A Study into the Characteristics of the Cohesion-Adhesion Relation and its Effects on Cutting Processes in Dredging Engineering

J.W. van den Broecke

MSc Thesis

TU Delft Delft University of Technology

CCCC China Communications Construction Company

A Study into the Characteristics of the Cohesion-Adhesion Relation and its Effect on Cutting Processes in Dredging Operations

Author:
J.W. van den Broecke

Supervisors:
Dr. Ir. S.A. Miedema
Dr. G. Liu
Ir. X. Chen

In partial fulfillment of the requirements for the degree of
Master of Science
in Offshore & Dredging Engineering

Dredging Engineering
Delft University of Technology

December 5, 2018

A Study into the Characteristics of the Cohesion-Adhesion Relation and its Effect on Cutting Processes in Dredging Operations

Author:
J.W. van den Broecke

Thesis Committee:

Dr. Ir. S.A. Miedema	Delft University of Technology
Dr. Ir. D.J.M. Ngan-Tillard	Delft University of Technology
Dr. G. Hong	CCCC National Engineering Research Center for Dredging Technology and Equipment
Dr. G. Liu	CCCC National Engineering Research Center for Dredging Technology and Equipment
Ir. X. Chen	Delft University of Technology

Under the authority of:
Delft University of Technology
National Engineering Research Center for Dredging Technology and Equipment Co. Ltd.

DELFT UNIVERSITY OF TECHNOLOGY

Abstract

Mechanical, Maritime and Materials Engineering
Offshore & Dredging Engineering

Master of Science

A Study into the Characteristics of the Cohesion-Adhesion Relation and its Effect on Cutting Processes in Dredging Operations

by J.W. van den Broecke

In the last two decades, the global economy and population have been growing steadily. Due to this global trends the demand for dredging, trenching and deep sea mining activities have grown dramatically. In these engineering practices, underwater excavation is one of the major procedures which involves complicated physics. In dredging, operations with clamshell buckets in saturated cohesive soils often leads to a decreased production due to the highly adhesive properties of these soils. And, in offshore wind farm installation operations, the vulnerable power cables transporting the generated energy must be buried a couple of meters under the seabed for their protection, so trenching in saturated cohesive soils becomes indispensable.

Based on the soil mechanical properties, the soils on which the underwater excavation process is applied to can be divided into three categories, namely: sand, clay and rock, where sand is non-cohesive and the other two are cohesive materials. To reasonably estimate the cutting force and cutting energy needed, Miedema has developed "The Delft Sand, Clay and Rock Cutting Model", in which several sets of equations are derived for each type of seabed soil. In the scenario of clay cutting, both the cohesion and adhesion should be known as the input parameters. However, very few information is available to define the relation between cohesion and adhesion. Yet, it is of great importance to get a better understanding of the relationship between cohesive and adhesive forces, because the large surfaces on dredging tools can generate a lot of resistance; limiting production for materials with increasing adhesion.

First, literature is reviewed to get a better understanding into the relevant soil mechanical properties and cutting theories. Existing models for the adhesion factor, which is defined as the ratio between the adhesion or stickiness of a cohesive soil and its cohesion or internal shear strength, are analyzed and new models for the adhesion factor are constructed.

To validate these new models, a new dedicated test setup is constructed with the help of the National Engineering Research Center for Dredging Technology and Equipment based in Shanghai, China. Tests are performed on two different cohesive soils (clays) to obtain the adhesion and cohesion of the samples. Furthermore, the test data is analyzed and the data is used to validate the models.

Finally, the obtained relation between the adhesion and cohesion is implemented in a numerical discrete element model for clay cutting. Two models are constructed to validate the properties of the numerical clay sample, after which the full cutting model is validated using existing experimental data obtained by Hatamura and Chijiiwa. With this validated cutting model, it is now possible to simulate the cutting force on more complicated geometries.

Acknowledgements

I would like to use this opportunity to express my gratitude to everyone who supported me throughout the course of this master thesis. First and foremost, I have to thank the National Engineering Research Center for Dredging Technology and Equipment Co. Ltd. for inviting me to come to Shanghai, China and for granting me permission to use their outstanding modern facilities and make this master thesis possible.

I would like to express my gratitude to my daily supervisors in both Delft and Shanghai: Xiuhan Chen and Dr. Liu. Thank you for the patience, the useful remarks, comments and engagement throughout this project. Furthermore, I express my warm thanks to Shao and Shuwei, for helping me with the day to day life and the experiments in China. Finally, I would like to thank Sape Miedema for introducing me to the topic as well as the support during the course of this project.

Of course, getting through this project required more than academic support. I would like to thank Tom for the fantastic time in Shanghai, both in and outside of office hours. Furthermore, I would like to thank my roommates for their support and the Champions League nights which offered some welcome distraction from the project.

Most importantly, none of this would be possible without my family. I want to thank my parents for believing in me and making this education possible over the years. I would like to thank my brother and sister for the support and for keeping me sharp with the (often offensive) remarks portraying me as a child playing with sticky clay. Finally, I would like to thank my girlfriend for the support and much needed distraction.

During the course of this project I developed myself on both a personal and professional level. It was amazing to be able to getting to know a new culture and to experience the hospitality of the Chinese people during my stay in China. On the academic level, this project required me to apply the skills I acquired over the years to conduct research in both an analytic and experimental way. One lesson to take away from this research is that fact that, when something does not go the way you planned it to go, take matters in your own hands, improvise and overcome.

Jan van den Broecke
Delft
December 2018

Contents

iii

Acknowledgements **v**

I Introduction to Dredging Processes Influenced by Adhesive Forces **1**

1 Introduction **3**
1.1 Thesis Background . . . 3
1.2 Research Goals . . . 4
1.3 Research approach . . . 4
1.4 Report Structure . . . 4

2 Dredging Processes Influenced by Adhesive Forces **5**
2.1 Subsea Ploughing . . . 5
2.2 Clamshell Dredging . . . 7

3 Soil Mechanical Properties of Cohesive Soils **11**
3.1 Basic Soil Parameters . . . 11
3.1.1 Soil Classification . . . 11
3.1.2 Moisture Content and Degree of Saturation . . . 12
3.1.3 Atterberg Limits . . . 12
3.1.4 Angles of Internal and External Friction . . . 13
3.1.5 Shear Strength . . . 14
3.2 Clay . . . 14
3.2.1 Clay Mineralogy . . . 15
3.3 Mechanical Properties of Clay . . . 17
3.3.1 Internal shear strength: cohesion . . . 18
3.3.2 External shear strength: adhesion . . . 19

4 The Two Dimensional Soil Cutting Theory **23**
4.1 Overview of The Various Cutting Mechanisms . . . 23
4.2 Cutting Theory for Cohesive Soils . . . 23
4.3 The Flow Type . . . 24

II Literature Review on the Cohesion-Adhesion Relation **27**

5 Existing Models for the Adhesion Factor **29**
5.1 Adhesion Factor Models Based on Total Shear Resistance . . . 29
5.2 Adhesion Factor Models Based on Adhesive Resistance . . . 31

III Experiments and Results **35**

6 Experimental Study **37**
6.1 Adhesion Test Setup Design . . . 37
6.1.1 Horizontal Adhesion Test Setup . . . 37
6.1.2 Vertical Adhesion Test Setup . . . 38
6.2 Experimental Setup . . . 41
6.2.1 Adhesion and External Friction Angle . . . 41
6.2.2 Cohesion and Internal Friction Angle . . . 42
6.2.3 Blade Roughness . . . 42
6.3 Experimental Matrix . . . 43
6.4 Soils . . . 44
6.5 Procedure . . . 44
6.5.1 Adhesion and External Friction Angle Tests . . . 44
6.5.2 Cohesion and Internal Friction Angle Tests . . . 45
6.5.3 Procedure Summary . . . 45

7 Results and Discussion **47**
7.1 Internal and External Shear Strength and Friction Angles . . . 47
7.2 Adhesion Factor . . . 52
7.3 Discussion on the Mechanism of Adhesion . . . 52

IV Implementation of the Cohesion-Adhesion Model: Numerical Modelling for Clay Cutting **55**

8 Numerical Modeling for Clay Cutting **57**
8.1 Discrete Element Modeling . . . 57
8.2 Implementing Cohesive and Adhesive Shear Strength . . . 58
8.3 Validation of the Cutting Model . . . 62

9 Conclusions and Recommendations **67**
9.1 Recommendations . . . 68

Bibliography **69**

A Appendix to Chapter 6: Experimental Study **77**
A.1 Vertical Adhesion Test Setup Drawings . . . 77
A.2 Pictures of the Adhesion Test Setup . . . 84
A.3 Direct Shear Apparatus . . . 85
A.4 Atterberg Limit Tests . . . 86
A.5 X-ray Diffraction Results . . . 88

B Appendix to Chapter 8: Numerical Modeling for Clay Cutting **91**
B.1 DEM Code for Schulze Ring Shear Test . . . 91
B.2 DEM Code for The Blade pull-out Test . . . 94
B.3 DEM Code for the Cutting Model . . . 98

Part I

Introduction to Dredging Processes Influenced by Adhesive Forces

Chapter 1

Introduction

1.1 Thesis Background

In the last two decades, the global economy and population have been growing steadily. An ever growing number of people benefit from increasing welfare, expanding the market for luxury goods like high-end consumer electronics. The already densely populated coastal areas get even more crowded, which calls for new artificial islands where human activities can take place. Furthermore, the rising demand for green energy has stimulated the development and installation of more and more offshore wind farms. And, as global trade increases, there is more and more demand for dredging activities to keep ports and waterways navigable. Due to these global trends the demand for dredging, trenching and deep sea mining activities have grown dramatically the past 20 years.

In these engineering practices, underwater excavation is one of the major procedures which involves complicated physics. In dredging, operations with clamshell buckets in saturated cohesive soils often leads to a decreased production for highly adhesive soils. And, in offshore wind farm installation operations, the vulnerable power cables transporting the generated energy must be buried a couple of meters under the seabed for their protection, so trenching in saturated cohesive soils becomes indispensable.

Based on the soil mechanical properties, the soils on which the underwater excavation process is applied to can be divided into three categories, namely: sand, clay and rock, where sand is non-cohesive and the other two are cohesive materials. To reasonably estimate the cutting force and cutting energy needed, (Miedema, 2015) has developed "The Delft Sand, Clay and Rock Cutting Model", in which several sets of equations are derived for each type of seabed soil. In these equations, the cutting depth, the cutting angle, the cutting speed and the soil properties are used as input parameters, while the cutting forces and the specific energy are the output results. In the scenario of clay cutting, both the cohesion and adhesion should be known as the input parameters. However, very few information is available to define the relation between cohesion and adhesion. Yet, it is of great importance to get a better understanding of the relationship between cohesive and adhesive forces, because the large surfaces on dredging tools can generate a lot of resistance; limiting production for materials with increasing adhesion. Because the relationship is not exactly known, the adhesive strength of a clay is usually expressed as a fixed fraction of the cohesive strength, varying between 60% for hard clays and 100% for soft clays. Therefore, understanding the relation between cohesion and adhesion can be the key in optimizing the designs of dredging tools and can help to improve overall production in dredging operations. (X. Chen, Broecke, et al., 2019)

1.2 Research Goals

The main goal of this research is to characterize the relation between cohesion and adhesion in cohesive soils through experimental research. Subsequently, this new relation can be implemented in Miedema's "Delft Sand, Clay and Rock Cutting Model" to be able to analytically calculate and estimate cutting forces in cohesive soils.

Furthermore, a side goal of this research is develop a numerical model in which the cohesive and adhesive shear strength of a numerical soil sample can be validated. With these tools, the obtained cohesion - adhesion relation can be implemented in the numerical Delft 3D cutting model (3DCM) and can be used to simulate the cutting forces on complex geometries in cohesive soils.

1.3 Research approach

First, literature with respect to dredging processes influenced by adhesive forces, cohesive soils and already existing cohesion-adhesion models is reviewed. To investigate and analyze the relation between cohesion and adhesion, a custom test setup is designed and constructed, whereafter a series of experiments is carried out, aiming at discovering the fundamental relation between cohesion and adhesion in clay. With these results, the analytic model from Miedema can be implemented and serve industrial applications.

1.4 Report Structure

This report is made up out of 8 chapters, divided over 4 parts. Part 1 is an introduction to dredging processes influenced by adhesive forces and consists of 3 chapters. In Chapter 2 two common dredging operations influenced by adhesive forces are covered. A general overview is presented and the importance of understanding the cohesion-adhesion relation with respect to estimating forces and production in these processes is highlighted. Chapter 3 presents an overview of the mineralogy and soil mechanical properties of clay, the main type of cohesive soil encountered in marine dredging operations. Finally, in Chapter 4, the theory for two dimensional soil cutting is discussed.

Part 2 covers the literature review on the Cohesion-Adhesion relation. In Chapter 5, existing data and models for the adhesion factor are discussed and new models for dredging applications are presented.

Part 3 covers the experimental part of the research and the obtained results. In Chapter **??**, the design concepts, the final experimental setup, the experimental matrix and the experimental procedure are discussed. Subsequently, the obtained results are analyzed and discussed in Chapter 7.

Part 4 discusses the implementation of the developed cohesion-adhesion models in numerical simulation for clay cutting. in Chapter 8, the numerical principles and techniques used are covered, validation of the numerical clay sample is discussed and the validation of the overall cutting model using existing experiments is presented. Finally, the conclusion is presented and recommendations are made in Chapter 9.

Chapter 2

Dredging Processes Influenced by Adhesive Forces

In this chapter two common dredging operations influenced by adhesive forces are covered. A general overview of subsea ploughing and clamshell dredging is presented and the importance of understanding the cohesion-adhesion relation with respect to estimating forces and production in these processes is highlighted.

2.1 Subsea Ploughing

In the last decade the demand for subsea cable protection has grown dramatically, mostly because of the rapid development of the offshore renewable market. Both infield cables between offshore power generators, e.g. offshore wind turbines, and export cables between the offshore substations and shore need to be protected against hostile interventions. These hostile interventions can be of a natural cause, like subsea landslides, seismic activity, seabed mobility and iceberg scour, or can be human induced hazards like fishing activities, anchor movement and dropped objects. Damage to offshore cables and pipelines is not only very costly to repair, but can also lead to massive damage to the environment and the possible people involved. Therefore sufficient protection of these offshore cables and pipelines is required.

The two most used methods for cable protection are cable burying or trenching and cable protection by rock dumping or flexible concrete mattresses. In general, protection by rock dumping or flexible concrete mattresses is used at locations of particular concern, e.g. the crossing of two cables or locations where it has not been practical to operate cable burying equipment. Protection by burial or trenching is considered the most effective and reliable method and is typically the cable protection method when longer lengths of cable protection are required. (BERR, 2008) Trenching a cable or pipeline can be performed by several methods:

- Ploughing: a plough is pulled through the seabed to form a trench.
- Mechanical Cutting: a trench is formed by cutting the soil with a cutting disk or chain.
- Jetting: the soil is fluidized and blown away by a jet, after which a cable can be lowered in the formed trenched.

One of the dredging operations where the cohesive and adhesive properties of soils play a important role in determining the overall cutting force required, is subsea ploughing. In offshore ploughing operations, a plough, which is a passive tool, is pulled through the soil by a host vessel. By using a sufficient bollard pull, continuous progress through the seabed is achieved. During trenching, the plough lifts a wedge of soil and places the cable at the base of the trench before the wedge of soil then naturally backfills over the cable using gravity. Two main types of subsea

ploughs are used: V-shaped ploughs, typically used for burying pipelines, and narrow-shaped ploughs, typically used for the burial of cables. Ploughs are capable of working in a wide range of soils and are capable of operating in water depths up to 1500m. (BERR, 2008)

An example of a V-Shaped plough used to bury pipe is depicted in Figure 2.1. Figure 2.1 depicts the PL3 Pipe Burial Plough designed by Royal IHC. Some basic properties of the PL3 are presented in Table 2.1.

TABLE 2.1: General Properties of the PL3 Pipe Burial Plough by Royal IHC. (IHC, 2009)

Dimensions	22 m (L) x 12 (W) x 10 (H)	$[m]$
Weight	Atmospheric: 175	$[T]$
	Submerged: 150	$[T]$
Operating Depth	Max. 1000	$[m]$
Trench Depth	Max Single Pass: 1.5	$[m]$
	Max. Multi-Pass: 2.5	$[m]$
Pipe Size	75 - 1550	$[mm]$

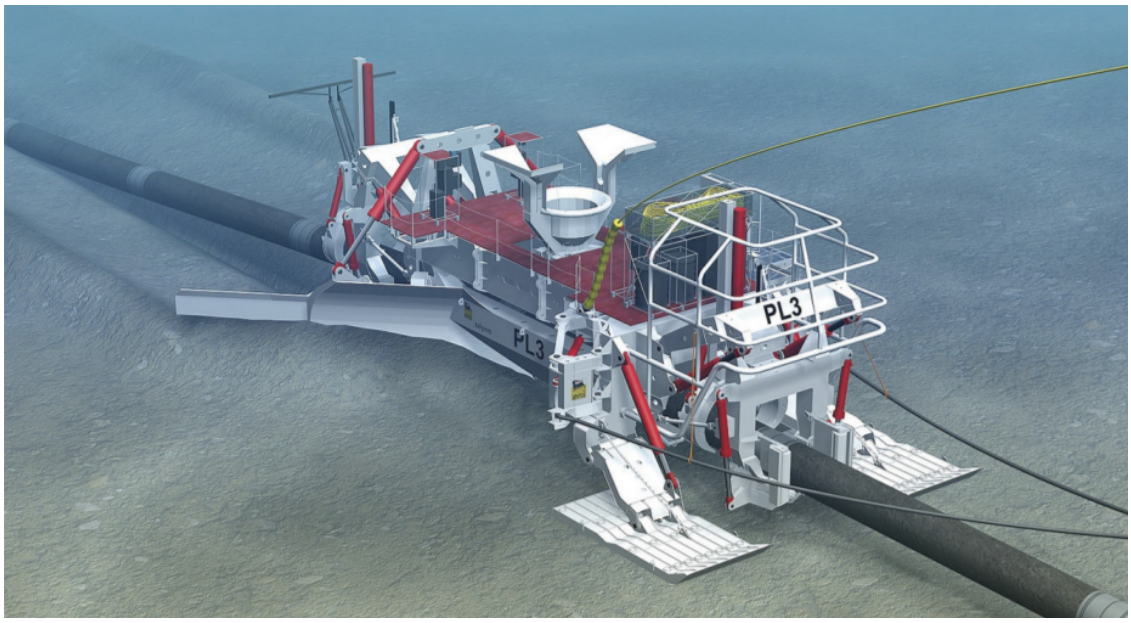

FIGURE 2.1: The PL3 V-shaped Pipe Burial Plough Designed by Royal IHC. Retrieved from IHC, 2009

Van Gurp developed a basic model to predict the pulling forces during subsea ploughing of the seabed. The cutting model by Van Gurp is given in Equation 2.1.

$$F_{pull} = \underbrace{s_u \cdot N_c \cdot d \cdot b}_{\text{cutting component}} + \underbrace{2 \cdot \alpha \cdot s_u \cdot d \cdot l_a}_{\text{adhesive resistance}} \tag{2.1}$$

Where s_u is the undrained shear strength of a cohesive soil $[kPa]$, N_c a dimensionless coefficient depending on the plough geometry [-], d the ploughing depth $[m]$, b the ploughing width $[m]$, α the adhesion coefficient defined as $\frac{a}{c}$ [-] and l_a the adhesion length $[m]$ (depending on the plough geometry.

2.2 Clamshell Dredging

The grab or clamshell dredger is the most common used dredger in the world, especially in North America and the Far East. The clamshell dredger is a relatively simple dredging concept: a stationary dredger with or without propulsion, capable of picking up seabed material with a clam shell bucket, which hangs from an onboard crane. In the case of a self-propelled clamshell dredger, the dredged material can be stored in an onboard hopper. Otherwise, the dredged material is transported using barges. An schematic representation of a self-propelled clamshell dredge is depicted in Figure 2.2. (Miedema and Vlasblom, 2006)

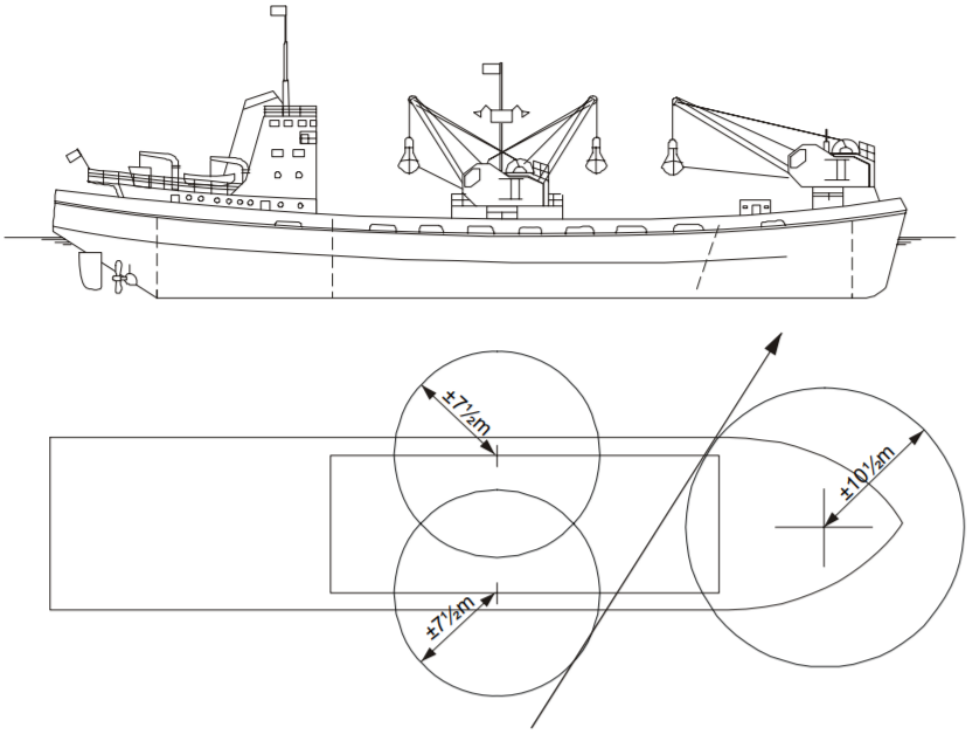

FIGURE 2.2: Schematic Representation of a Self-propelled Clamshell Dredger. Retrieved from Miedema and Vlasblom, 2006

Clamshell dredgers are typically used in dredging operations at locations which are difficult to access, e.g. harbours. Other operations where clamshell dredgers are used are dredging operations where small quantities with strongly varying depth need to be dredged, sand and gravel mining and dredging operations in moraine areas, where big stones and boulders can be expected. (Miedema and Vlasblom, 2006)

The capacity of a clamshell dredge is expressed in the clamshell bucket- or grab volume. Clamshell buckets can vary in size from 1 m^3 up to a volume of 200 m^3. Typically, the opening of the clamshell bucket is controlled by the closing and hoisting wires or by hydraulic cylinders. To ensure that the clamshell bucket does not spin during hoisting and lowering many cranes are equipped with a tag line, running from half way the boom straight to the clamshell bucket. The clamshell dredging process is discontinuous and cyclic, consisting of the following steps (in the case of a cable clamshell): (Miedema and Vlasblom, 2006)

- Lowering of the clamshell bucket to the seabed.
- Closing of the clamshell bucket by pulling the hoisting wire.

- When the bucket is completely closed, the hoisting starts.
- Swinging the filled bucket to the barge or onboard hopper.
- Lowering the filled bucket into the barge or hopper.
- Opening the bucket by releasing the closing wire.

A schematic representation of a cable clamshell hoisting system is given in Figure 2.3.

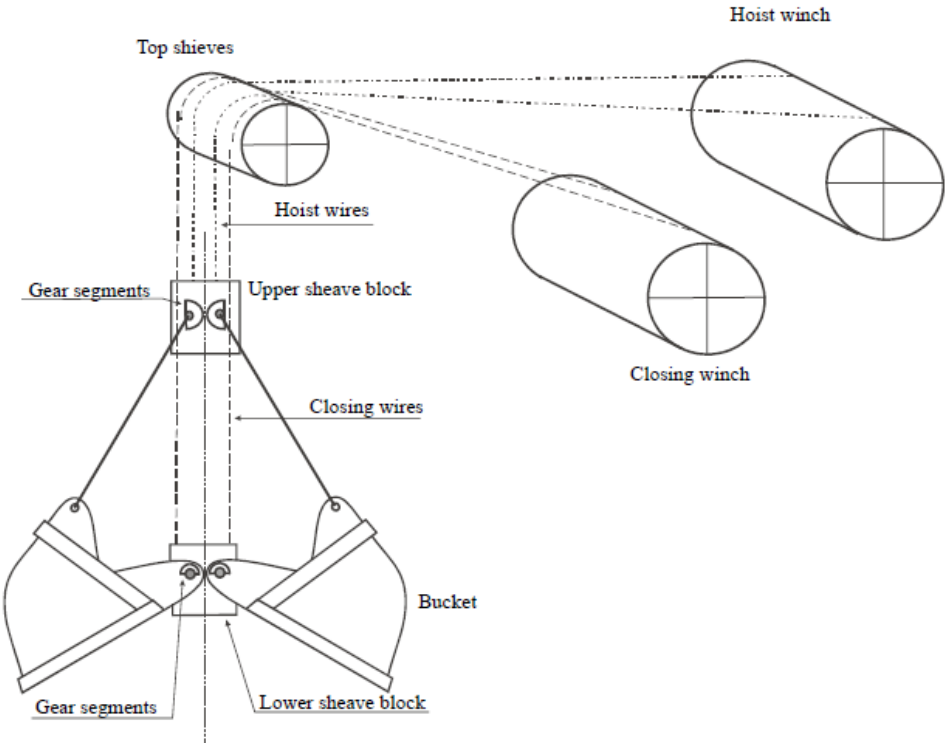

FIGURE 2.3: Schematic Representation of a Cable Clamshell Bucket Hoisting System . Retrieved from Miedema and Vlasblom, 2006

Miedema and Vlasblom developed a model to calculate the cutting forces in clamshell dredging operations in saturated sand. With the cutting theory developed by Miedema, 2015 for clay cutting, this model can be adapted to analyze the forces on a clamshell bucket during the dredging of clay. Since the equations of motion of the clamshell grabbing process are non-linear, the equations have to be solved numerically. The buckets of the clamshell are subject to forces and resulting moments exerted out by the soil on the buckets. The forces and moments can be divided into forces and moments as a result of the cutting forces on the cutting edges of the buckets and forces and moments as a result of the soil adhesion and friction on the side edges of the buckets. (Miedema and Vlasblom, 2006)

As mentioned earlier, the cutting forces on the clamshell buckets can be calculated using Miedema's equations for clay cutting. Miedema's cutting theory will be extensively covered in Chapter 4, so the resulting Equations will just be summarized here. When assuming clay is cut according to the flow type, the horizontal and vertical cutting force on the blade edge can be calculated according Equations 2.2, 2.3 and 2.4.

$$F_h = \lambda \cdot c \cdot h_i \cdot w \cdot \frac{\frac{sin(\alpha_a)}{sin(\beta)} + r \cdot \frac{sin(\beta)}{sin(\alpha_a)}}{sin(\alpha_a + \beta)} \tag{2.2}$$

$$F_v = \lambda \cdot c \cdot h_i \cdot w \cdot \frac{\frac{cos(\alpha_a)}{sin(\beta)} - r \cdot \frac{cos(\beta)}{sin(\alpha_a)}}{sin(\alpha_a + \beta)} \tag{2.3}$$

$$r = \frac{a \cdot h_b}{c \cdot h_i} \tag{2.4}$$

Where F_h is the horizontal cutting force which is aligned with the direction of the cutting edge $[N]$ while F_v is the vertical cutting force $[N]$,α_a is the cutting angle [-], β is the angle of the shear plane with the direction of the cutting velocity [-], λ is the strengthening factor which follows the fact that when the cutting velocity increases, the clay gets stronger. c is the cohesive shear stress $[Pa]$ while a is the adhesive shear stress $[Pa]$, h_i is the cutting depth $[m]$, h_b is the blade height $[m]$, w is the width of the blade $[m]$ and r the parameter that represents the adhesion factor α, which is defined as $\frac{a}{c}$ [-].

The pressure force on the side egdges of the bucket are modelled as the forces on a stip footing. Using Terzaghi's bearing capacity theory for foundations, the pressure force on the side egdges of the bucket can be calculated according to Equation. (Miedema and Vlasblom, 2006)

$$F_e = \left(c \cdot N_{cp} + \frac{1}{2} \cdot \gamma_s \cdot b \cdot N_\gamma + \gamma_s \cdot h_i \cdot N_q \right) \cdot A_e \tag{2.5}$$

Where c is the cohesion in $[kPa]$, N_c, N_γ and N_q Terzaghi's bearing capacity factors depending on soil internal friction angle ϕ, γ_s the unit weight of the soil $[kg/m^3]$, b the width of the cutting edge $[m]$ and h_i the height of the cutting edge $[m]$. Furthermore, the frictional force on the bucket edges can be calculated by integrating the shear stress, presented in Equation, over the edge surfaces of the buckets A_e $[m^3]$. (Miedema and Vlasblom, 2006)

$$\tau_e = \sigma_e \cdot \tan(\delta) + \alpha \cdot c \tag{2.6}$$

Where τ_e is the shear stress on the edge of the buckets $[kPa]$, σ_e the normal stress on the edge of the buckets $[kPa]$, δ the soil to metal friction angle [deg], α the adhesion factor [-] and c the cohesion $[kPa]$.

In the set of equations for both subsea ploughing and clamshell dredging, the ratio α is an unknown parameter, which reflects one of the fundamental mechanical properties of the clay soil: the ratio between adhesion and cohesion, also called the adhesion factor. Understanding the relation between cohesion and adhesion is key in predicting cutting forces on dredging tools and finally, optimizing production estimations in these dredging operations. (X. Chen, Broecke, et al., 2019)

Chapter 3

Soil Mechanical Properties of Cohesive Soils

In this chapter an overview of the mineralogy and soil mechanical properties of clay, the main type of cohesive soil encountered in marine dredging operations, is presented. First, an overview of basic soil parameters encountered in soil mechanics is given in Paragraph 3.1. Subsequently, the clays and their properties are discussed in Paragraph 3.2. Basic soil mechanics regarding clay and the mechanical properties of clay are presented in Paragraph 3.3.

3.1 Basic Soil Parameters

3.1.1 Soil Classification

In dredging operations a wide variety of sedimentary deposits, more commonly known as soils, is encountered. These soils can range from granular soils like sand and gravel up to fine-grained soils like silts and clay, or any mixture in between. In general, classification of soil separates is performed according to their particle size. Table 3.1 shows the particle diameter limits used for soil classification by the United States Department of Agriculture (*USDA* 2018) (Miedema, 2015):

TABLE 3.1: Soil classification according to Soil particle size according to Miedema, 2015

Name of Soil	Diameter Limits [mm]
Clay	< 0.002
Silt	0.002-0.06
Sand	0.06-2
Gravel	2-60
Cobbles	60-200
Boulders	> 200

Typically, the soil encountered in real-life dredging operations is not comprised of just one of the soil separates: it is a mixture of various types of soil. An overview showing the naming of soils according to their relative sand, clay and silt content according to the United States Department of Agriculture (USDA) is shown in Figure 3.1.

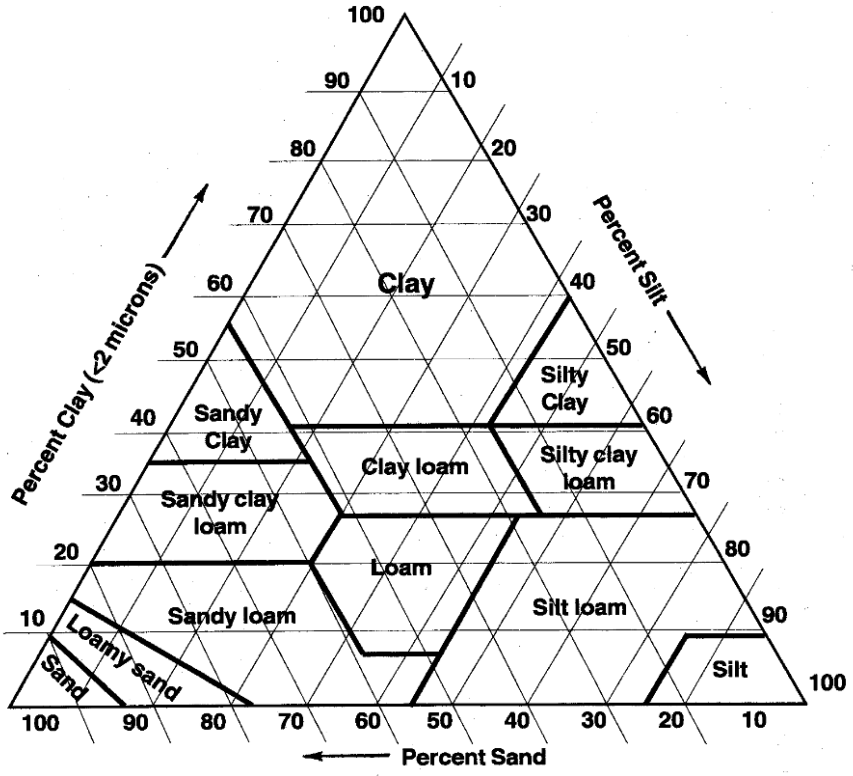

FIGURE 3.1: Soil naming according to the United States Department of Agriculture. Retrieved from `https://www.nrcs.usda.gov`.

3.1.2 Moisture Content and Degree of Saturation

The moisture content, ww [-], is an important index for the state and behaviour of a soil. It is defined as the ration between the mass of water in the soil and the mass of solids in the soil, as given in Equation 3.1.

$$ww = \frac{m_w}{m_s} \qquad [-] \tag{3.1}$$

Where m_w is the mass of the water in the soil [kg] and m_s the mass of the solids [kg]. Another important parameter regarding moisture in a soil, is the degree of saturation S [-]. The degree of saturation is defined as the ration between the volume of water in the soil and the total pore volume (which is equal to the sum of the volume of water and the volume of air in the soil), as given in Equation 3.2.

$$S = \frac{V_w}{V_p} = \frac{V_w}{V_a + V_w} \qquad [-] \tag{3.2}$$

Where V_w is the volume of water [m^3], the volume of air in the soil [m^3] and V_p the total pore volume [m^3]. A soil is said to be fully saturated when S equals 1. (Barnes, 1995)

3.1.3 Atterberg Limits

The Atterberg Limits are a basic tool to define the behavior of fine-grained soils according to their water content. Depending on the water content, the soil may appear in one of four states: the solid, semi-solid, plastic or liquid state. In each of the four states, the consistency, behavior and

thus it's engineering properties are different: therefore the boundary between each state can be defined based on the change in a soil's behavior. (Miedema, 2015) A graphic representation of the Atterberg Limits is shown in Figure 3.2.

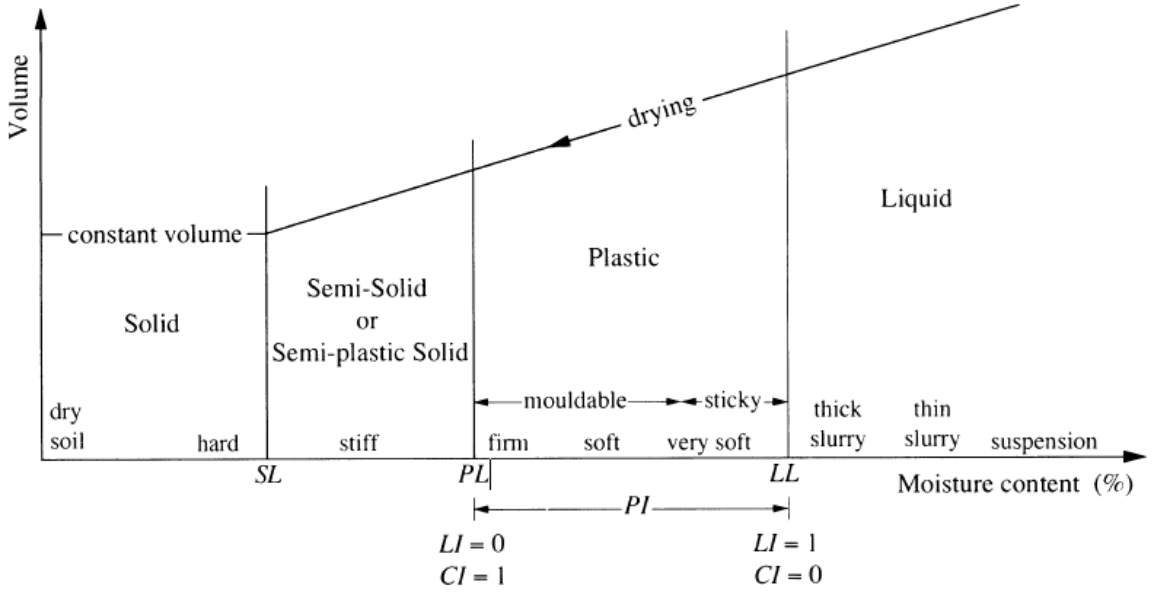

FIGURE 3.2: The Atterberg Limits. Retrieved from Barnes, 1995

The Shrinkage Limit

As depicted in Figure 3.2, the Shrinkage Limit (SL) is the moisture content below which soils do not reduce in volume anymore as the soil continues to dry out. (Miedema, 2015) The Shrinkage Limit is typically used in the production of ceramics, but is not important in the continuation of this research.

The Plastic Limit

The Plastic Limit (PL) is the lowest moisture content where a soil is said to behave like a plastic material; it is the transition between brittle and plastic behavior. A soil is said to be at its Plastic Limit when a string of soil with a diameter of 3 *mm* begins to crumble; the Plastic Limit is defined in the ASTM D-4318 standard test method. (*ASTM International* 2018) (Miedema, 2015)

The Liquid Limit

The water content at which the behaviour of a soil changes from plastic to liquid is called the Liquid Limit (LL). The Liquid Limit can be measured using the Casagrande Method, defined in the ASTM D-4318 standard test method or with a fall cone test. (*ASTM International* 2018) (Miedema, 2015)

3.1.4 Angles of Internal and External Friction

The angle of internal friction, which is represented by the Greek letter ϕ [deg], is a measure of a soil's ability to withstand a shear stress. It is defined as the angle between the normal force and the resultant force when failure of the soil just occurs due to a shearing stress on the soil. In a direct shear test (soil-soil), the angle of internal friction is visually represented in Mohr's circle as

the slope angle of the Mohr-Coulomb failure criterion (see Paragraph 3.3). The angle of internal friction is determined experimentally by performing a direct shear test or a triaxial test. (Miedema, 2015)

Besides an angle of internal friction, soils also have an angle of external friction. The angle of external friction or δ is a measure for the friction between a soil and a body of another material. In a shear test between soil and a foreign body, for example soil-metal, the angle of external friction is visually represented in Mohr's Circle as the slope angle of the Mohr-Coulomb failure criterion (see Paragraph 3.3)

3.1.5 Shear Strength

The shear strength of a soil is a term used to describe the magnitude of shear stress a soil can sustain. As depicted in Figure 3.3, gravel, sand and silt are soils comprised of larger, bulky particles. The strength of these soil types depends purely on the interlocking and friction between the granular particles. Consequently, these soils cannot sustain any shear stress in the absence of a normal load on the soil, and are therefore called cohesionless soils.

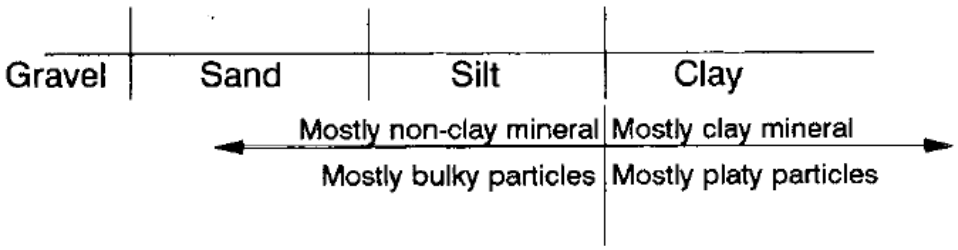

FIGURE 3.3: Particle size ranges for engineering classifications. Retrieved from Mitchell and Soga (2005).

In contrast to gravel, sand and silt, clay is comprised of very small platy particles. Because these platy particles form mutual covalent-, ionic- and Vanderwaals-bonds, clayey soils posses cohesive properties. This means that depending on the type of clay among other variables, the soil has a shear strength even in the absence of a normal load on the soil. This shear strength is called the cohesion or internal shear strength of the clay: it is the part of the clay's strength that is independent of inter-particle friction in the clay.

Most of the time, it can be stated that a soil possess cohesive properties when the amount of clay in the soil is large enough ($> \pm$ 30 %). So, a soil is regarded to be cohesive if enough clay is present. This is not 100% accurate, as soils with a high organic content like peat can also exert cohesive and adhesive properties. However, in the vast majority of dredging operations clay is the main cohesive soil encountered; therefore in the continuation of this research the focus will be on clayey soils.

3.2 Clay

In general, the term 'clay' can have several meanings. In engineering classifications clay refers to particles with a certain size: it is referred to as all elements in a soil with a particle diameter smaller than 0.002 mm or 2 μm. However, not all clay particles are smaller than 2 μm and not all non-clay particles are bigger than 2 μm. Nevertheless, it is still a useful classification as the amount of clay minerals in a soil is usually closely approximated by the amount of particles smaller than 2 μm

(Mitchell and Soga, 2005). In mineralogy, the term clay refers to clay minerals. Mitchell and Soga, 2005 define clay minerals as the minerals with the following properties:

- Small particle size
- A net negative electrical charge
- Plasticity when mixed with water
- High weathering resistance

3.2.1 Clay Mineralogy

Clay minerals are complex mineral structures with a distinctive sheet-like structure. To be able to build a conceptual model of these minerals, they are visualized and characterized using a building block approach. The structure of the majority of clay minerals is made up of combinations of two basic building blocks: the silicon tetrahedron, depicted in Figure 3.4(a), and the aluminium or magnesium octahedron, depicted in Figure (Mitchell and Soga (2005).

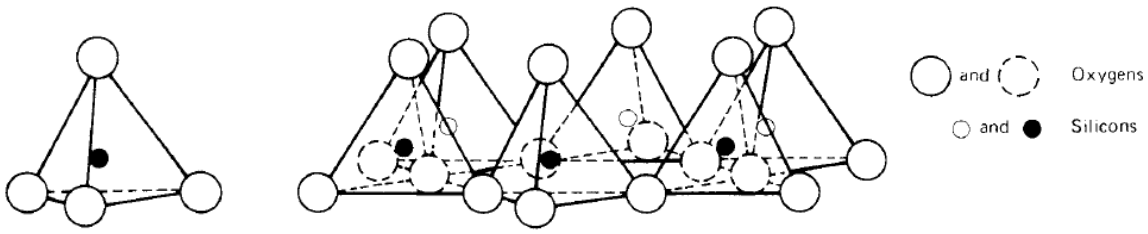

(a) Tetrahedral unit (b) Silica tetrahedra units arranged in a tetrahedral sheet structure

FIGURE 3.4: Overview of a single silicon tetrahedron and a silica sheet. Retrieved from Mitchell and Soga (2005).

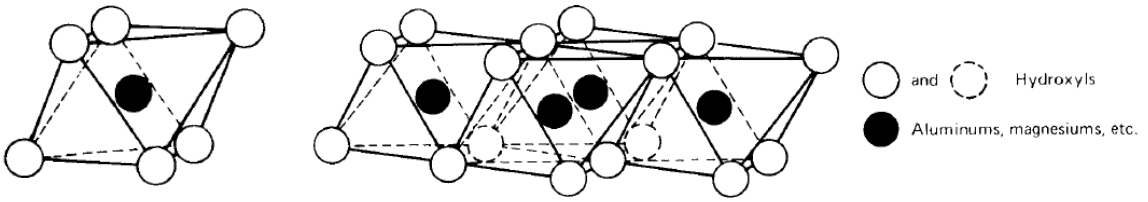

(a) Octahedral unit (b) Octahedral units arranged in a octahedral sheet structure

FIGURE 3.5: Overview of a single octahedral unit and an octahedral sheet structure. Retrieved from Mitchell and Soga (2005).

The Silicon Tetrahedra form tetrahedral silica sheets. Three of the four oxygen atoms in each tetrahedron are shared to form a hexagonal net, as depicted in Figure 3.4(b). The octrahedral sheets are comprised of magnesium or aluminium in octrahedral coordination with oxygens or hydroxyls, as depicted in 3.5. The oxygen and hydroxyl ions dominate the mineral structure due to their number and size, explaining the negative character of these sheets even if their negative charges are satisfied. Furthermore, if substitution of cations (positive ions) has occurred because of a higher availability of these ions at the time of formation, for example Mg^{2+} for Al^{3+}, the

resulting negative character on the particle surface will be even greater. (Mitchell and Soga, 2005) (Barnes, 1995)

The tetrahedral and octahedral sheets combine to form layered units: either two-layer units (1:1) or three-layer units (2:1). The resulting negative charges are neutralized by the adsorption of other cations or polar water molecules on the surfaces. So, with various combinations of substituted cations, exchangeable cations, inter layer water and manners of structural layer stacking a wide variety of clay mineral structures is possible. (Barnes, 1995) An overview of structure of the most common groups of clay minerals is presented in Figure 3.6.

Mineral	Layer structure	Stack structure	Bonding between layers
kaolinite	1:1	Al or G Si Al or G Si	hydrogen bonds (strong)
halloysite	1:1	Al or G Si ○ ○ ○ ○ Al or G Si	hydrated with water molecules
illite	2:1	Si Al or G Si (K) (K) (K) Si Al or G Si	potassium ion (strong)
montmorillonite	2:1	Si Al or G Si Si Al or G Si	van der Waal's forces (weak) exchangeable ions water molecules
chlorite	2:1:1	Si Al or G Si B Si Al or G Si	brucite sheet

FIGURE 3.6: An overview of the most common types of clay minerals. Retrieved from (Barnes, 1995)

3.3 Mechanical Properties of Clay

In soil mechanics, Mohr's circle is used to describe the general state of stress in a point. The Mohr circle provides a relation between the principal stresses and the normal and shear stresses under an arbitrary angle α.

Consider an infinitesimal soil element with unit length under plain strain conditions as displayed in Figure 3.7. According to Miedema, in this derivation, the vertical and the horizontal stresses σ_v and σ_h are taken as the principal stresses but these could have any orientation.

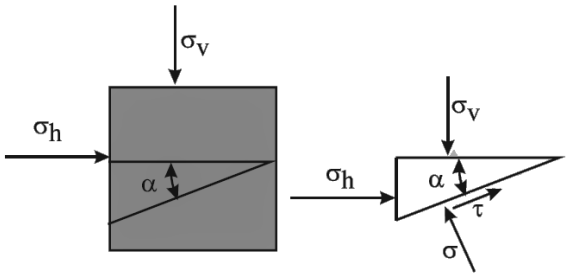

FIGURE 3.7: The stresses acting on an infinitesimal piece of soil. Retrieved from Miedema, 2015.

The soil element has unit length, therefore the equilibria of forces in the horizontal and vertical direction can easily be rewritten into the description for the principal stresses as presented in Equations 3.3 and 3.4 (Miedema, 2015):

$$\sigma_h \cdot \sin(\alpha) = \sigma \cdot \sin(\alpha) - \tau \cdot \cos(\alpha) \tag{3.3}$$

$$\sigma_v \cdot \cos(\alpha) = \sigma \cdot \cos(\alpha) + \tau \cdot \sin(\alpha) \tag{3.4}$$

Rewriting Equations 3.3 and 3.4 results in the equations for the normal and shear stresses as given in Equations 3.6 and 3.6 (Miedema, 2015).

$$\sigma = \left(\frac{\sigma_v + \sigma_h}{2}\right) + \left(\frac{\sigma_v - \sigma_h}{2}\right) \cdot \cos(2 \cdot \alpha) \tag{3.5}$$

$$\tau = \left(\frac{\sigma_v - \sigma_h}{2}\right) \cdot \sin(2 \cdot \alpha) \tag{3.6}$$

Squaring and adding Equations 3.6 and 3.6 gives the circle equation presented in Equation 3.7:

$$\left(\sigma - \left(\frac{\sigma_v + \sigma_h}{2}\right)\right)^2 + \tau^2 - \left(\frac{\sigma_v - \sigma_h}{2}\right)^2 \tag{3.7}$$

Equation 3.7 represents the Mohr circle: it describes the stress state of an arbitrary point in a soil for a given principal stress state. A graphical representation of the Mohr circle and the Mohr-Coulomb failure criterion for a cohesive soil like clay is presented in Figure 3.8. (Miedema, 2015)

In Figure 3.8, the Mohr-Coulomb failure criterion is given by the bold tangent line, according to Equation 3.8.

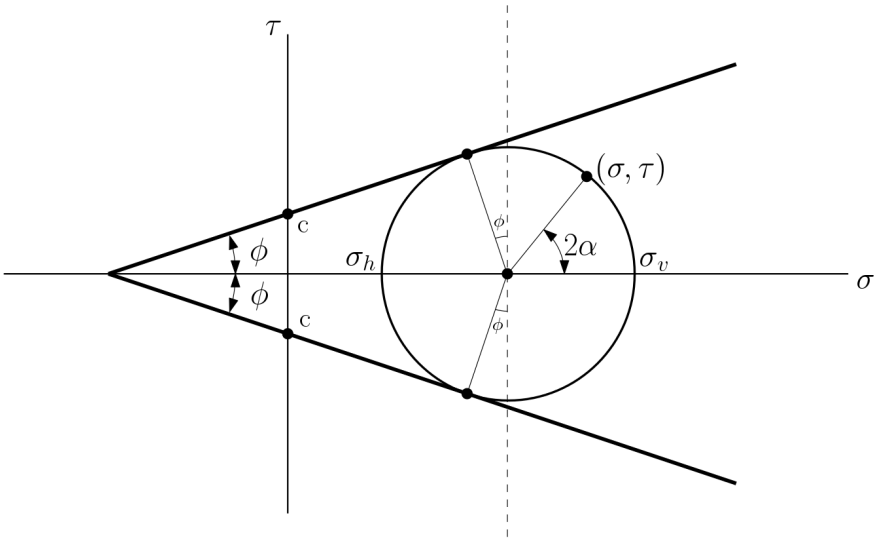

FIGURE 3.8: The Mohr circle with the Mohr-Coulomb failure criterion

$$\tau = c + \sigma \quad \tan(\phi) \tag{3.8}$$

Where c is the cohesion or internal shear strength of the clay [kPa], σ the normal stress [kPa] and ϕ the internal friction angle [deg].

3.3.1 Internal shear strength: cohesion

According to (Miedema, 2015), cohesion is the action or property of similar molecules sticking together, being mutually attractive. In clays, cohesion between particles is a result of the electrostatic forces between is caused by the shape and structure of its particles, which makes the distribution of orbiting electrons irregular when particle get close to one another, creating electrical attraction that can maintain a macroscopic structure such as a water drop.

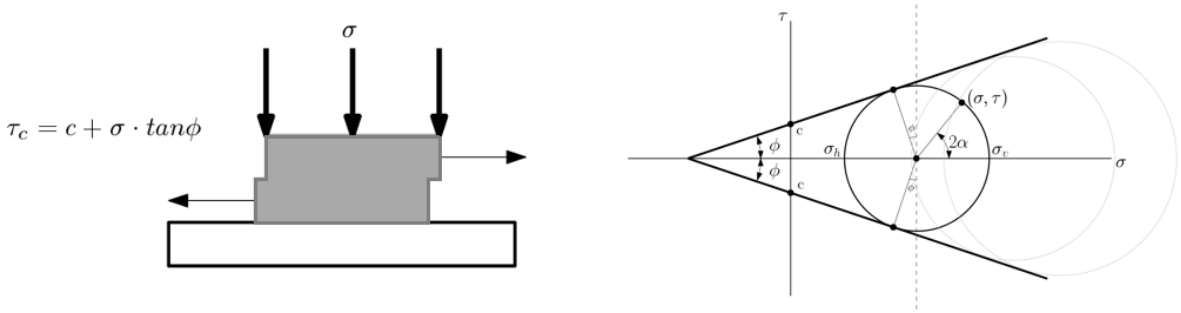

FIGURE 3.9: Direct shear test (soil-soil) with the Mohr-Coulomb failure criterion

As stated in Paragraph 3.1, cohesion (**c**)is the part of a clay's strength that is independent of inter-particle friction in the clay. This is clearly depicted in Figure3.9: for a normal stress σ equal to 0, the clay can sustain a shear stress τ larger than zero: this is the clays' cohesion.

3.3.2 External shear strength: adhesion

Adhesion is the phenomenon of a cohesive soil sticking to another material; it is a measure of the 'stickiness' of the soil. This adhesion between clays and other materials is partly due to direct attraction between the clay particles and the solid material and partly due to adhesive action of the water in the clay, but the latter force is strongly dominant. (Fountaine, 1953) Fountaine explains normal adhesion (adhesive tensile strength) using two idealized soils, as depicted in Figure 3.10.

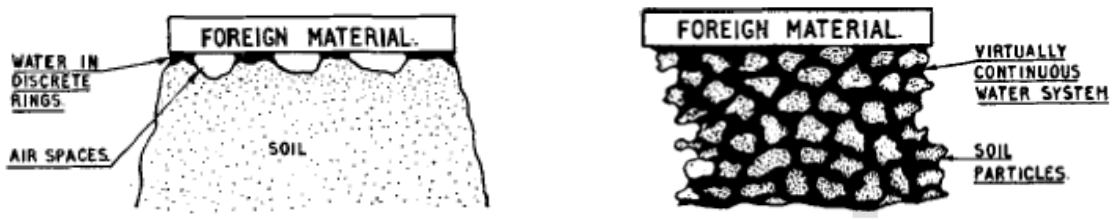

(a) (b)

FIGURE 3.10: Adhesion of a relatively dry and coarse soil (left) and a relatively wet ideal fine soil (right). Retrieved from: (Fountaine, 1953)

For the dry, coarse soil, adhesion is described as rings of water connecting discrete pinnacles of soil to the foreign material with rings of water. In this case, adhesion depends on the wettability of the foreign material. In the wet, fine-grained soil there is a water film between the soil surface and the steel, albeit not fully continuous. This water film is connected via microscopic channels to the bulk water content. To establish an equilibrium in moisture tension, the water has to move through these channels. Most of the water will move to channels where the channel size gives this same overall tension, but a fraction of the channels will be to small resulting in a forced curvature of the water/air menisci in these channels. This excess moisture tension results in an adhesive strength per unit area.

According to Tong et al., there are six possible contacting states: completely non-contacting asperities, water point contacting asperities, water loop contacting asperities, water film contacting particles, water film contacting micro-aggregates and clods. Tong et al. concluded that the adhesive component of tangential resistance is mainly comprised of the tangential viscous resistance of the water film on the contact area.

Zhang proposed that the total soil adhesive force consists out of 6 forces (Khan, Qaisrani, and Jian-Qiao, 2010):

$$a = a_m + a_e + a_c + a_v + a_w + a_g \tag{3.9}$$

Where:

- a = Soil adhesive force
- a_m = Sum of the molecular forces of soil molecules with other bodies
- a_e = Sum of the forces of electro-static attraction between two surfaces in contact
- a_c = Sum of the capillary forces produced by the surface of menisci formed by the contact between soil liquid and a contact surface of another body
- a_v = Viscous resistance of the soil liquid

- a_w = The wedge pressure that results from the pressure difference between the soil liquid pressure and the pressure in voids
- a_g = Force due to the negative air pressure by closed soil pores closed at the contact surface between soil and a body

In general, the adhesive strength of soils can be split into two components: the adhesive strength in normal direction or the adhesive tensile strength and the adhesive strength in tangential direction or the adhesive shear strength. A schematic depiction is presented in Figure 3.11 (Zimnik et al., 2014)

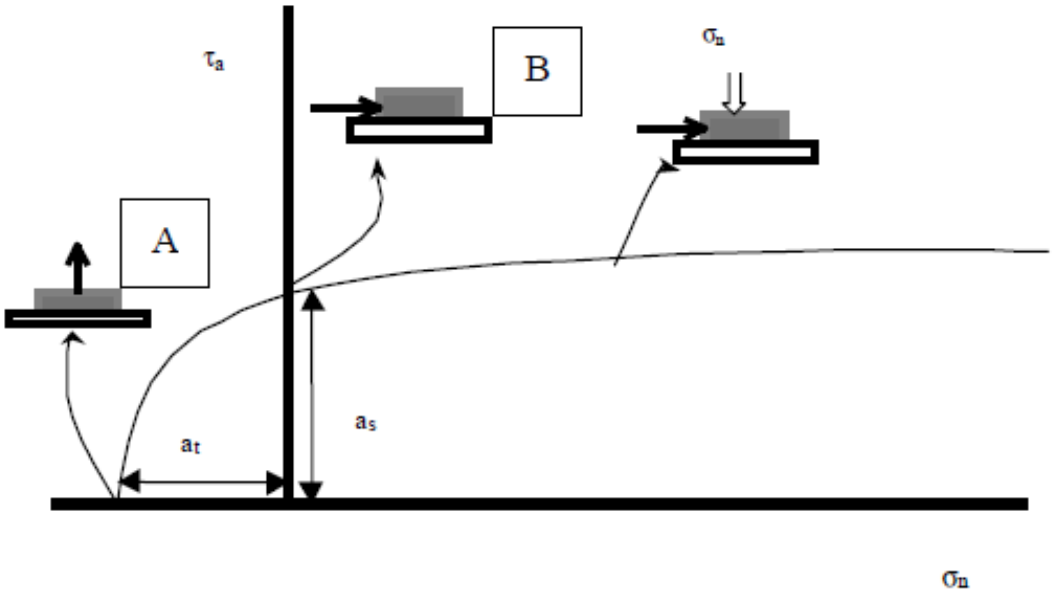

FIGURE 3.11: The adhesive tensile strength (normal pull) and the adhesive shear strength (tangential pull). Retrieved from (Zimnik et al., 2014)

When pulling a body from an adhesive soil in normal direction, the adhesive tensile strength is simply given by Equation 3.10.

$$a_t = \frac{F}{S_c} \tag{3.10}$$

Where a_t is the adhesive tensile strength, F is the required pulling force and S_c is the effective soil-body contact area.

When excavation tools are moved through a soil with adhesive properties, i.e. a pipe-lay trencher, the trencher is subjected to sliding resistance consisting out of a adhesive and a frictional part. This sliding resistance is described by (Stafford and Tanner, 1976) and follows a Coulomb-type expression, as depicted in Figure 3.12.

Where a_s or simply a is the adhesive shear strength and δ the external friction angle of the clay, also called the soil to metal friction angle.

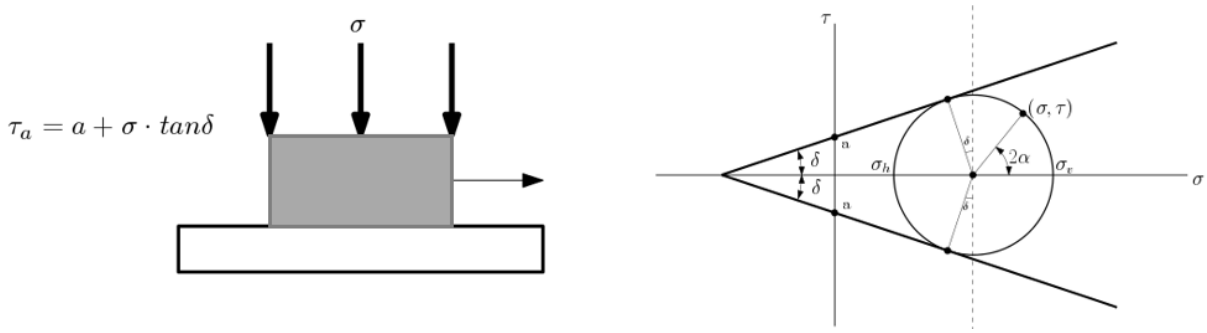

FIGURE 3.12: Direct shear test (soil-foreign body) with the Mohr-Coulomb failure criterion

Both cohesion and adhesion are recoverable forces, meaning that they can be stuck back together after they have been teared apart. (X. Chen, Miedema, and Rhee, 2015) Furthermore, cohesion and adhesion are strain rate dependent: the internal and external shear strength C and A increase with an increasing strain rate.

Chapter 4

The Two Dimensional Soil Cutting Theory

In this chapter the theory for two dimensional soil cutting is discussed. First, an overview of the various cutting mechanisms is presented in Paragraph 4.1, whereafter a more detailed description of the theory for applications in cohesive soils is discussed in Paragraph 4.2.

4.1 Overview of The Various Cutting Mechanisms

Hatamura and Chijiiwa identified three different cutting mechanisms in soil excavation processes: the so-called "shear type", "flow type" and "tear type". (Hatamura and Chijiiwa, 1975; Hatamura and Chijiiwa, 1976a; Hatamura and Chijiiwa, 1976b; Hatamura and Chijiiwa, 1977a; Hatamura and Chijiiwa, 1977b) The shear type is typically encountered when cutting soils with an angle of internal friction. The flow and tear type occur in soils without an angle of internal friction. A fourth cutting mechanism for soils without an angle of internal friction was identified by Miedema, 1992 the "curling type". A schematic overview of these four cutting mechanisms is given in Figure 4.1. (Miedema, 2015, X. Chen, Miedema, and Rhee, 2015)

4.2 Cutting Theory for Cohesive Soils

The cutting of clay in dredging applications or deep-sea mining (undrained, high strain rates) follows the so-called $\phi = 0$ concept: effectively there is no relation between excess normal stresses and shear stresses in the clay so the soil behaves like there is no angle of internal friction. Because, when clay is compressed at high strain rates, the water in the pores cannot flow away because of the low permeability of the clay. The excess pressure is carried by the water in the pores and not by the soil skeleton, so the grain stresses will not change. If there is no change in grain stresses, the shear stress according to Coulomb friction does not change. So the soil behaves like there is no angle of internal friction, or $\phi = 0$. (Miedema, 2015) This phenomenon will be used to simplify the general cutting equations to the clay cutting equations.

The cutting mechanisms typically encountered in clay cutting are the flow type, the tear type and the curling type. Typically the flow type will occur, but the tear type and the curling type can occur under specific conditions:

- When the blade height h_b is small with respect to the layer thickness h_i, the adhesion a is small compared to the cohesion c and the blade angle α is relatively small, the blade will generate tensile cracks in the soil and the tear type will occur.
- When the blade height h_b is big compared to the layer thickness h_i, the adhesion is large with respect to the cohesion c and the blade angle is relatively big, the contact length between length curling type will occur. (Miedema, 2015)

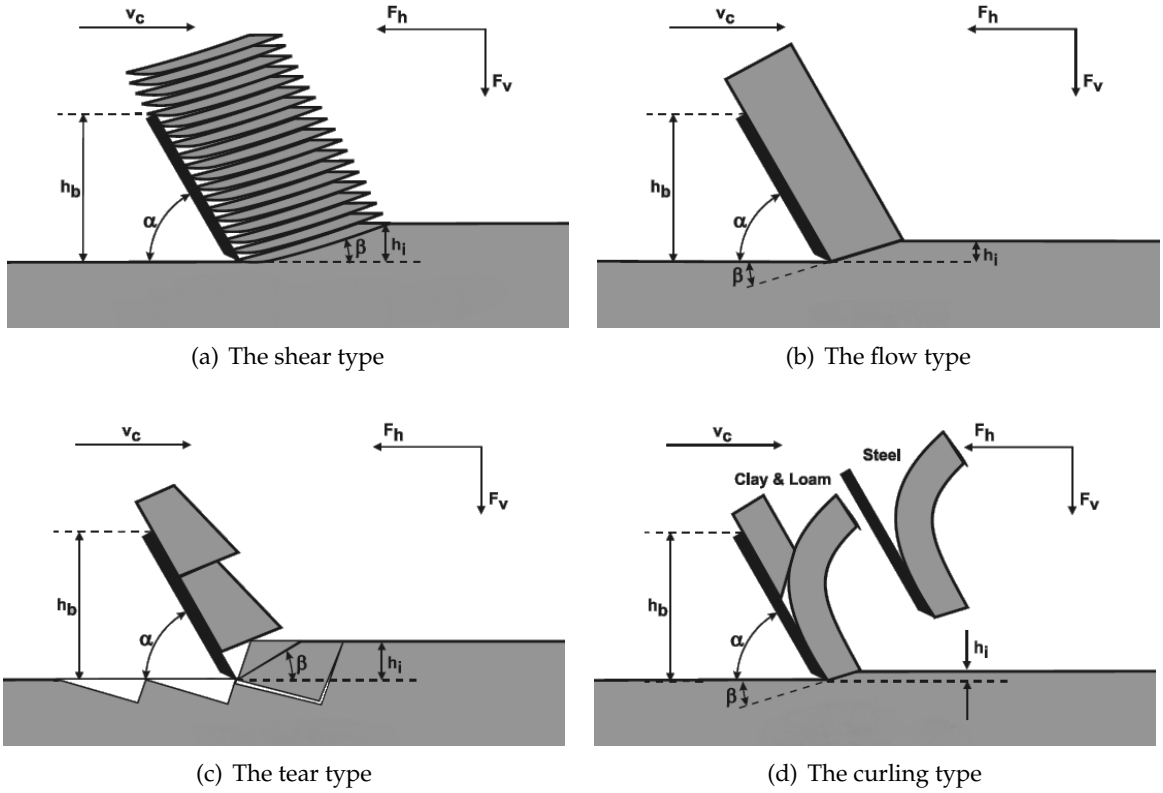

(a) The shear type

(b) The flow type

(c) The tear type

(d) The curling type

FIGURE 4.1: The different types of cutting mechanisms encountered in excavation processes. Retrieved from Miedema, 2015.

4.3 The Flow Type

As stated in the previous paragraph, the flow type is the most common failure mechanism in the cutting of clay. Therefore the derivation of the cutting forces will be performed for the flow type; the cutting equations for the tear type and the curling type can be derived from these equations.

In clay cutting the cohesive and adhesive forces play a dominant role; gravity, inertial forces and pore pressures can be neglected. Furthermore, because of the $\phi = 0$ concept, the angle of internal and external friction are 0. An schematic overview of the forces on the layer cut and the forces on the cutting blade in clay cutting according to the flow type is given in Figure 4.2. (Miedema, 2015)

Figure 4.2(a) depicts the forces on a layer cut of clay. In Figure 4.2(a) the blade is moving from left to right with a constant speed v_c. The blade angle is called α and the angle of the shear plane β. The blade has a height h_b and cuts a layer with a thickness of h_i. The blade experiences a horizontal cutting force F_h positive in the leftward direction and a vertical cutting force F_v positive in the downward direction. (Miedema, 2015)

The forces acting on the layer in Figure 4.2(a) are:

- A normal force N_1 acting on the shear surface resulting from the effective grain stresses.
- A shear force C acting on the shear surface as a result of the cohesion c or cohesive shear strength τ_c of the clay. This force C is equal to the area of the shear plane multiplied with c of τ_c.

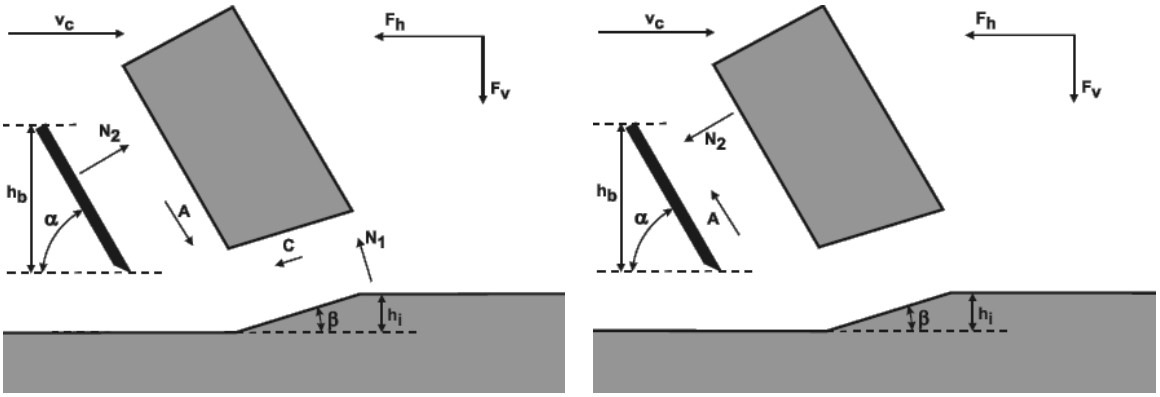

(a) Forces on the layer cut in clay (b) Forces on the blade in clay cutting

FIGURE 4.2: Forces on the layer cut and forces on the blade in clay cutting. Retrieved from Miedema, 2015.

- A normal force N_2 acting on the soil layer as a result of the effective grain stresses.
- A shear force A as a results of the adhesion a or adhesive shear strength τ_a of the clay. This force A is equal to the contact area between the blade and the soil layer multiplied with a or τ_a.

In the same way, the forces acting on the blade, depicted in Figure 4.2(b), are:

- A normal force N_2 acting on the blade as a result of the effective grain stresses.
- A shear force A as a results of the adhesion a or adhesive shear strength τ_a of the clay. This force A is equal to the contact area between the blade and the soil layer multiplied with a or τ_a.

As stated above cohesive and adhesive forces are dominant so gravity, inertial forces and pore pressures can be neglected. Applying the horizontal equilibrium of forces yields Equation 4.1

$$\sum F_h = N_1 \cdot sin(\beta) + C \cdot cos(\beta) - A \cdot cos(\alpha) - N_2 \cdot sin(\alpha) \tag{4.1}$$

Taking the vertical equilibrium of forces gives Equation 4.2.

$$\sum F_v = -N_1 \cdot cos(\beta) + C \cdot sin(\beta) + A \cdot sin(\alpha) - N_2 \cdot cos(\alpha) \tag{4.2}$$

From the equilibria in Equations 4.1 and 4.2 the equations for a horizontal cutting force in the direction of the cutting velocity v_c and a vertical cutting force perpendicular to this force can be derived. The equations for the horizontal and vertical cutting force are given in Equations 4.3 and 4.4. (Miedema, 2015)

$$F_h = N_2 \cdot sin(\alpha) + A \cdot cos(\alpha) \tag{4.3}$$
$$F_v = N_2 \cdot cos(\alpha) - A \cdot sin(\alpha) \tag{4.4}$$

Which finally gives Equations 4.5 and 4.6 for the cutting forces on the blade in horizontal and vertical directions:

$$F_h = \lambda \cdot c \cdot h_i \cdot w \cdot \frac{\frac{sin(\alpha)}{sin(\beta)} + r \cdot \frac{sin(\beta)}{sin(\alpha)}}{sin(\alpha + \beta)} \tag{4.5}$$

$$F_v = \lambda \cdot c \cdot h_i \cdot w \cdot \frac{\frac{cos(\alpha)}{sin(\beta)} - r \cdot \frac{cos(\beta)}{sin(\alpha)}}{sin(\alpha + \beta)} \tag{4.6}$$

$$r = \frac{a \cdot h_b}{c \cdot h_i} \tag{4.7}$$

Where F_h is the horizontal cutting force which is aligned with the direction of the cutting blade [N] while F_v is the vertical cutting force [N],α is the cutting angle [-], β is the angle of the shear plane with the direction of the cutting velocity [-], λ is the strengthening factor which follows the fact that when the cutting velocity increases, the clay gets stronger. c is the cohesive shear stress [Pa] while a is the adhesive shear stress [Pa], h_i is the cutting depth [m] and h_b is the blade height [m], w is the width of the blade [m], and r is the ratio between adhesion and cohesion [-].

Again, it is important to note that the model developed by Miedema is based using assumptions of constant, average forces on the shear plane in two dimensions.

Part II

Literature Review on the Cohesion-Adhesion Relation

Chapter 5

Existing Models for the Adhesion Factor

In this chapter existing data and models for the adhesion factor are discussed and new models for dredging applications are presented. Reviewed models are separated and discussed in two categories: models for the adhesion factor based on the total shear resistance and models for the adhesion factor based on true adhesion or stickiness.

5.1 Adhesion Factor Models Based on Total Shear Resistance

In geotechnical engineering, and in particular foundation engineering, the α-method is a common used total stress analysis for the side resistance capacity of shaft foundations in cohesive soils. In this method, the side resistance capacity is related to the soil undrained shear strength by an empirical coefficient denoted as α which is, as mentioned earlier, the adhesion factor. With the adhesion factor, the side resistance of a pile foundation in cohesive soil is calculated using Equation 5.1. (Y. Chen et al., 2011)

$$Q_s(\alpha) = \pi B \sum_{n=1}^{N} \alpha c_u t \tag{5.1}$$

Where Q_s is the side resistance capacity of the pile foundation [kPa], α the adhesion factor [-], c_u the undrained shear strength of the soil [kPa], B the foundation width [m] and t the the thickness [m]. (Y. Chen et al., 2011)

Many authors have contributed with publications on the adhesion factor, typically by evaluating the adhesion factor as a function of the undrained shear strength c_u of the soil. An overview of the most frequently used α-c_u relations is depicted in Figure 5.1.

The α-c_u relations depicted in Figure 5.1 are based on empirical correlations of soil undrained shear strength over the foundation depth, using primarily driven pile data. (Y. Chen et al., 2011) From Figure 5.1 it is clear that allot of variation exists between different models. These variations originate primarily from differences in tested soils, foundation geometry and testing methods. In practice, the adhesion factor used in foundation design are obtained from applicable design standards.

It is important to note that the empirical adhesion factor used in foundation engineering has a different definition than the adhesion factor required for practical application of the Delft Clay Cutting model. In the Delft Clay Cutting theory, the adhesion factor is defined as the ratio between a soil's adhesion and cohesion, whereas the empirical adhesion factor used in foundation engineering is a coefficient providing a indication for the total shear resistance of the foundation, so consisting of both adhesion and friction. This is a direct result from the calculation method used to determine the empirical adhesion factor, which is shown in Equation 5.2.

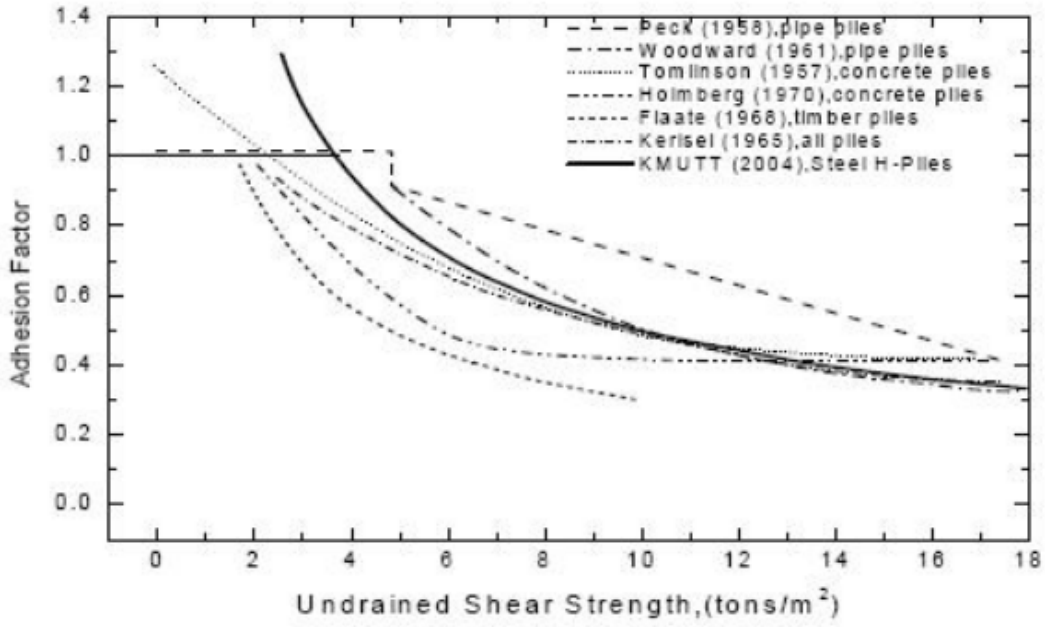

FIGURE 5.1: An overview of the most frequently used α-c_u relations (1 ton/m^2 is approximately 10 kPa). Retrieved from `http://www.thaicontractors.com`

$$\alpha = \frac{Q_s(L)}{(\pi B t c_u)} \tag{5.2}$$

Where Where Q_s is the side resistance capacity of the pile foundation [kPa], α the adhesion factor [-], c_u the undrained shear strength of the soil [kPa], B the foundation width [m] and t the the thickness [m]. As shown in Equation 5.2, the empirical adhesion factor is calculated using data from field load results, resulting in an empirical coefficient which, as mentioned earlier, is a measure for the total skin shear resistance consisting of both adhesion and friction. Therefore, this empirical coefficient for a given undrained shear strength is typically higher than the adhesion factor based on the true adhesion of the soil. Furthermore, for high undrained shear strength, this empirical adhesion factor goes to a constant value unequal to zero (as depicted in Figure 5.1), where, if we look at true adhesion (stickiness) of a cohesive soil, it would be expected to drop to zero for high undrained shear strengths.

5.2 Adhesion Factor Models Based on Adhesive Resistance

In the review of the available literature on adhesion and frictional resistance between clay and solid bodies, no existing models indicating the relation between the adhesion-factor α (defined as a/c) and the undrained shear strength c_u, either analytic or empirical, could be found. However, several authors conducted experiments on the The frictional behaviour of soil-steel interfaces, publishing data from which the adhesion a and undrained shear strength c_u for a variety of soils can be obtained and a model can be constructed. An overview and summary of these soils and there properties is presented in Table 5.1.

TABLE 5.1: An overview of the soils and there properties obtained in the literature review.

Class	Type of Clay	Source	Soil Mechanical Parameters		
			c_u [kPa]	a [kPa]	α [-]
Very Soft	Illite	Littleton, 1976	19.0	16.0	0.84
Soft	River Clay	Van Der Wielen, 2014	26.9	15.6	0.58
Soft	K122*	Kooistra et al., 1998	28.0	18.5	0.66
Intermediate	Unknown	Cappelletto et al., 1998	40.0	19.2	0.48
Intermediate	Unknown	Cappelletto et al., 1998	48.0	19.0	0.4
Firm	River Clay	Kooistra et al., 1998	75.0	5.1	0.07
Stiff	River Clay	Kooistra et al., 1998	129.0	0.0	0
Stiff	River Clay	Kooistra et al., 1998	149.0	0.0	0
Very Stiff	River Clay	Kooistra et al., 1998	238.0	0.0	0

* Commercial Potters Clay

The α-c_u data presented in Table 5.1 was scattered and analyzed to find the correlation between the adhesion factor α and the undrained shear strength c_u. On a linear axis system, displayed in Figure 5.2(a), the adhesion factor clearly shows what looks like a logarithmic or exponential decaying trend for an increasing undrained shear strength. To check this hypothesis, the adhesion factor is plotted versus the undrained shear strength in a semi-logarithmic plot with a logarithmic x-axis for c_u, as depicted in Figure 5.2(b).

In the semi-logarithmic plot displayed in Figure 5.2(b) the scattered data shows a negative linear trend, indicating that the hypothesis was correct. Therefore logarithmic and exponential functions are chosen as the basis of the literature model, in combination with either a linear or constant value function for low undrained shear strengths. Three possible combinations of functions are reviewed: a linear-exponential model, a constant-logarithmic model and a constant-exponential model. All models are depicted in Figure 5.3.

Linear-Exponential Model

In Figure 5.3(a) and 5.3(b) the linear-exponential model is depicted as the dashed line (overlapped by the solid line for $c_u > 40$ [kPa]). Both the linear and exponential functions represent the least-squares fit to the literature data. An overview of the model is given in Equation 5.3.

$$\begin{aligned} \alpha &= 1.08 - 0.017 c_u \quad \text{for} \quad c_u \leq 40 \quad [kPa] \\ \alpha &= 2.1019 \cdot e^{-0.046 c_u} \quad \text{for} \quad c_u > 40 \quad [kPa] \end{aligned} \tag{5.3}$$

Looking at the linear-exponential model in Figure 5.3, the conclusion can be drawn that the linear part of the model slightly underestimates the adhesion factor for low undrained shear strengths. The exponential part however provides a good description of the adhesion factor, especially at higher undrained shear strengths.

Constant-Exponential Model

The constant-exponential model is depicted as the solid line in Figure 5.3(a) and 5.3(b) (overlapped by the dotted line for $cu < 15$. In this model the adhesion factor is set as a constant factor of 1 up to a undrained shear strength of 20 [kPa], after which the adhesion factor is described by the same exponential decaying model according to the least-squares method as in the linear-exponential model. An overview of the model is given in Equation 5.4.

$$\begin{aligned} \alpha &= 1 && \text{for} \quad c_u \leq 20 \quad [kPa] \\ \alpha &= 2.1019 \cdot e^{-0.046 c_u} && \text{for} \quad c_u > 20 \quad [kPa] \end{aligned} \tag{5.4}$$

From both Figure 5.3(a) and 5.3(b), it can be concluded that the exponential decaying model provides an excellent description of the literature data. Because no data is available at undrained shear strengths lower than 15 [kPa], the constant section of the model can not be validated.

Constant-Logarithmic Model

In Figure 5.3(a) and 5.3(b) the constant-logarithmic model is depicted as the dotted line. In this model the adhesion factor is set as a constant factor of 1 up to a undrained shear strength of 15 [kPa], after which the adhesion factor is described by a least-squares logarithmic fit up to a undrained shear strength of 90 [kPa]. For undrained shear strengths larger than 90 [kPa], the adhesion factor is again set at a constant factor, this time at 0. An overview of the model is given in Equation 5.5.

$$\begin{aligned} \alpha &= 1 && \text{for} \quad c_u \leq 15 && [kPa] \\ \alpha &= -0.516 \cdot \log(c_u) + 2.3392 && \text{for} \quad 20 < c_u \leq 90 && [kPa] \\ \alpha &= 0 && \text{for} \quad c_u > 90 && [kPa] \end{aligned} \tag{5.5}$$

The logarithmic model provides a good description of the reviewed data, however not as good as the exponential model. In Chapter 7, the developed models will be validated with experiments to see which model provides the best description of the relation between the adhesion factor and the undrained shear strength.

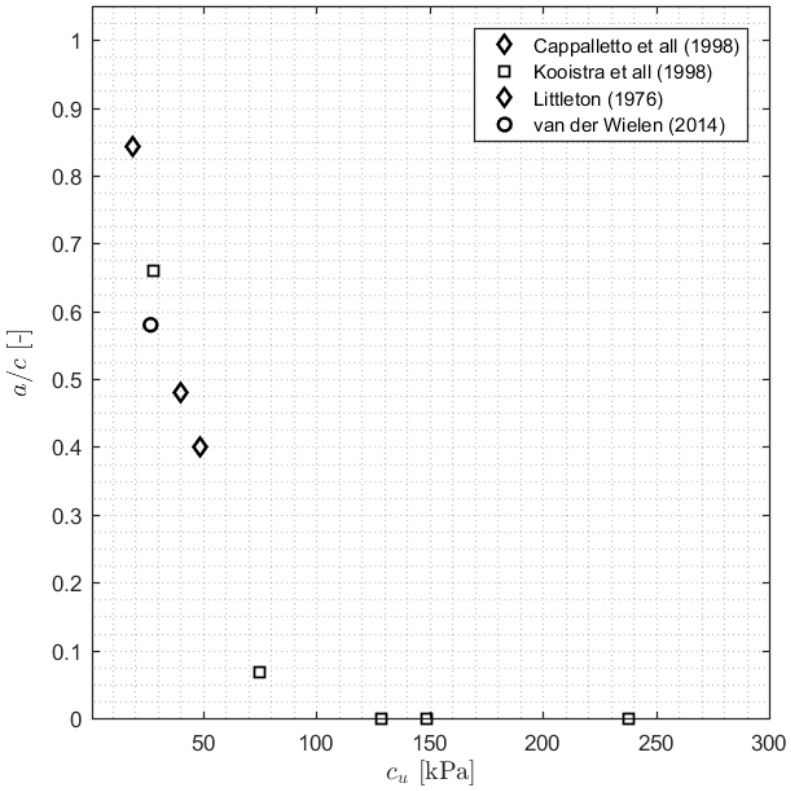

(a) Plot showing α-c_u data obtained from various authors.

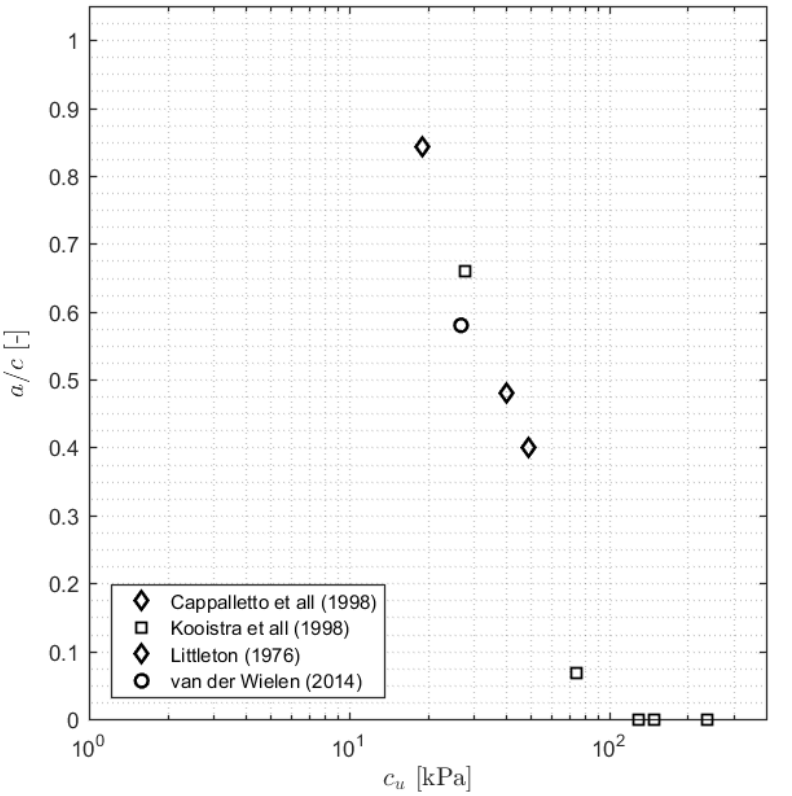

(b) Semi-logarithmic plot showing α-c_u data obtained from various authors.

FIGURE 5.2: Linear and semi-logarithmic plot of the adhesion factor versus the undrained shear strength as obtained from literature.

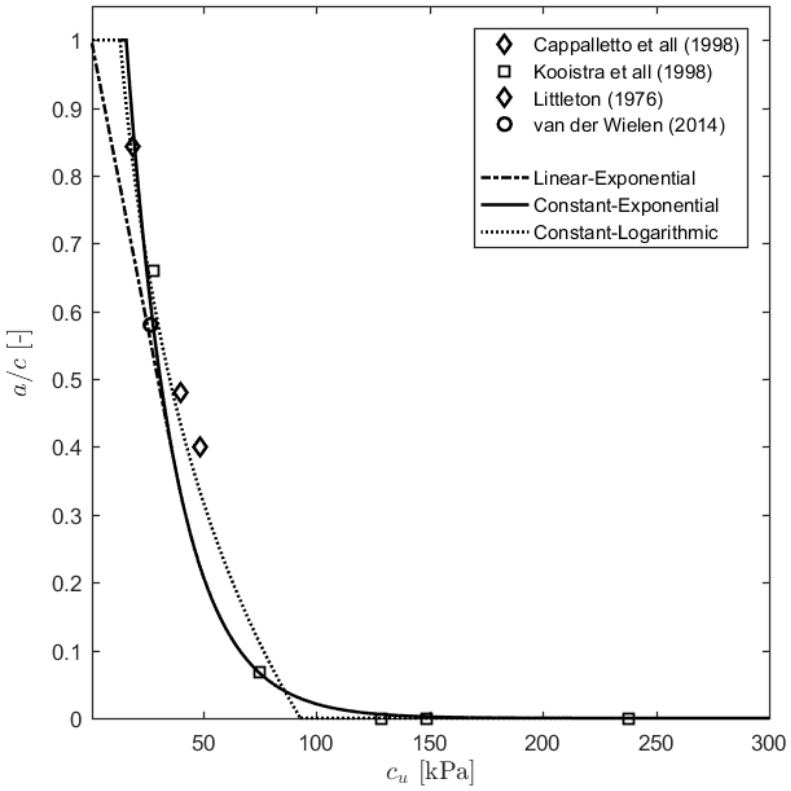

(a) Plot showing α-c_u data obtained from various authors.

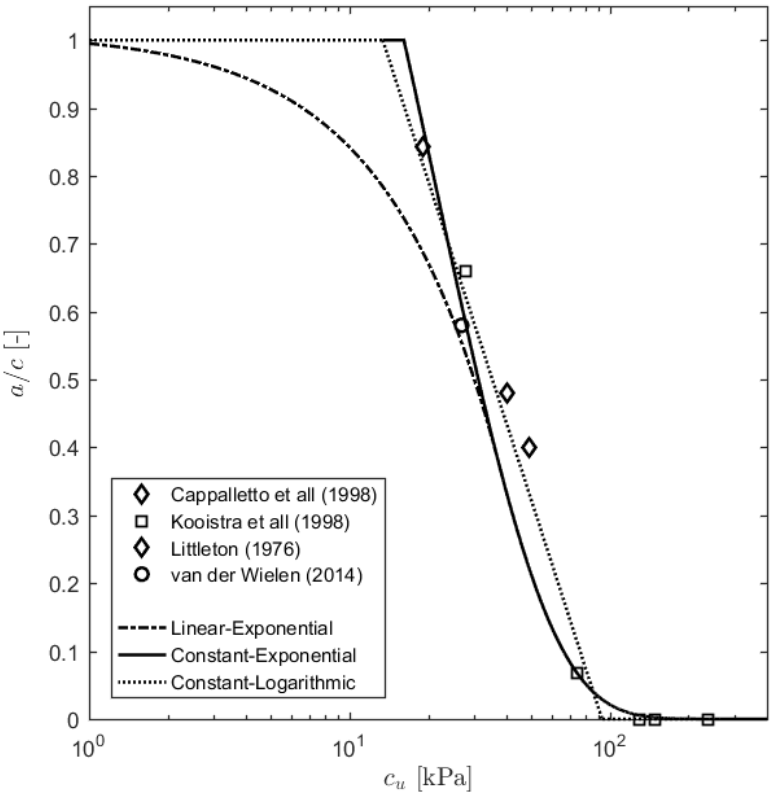

(b) Semi-logarithmic plot showing α-c_u data obtained from various authors.

FIGURE 5.3: Linear and semi-logarithmic plot of the adhesion factor versus the undrained shear strength as obtained from literature.

Part III

Experiments and Results

Chapter 6

Experimental Study

As mentioned in Chapter 1, a fundamental relation between cohesion and adhesion in clays has not been established yet. In the previous chapter, three models for the cohesion-adhesion relationship have been constructed with data obtained from literature. To test this relationship, experimental research is performed which will be discussed in this chapter. First, the two design concepts for an adhesion test setup will be discussed in Paragraph 6.1. These concepts lead up to the final setup used for the experiments in Paragraph 6.2. Subsequently, the experimental matrix containing the various tests is presented in Paragraph 6.3. Finally, the experimental procedure is explained in detail in Paragraph 6.4.

6.1 Adhesion Test Setup Design

Because the internal shear strength or cohesion and the internal friction angle ϕ are two properties often used to characterize a cohesive soil, direct shear testing equipment applying to ASTM-standards is readily available. However, this does not apply for external shear strength or adhesion and external friction angle of soils δ. Therefore a new experimental setup needs to be designed and constructed. First, the design criteria for an Adhesion Test Setup (ATS) are listed below:

- The experimental setup should be able to measure the external shear strength or adhesion of the cohesive soil sample.
- With the results from the tests performed on the setup, it should be able to indicate and describe the presence of an external friction angle.
- The experimental setup should enable testing at adjustable constant speeds up to 10 mm/s.
- With the experimental setup, it should be possible to perform tests on cohesive soils with a undrained shear strength from $\pm$ 10 kPa ranging up to $\pm$ 300 kPa.
- The experimental setup should have the possibility to reproduce tests to indicate the error margin on the test results.
- As an additional optional requirement, the experimental setup enable submerged testing of the sample's adhesion.

Two design concepts for the setup according to these criteria are elaborated on: the horizontal adhesion test setup and the vertical test setup. The final design is chosen from these concepts.

6.1.1 Horizontal Adhesion Test Setup

In the first concept design, a metal blade is pulled through two halves of a soil sample in a horizontal arrangement: this is depicted in Figure 6.1. In Figure 6.1, black represents the sample container, light-gray the soil sample and dark gray auxiliary equipment like sensors and drive systems.

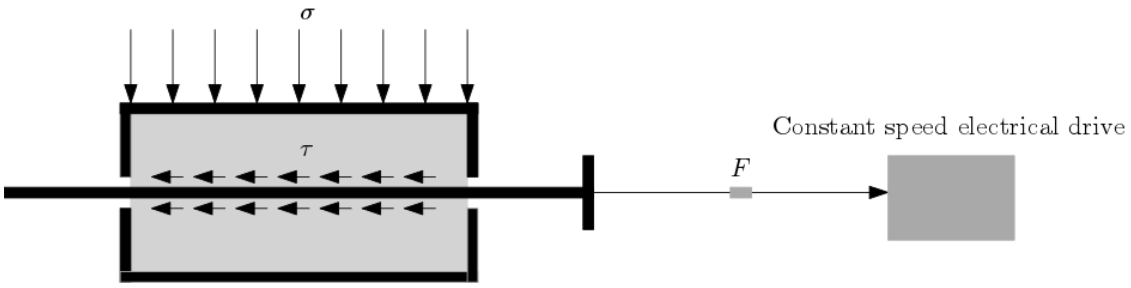

FIGURE 6.1: The Horizontal Adhesion Test Setup Concept.

In this concept, the one-sided applied normal pressure σ can be varied, either through adding and subtracting weights or varying applied pressure by a pneumatic or hydraulic piston. The blade is pulled from the clay at preset, adjustable constant speed whilst the force is recorded by the force sensor between the blade and the electrical drive-system.

With this concept setup, the tangential resistance τ can be obtained from the recorded pulling force F according to Equation 6.1.

$$\tau = \frac{F}{2A} \tag{6.1}$$

Where A is the contact area between the metal blade and one half of the clay in m^2. Conducting pull-out tests at a fixed constant speed at increasing normal pressures σ gives the τ-σ-relation for a soil sample. This relations is used to obtain the Mohr-Coulomb failure criterion and, finally, use the relation to obtain the adhesion a and external friction angle δ. This horizontal setup is easy to construct and operate, but has a disadvantage. Due to the horizontal arrangement, submerged testing is not possible without waterproof equipment, advanced sealing for moving parts or a gear- or pulley-system to enable vertical pulling.

6.1.2 Vertical Adhesion Test Setup

In the second concept, the possibility to conduct submerged experiments is taken into account in the design of the setup. The vertical arrangement, as depicted in Figure 6.2, makes it possible to place the auxiliary equipment above possible water for submerged conditions. Again, black depicts the soil sample and the blade, light-gray the soil sample and dark-gray the auxiliary equipment.

Just as in the horizontal setup, the blade is pulled from the soil sample at a constant speed whilst the force is recorded. Again, the tangential resistance τ can be calculated using Equation 6.1. The major difference however, is in the way the normal pressure σ is applied: in the horizontal setup is it sufficient to apply the normal pressure to one side of the soil-sample, but in the vertical the normal pressure needs to be applied to both sides to ensure even pressure between the soil sample and the blade.

To check the feasibility of the concept, the Vertical Adhesion Test Setup concept was developed further. A setup was designed using stainless steel standard box-, channel- and I-profiles and available linear bearings, sensors and actuators. The Vertical Adhesion Test Setup (ATS) is shown in Figure 6.3. A three-dimensional render and detailed drawings of the Vertical Adhesion Test Setup are enclosed in Appendix A.

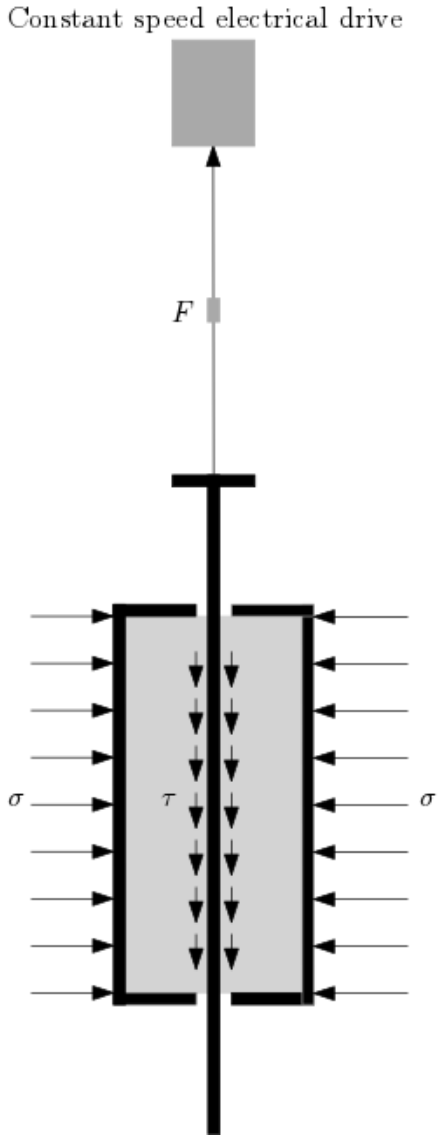

FIGURE 6.2: The Vertical Adhesion Test Setup Concept.

As depicted in Figure 6.3, the Vertical Adhesion Test Setup is comprised of five main elements:

1. A welded and bolted frame of standard box, channel and I-profiles holding the moving frame (2), sample container (4) and electrical actuator (5) in place.

2. A rectangular frame free to move linear in the vertical direction. A more detailed overview of the frame-blade assembly is enclosed in Appendix A.

3. The metal blade to be pulled from the clay. The blade is attached to the frame via a force sensor. A more detailed overview of the frame-blade assembly is enclosed in Appendix A.

4. The sample container consisting of two halves. Before testing, two equal blocks of clay are placed in the two sample container halves, after which stacks of parallel, in series placed disk spring washers are used to ensure clamping at a preset normal pressure σ. Furthermore, the sample container is placed on a metal stand which can be enclosed to facilitate submerged testing. A detailed overview of the sample container with the disk spring mechanism is enclosed in Appendix A.

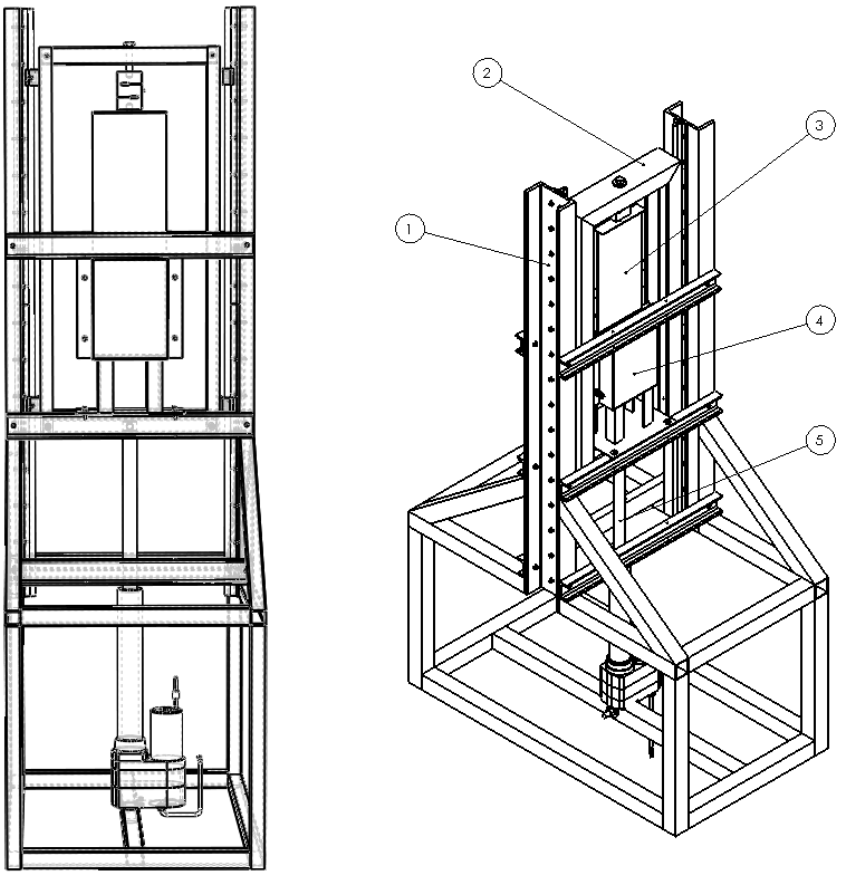

FIGURE 6.3: The Vertical Adhesion Test Setup Concept.

5. An electrical actuator capable of pulling the frame from the clay at a constant speed, up to high normal pressures.

First and foremost, the goal of this research is to analyze the cohesion-adhesion relation for cohesive soils. It was concluded that submerged testing was not required to be able to achieve the goals of this research. Furthermore, concerns were raised with respect to the rigidity of the designed vertical setup. And, finally, it was decided that the disk-spring clamping mechanism is not practical to use when conducting a large number of experiments, because of the precision required in the preset spring deflection to ensure clamping at a specif normal pressure. Therefore, the decision was made to construct a experimental setup according to an adjusted version of the Horizontal Adhesion Test Setup concept, depicted in Figure 6.4.

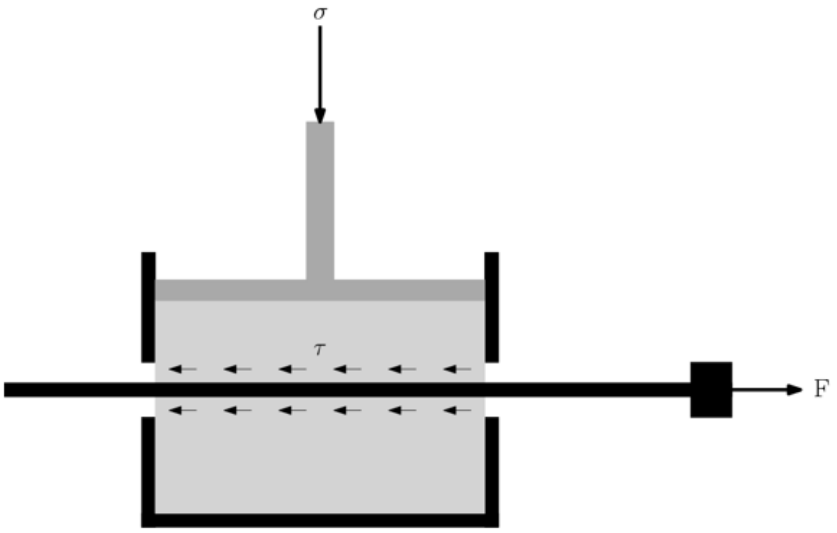

FIGURE 6.4: The final concept for the design of the Adhesion Test Setup.

6.2 Experimental Setup

6.2.1 Adhesion and External Friction Angle

The final experimental setup is designed in a collaboration by The Delft University of Technology and The National Engineering Research Center for Dredging Technology and Equipment located in Shanghai, China. The test equipment was constructed by the Shanghai Leao Test Instrument Company and complies with the Chinese T1129-2006 and T1130-2006 specifications in the JTG E50-2006 Test Procedure for Geo-synthetics for Highway Engineering. The final design for the test equipment is depicted in Figure 6.5.

The experimental rig depicted in Figure 6.5 is build up from 14 main components:

1. Main casing to shield and protect electrical equipment and tubing.
2. Pneumatic cylinder capable of applying normal pressures up to 200 kPa.
3. Pressure plate: distributes pressure from the cylinder over the soil surface.
4. Slotted soil container for shearing.
5. Clamping mechanism: clamps the metal blade used for shearing to the linear pulling mechanism.
6. Force sensor to measure the pulling force.
7. Linear electrical screw drive
8. Reduction gearbox to provide a constant pulling speed.
9. Encoder to measure speed of the screw drive.
10. Displacement sensor to measure blade displacement.
11. Pressure plate: distributes pressure from the cylinder over the soil surface (same as (3)).

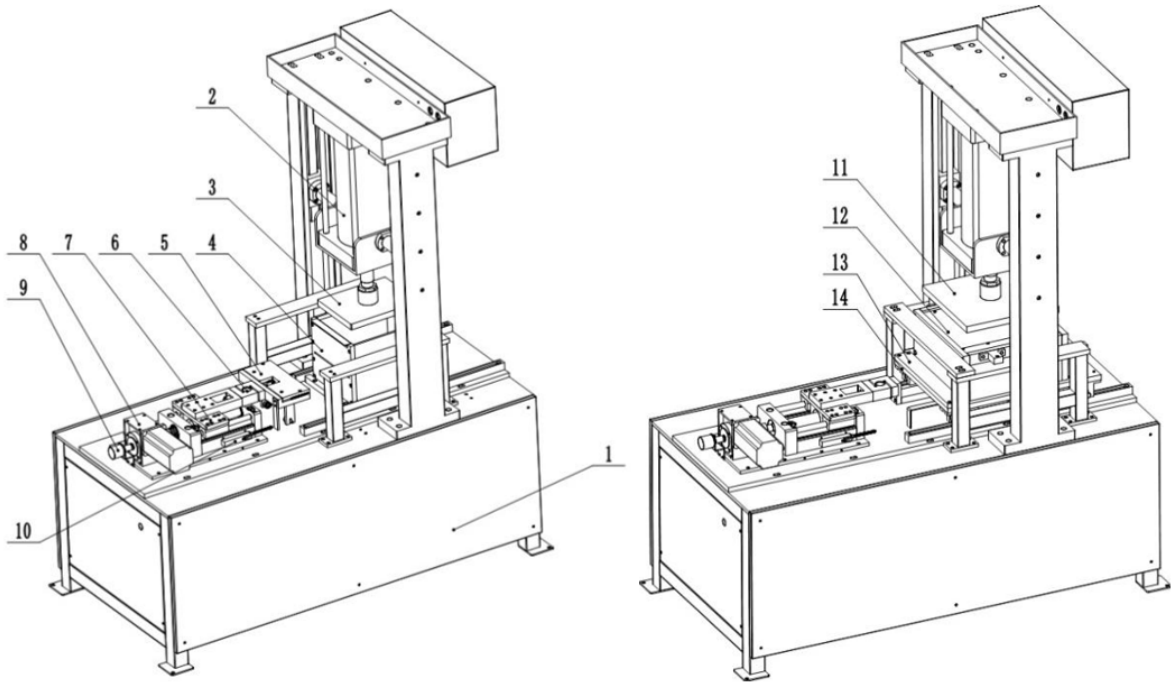

FIGURE 6.5: A schematic overview of the final experimental setup used for measuring soil-metal friction.

12. Blocker to keep the soil container at its position.
13. Metal blade used to measure soil-metal resistance.
14. Blocker to keep the soil container at its position.

Pictures of the setup during tests are presented in Appendix A.2.

6.2.2 Cohesion and Internal Friction Angle

The direct shear apparatus used in the experiments is constructed by the Nanjing Soil Instrument Factory Co. Ltd. and consists of four parallel direct shear boxes. A picture of the apparatus is enclosed in Appendix A.3. Figure 6.6 gives a schematic representation of the direct shear box used for the undrained direct shear tests on the consolidated soil samples. It consists out of two halves split in the horizontal center plane. Porous rocks are located both at the bottom and the top of the shear box to facilitate drained shear tests. The normal load, applied via a pressure pad, can be varied by adding and subtracting weights via a lever mechanism. Finally, the top half is sheared with the help of a constant speed electrical screw drive mechanism.

6.2.3 Blade Roughness

Roughness measurements were carried out with a surface profile gauge to measure the roughness of the blade. A total of 15 measurements was performed, giving an average blade roughness of 72.9 μm.

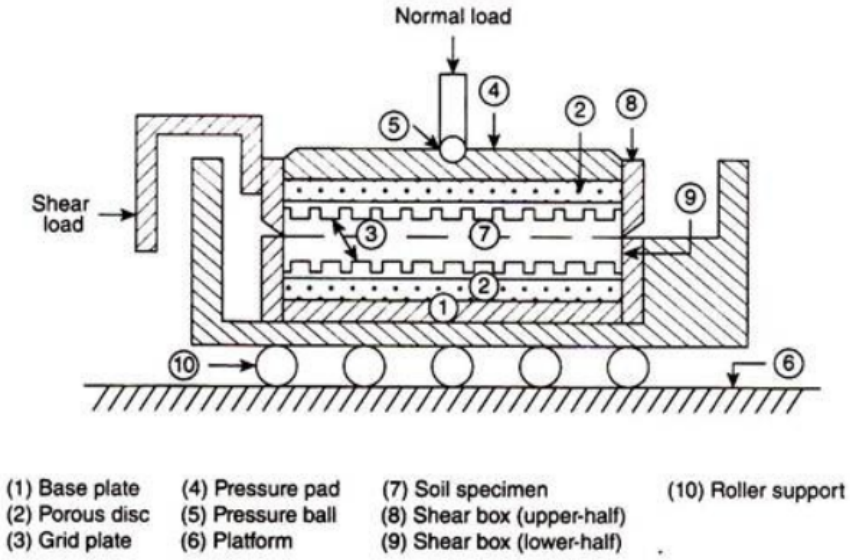

FIGURE 6.6: A schematic overview of the direct shear boxes used. Retrieved from `http://www.soilmanagementindia.com/soil/shear-strength`

6.3 Experimental Matrix

Before testing can commence, an overview and a planning of all tests is required to make sure that all planned tests can be performed within the available time frame. To see the effect of the clay mineral type, two soils from different locations in the People's Republic of China are included. Furthermore, soil samples will be consolidated for various amounts of time to be able to analyze the cohesion-adhesion relation over a wide range of undrained shear strengths. An overview of this experimental planning is shown in the experimental matrix given in Table 6.1.

TABLE 6.1: Experimental Matrix

	Sample	Preconsolidation up to	Adhesion					Cohesion				Water Content	
Soil 1	1-1	c_{u1}	σ_1	σ_2	σ_3	σ_4	σ_5	σ_1	σ_2	σ_3	σ_4	ww_1	ww_2
	1-2	c_{u2}	σ_1	σ_2	σ_3	σ_4	σ_5	σ_1	σ_2	σ_3	σ_4	ww_1	ww_2
	1-3	c_{u3}	σ_1	σ_2	σ_3	σ_4	σ_5	σ_1	σ_2	σ_3	σ_4	ww_1	ww_2
	1-4	c_{u4}	σ_1	σ_2	σ_3	σ_4	σ_5	σ_1	σ_2	σ_3	σ_4	ww_1	ww_2
	1-5	c_{u5}	σ_1	σ_2	σ_3	σ_4	σ_5	σ_1	σ_2	σ_3	σ_4	ww_1	ww_2
Soil 2	2-1	c_{u6}	σ_1	σ_2	σ_3	σ_4	σ_5	σ_1	σ_2	σ_3	σ_4	ww_1	ww_2
	2-2	c_{u7}	σ_1	σ_2	σ_3	σ_4	σ_5	σ_1	σ_2	σ_3	σ_4	ww_1	ww_2
	2-3	c_{u8}	σ_1	σ_2	σ_3	σ_4	σ_5	σ_1	σ_2	σ_3	σ_4	ww_1	ww_2
	2-4	c_{u9}	σ_1	σ_2	σ_3	σ_4	σ_5	σ_1	σ_2	σ_3	σ_4	ww_1	ww_2
	2-5	c_{u10}	σ_1	σ_2	σ_3	σ_4	σ_5	σ_1	σ_2	σ_3	σ_4	ww_1	ww_2

Blade pull out tests are performed at one fixed speed at five incremental increasing normal pressures for each sample, to be able to obtain an accurate measurement of the tangential resistance (thus adhesion and the external friction angle). Undrained direct shear tests are performed at one fixed speed and four normal pressures as this is the maximum amount of specimens the apparatus can hold per direct shear test. Furthermore, four direct shear tests give an accurate result for the sample's undrained shear strength. Finally, for each sample, two measurements of the

water content (weight percent water) are performed and averaged to obtain the sample's water content.

6.4 Soils

Two soils were used in the cohesion-adhesion experiments. Both soils were obtained from active dredging sites in the People's Republic of China: soil 1 originates from Wuhan and soil 2 originates from Lianyungang. Immediately after dredging, both soils were packed and send to the research facility where they were stored in a humidified cabinet. Furthermore, part of the two soils was prepared using air drying, crushing and sieving (1mm) and mixed with water to a certain water content to conduct Atterberg Limit tests according to the Chinese JTG E-40 standard. The results for the atterberg limit tests are depicted in Appendix A.4. Finally, X-ray diffraction tests were performed by the Shanghai OKanalysis Center to determine the mineralogy of the soils. The results for the X-ray diffraction tests are depicted in Appendix A.5.

An overview of the main properties of the used soils is presented in Table 6.2.

TABLE 6.2: The main soil properties of the used soils

Soil	Location	Dry bulk density $[kg/m^3]$	Minerals present	Plastic Limit (w/w/%)	Liquid Limit (w/w/%)
1	Wuhan	2180	Quartz, Calcite, Graphite, Kyanite, Albite, Cordierite, Orthoclase, Anorthite, Anatase, Almadine	14.2	23.4
2	Lianyungang	1950	Quartz, Graphite, Sylvite, Spinel, Sodalite, Siderite, Rutile, Magnetite, Magnesite, Hematite, Calcite	12.2	25.7

6.5 Procedure

6.5.1 Adhesion and External Friction Angle Tests

To ensure full saturation, the soil was placed in a large container filled with water for at least three days. Subsequently the soil was put in the metal soil container, shown by (4), separated in the middle by a plastic film; in this way the soil was split in two halves which makes for easy blade placement. The container containing the soil was placed on the test equipment and a constant vertical pressure was applied for a predetermined period while drainage was allowed. In this way, consolidation of the soil up to the desired shear strength is achieved.

After consolidation the plastic film and the top half of the consolidated clay were removed from the container. First, both surfaces were rolled to ensure a smooth surface, after which the blade was placed in the correct position on the bottom half of the soil. Subsequently the top half of the soil was put into place on top of the blade and the blade was clamped to the test equipment using the bolted clamping mechanism (5).

The specific normal pressure for the test was applied and after the pressure was maintained at a constant value for 30 seconds, the blade pull out test was commenced. For each consolidated

soil sample, five blade pull out test were performed at normal pressures ranging from 40 kPa up to 200 kPa, at incremental steps of 40 kPa. Between two tests, the top half of the consolidated soil and the blade were removed from the test setup. The blade was cleaned to remove any residual soil and the consolidated soil was rolled again to have equally smooth surfaces between tests. The tests were performed at a constant speed of 1 mm/s and recorded for a distance of 100 mm. The test results could be viewed and exported using the build-in 7-inch touchscreen.

6.5.2 Cohesion and Internal Friction Angle Tests

After the blade pull-out tests were performed, four samples were taken from both the top and bottom half of the consolidated soil to conduct undrained direct shear tests according to the ASTM-D6528 standard for undrained direct shear tests. (*ASTM International* 2018) First an impermeable film was placed on the bottom porous rock, so drainage is not allowed during the direct shear test. Subsequently, with the help of specimen rings, the soil sample is placed in the direct shear chambers and a second impermeable film is placed on top of the sample. Finally, the top porous rock and the pressure plate were placed on top of the film. The normal loads were applied and the direct shear test was commenced. Direct shear tests were performed at four normal pressures and a constant speed of 0.8 mm/min. Furthermore, two samples were taken to determine the water content for each consolidated soil specimen.

6.5.3 Procedure Summary

In short, the procedure for each test can be summarized using the following steps:

- Dry clay obtained from dredging sites is saturated for at least 3 days.
- The clay is consolidated up to the desired shear strength for a certain period: drainage is allowed. This is done in such a way that the consolidated clay is split in two halves, between which the blade can be placed for pull-out tests.
- Five blade pull-out tests are performed from 40 kPa up to 200 kPa, with incremental steps of 40 kPa. Between each tests, the blade is removed and the surface is rolled (flattened) to ensure an equally smooth surface between tests.
- After the pull-out tests, samples are taken to conduct undrained direct shear tests: so drainage is not allowed during these tests. Furthermore, two samples of the clay are used to determine the water content.

Chapter 7

Results and Discussion

In this Chapter, the results obtained from the blade pull-out experiments described in Chapter 6 are presented. First, the results for the internal and external shear strength (cohesion and adhesion) and the internal and external friction angles are discussed in Paragraph 7.1. In Paragraph 7.2 these results are analyzed and used to validate the models constructed in Chapter 5.

7.1 Internal and External Shear Strength and Friction Angles

As stated in Chapter 6, tests were performed on a total of 10 consolidated soil samples: five blade pull-out tests and four direct shear tests for each soil sample. The internal tangential resistance was recorded with a sampling frequency of 6 data points per sheared millimeter; the blade pull-out force was recorded with sampling frequency of 10 Hz. For each direct shear test the internal tangential resistance τ_c was plotted versus the shearing displacement. An example of these direct shear results for both soil 1 and soil 2 are shown in Figures 7.1(a) and 7.1(c). Also, the pull out force F was plotted versus the pull out displacement, shown in Figures 7.1(b) and 7.1(d).

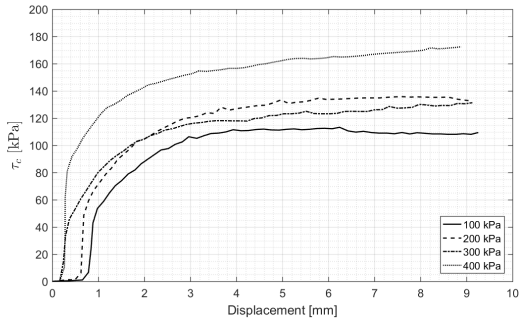

(a) Soil 1 - 15.9 % (w/w) - Direct shear results

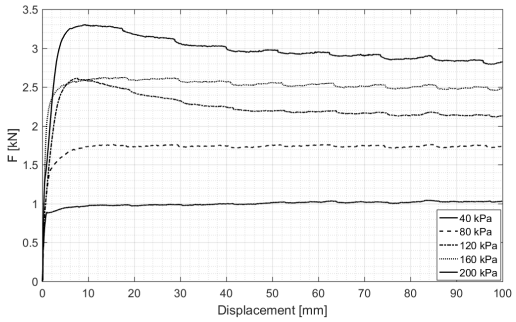

(b) Soil 1 - 15.9 % (w/w) - Blade pull-out test

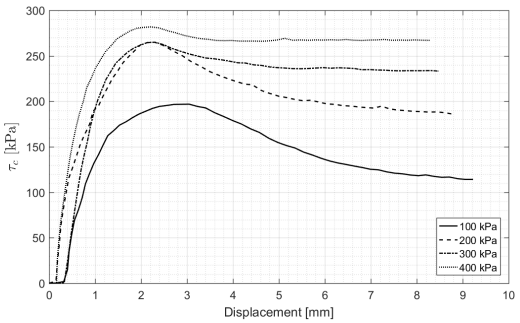

(c) Soil 2 - 12.0 % (w/w) - Direct shear results

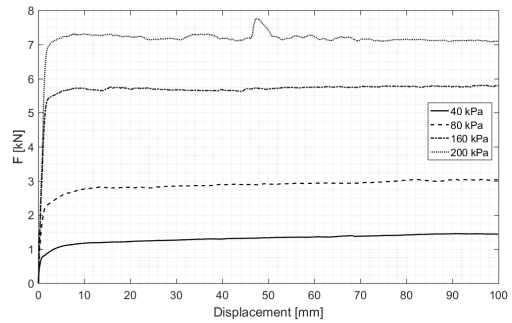

(d) Soil 2 - 12.0 % (w/w) - Blade pull-out test

FIGURE 7.1: Results obtained in the direct shear tests and blade pull-out tests

For both the undrained direct shear and the blade pull-out tests, the average steady-state value for the internal tangential resistance τ_c and blade pull-out force F were scattered in a Mohr-Coulomb diagram showing normal stress versus shear stress. Linear regressions were made according to the Mohr-Coulomb failure criterion (according to Figure 3.12) to obtain the internal and external shear strength at zero normal stress (cohesion and adhesion) and the internal and external friction angles. Statistical analysis showed significant linear regression between the normal stress σ and τ for both the direct shear results and the blade-pull out test results. Examples of this linear regression on the pull-out test data for both soil 1 and soil 2 are shown in Figures 7.2(a) and 7.2(b). Table 7.1 gives an overview of the experimental results for the undrained shear strength, internal friction angle, adhesion, external friction angle, adhesion factor and water content.

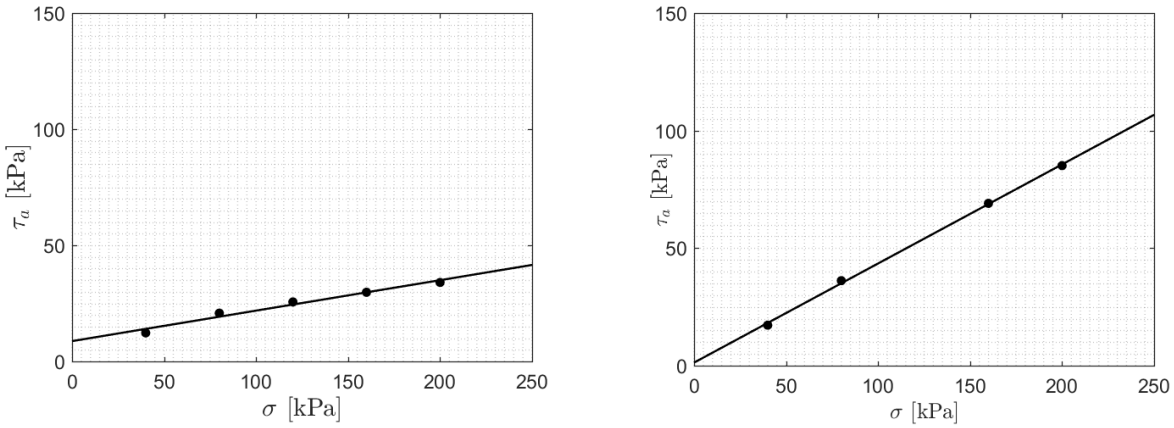

(a) Soil 1 - 15.9 % (w/w) - Normal stress versus shear stress with a linear fit according to the Mohr-Coulomb failure criterion

(b) Soil 2 - 12.0 % (w/w) - Normal stress versus shear stress with a linear fit according to the Mohr-Coulomb failure criterion

FIGURE 7.2: Example of normal stress versus shear stress with a linear fit according to the Mohr-Coulomb failure criterion for both soil 1 and soil 2

TABLE 7.1: Overview of the results obtained in the experimental study. Note: test data on sample 1-5 was lost due to data exchange issues after the tests.

Sample	Undrained Shear Strength [kPa]	Internal Friction Angle [degree]	Adhesion [kPa]	External Friction Angle [degree]	Adhesion Factor [-]	Water Content [w/w %]
1-1	31.05	4.8	7.26	2.31	***0.23***	0.226
1-2	57.00	4.96	4.63	8.05	***0.081***	0.174
1-3	71.63	11.02	7.94	10.29	***0.11***	0.181
1-4	90.98	7.92	8.76	7.47	***0.096***	0.159
1-5	-	-	-	-	**-**	-
2-1	30.12	4.14	7.01	10.74	***0.23***	0.229
2-2	32.72	4.19	7.50	8.74	***0.23***	0.206
2-3	81.54	14.07	9.13	16.90	***0.11***	0.181
2-4	188.44	14.29	0	22.86	***0***	0.120
2-5	295.0	14.67	0	27.45	***0***	0.105

The influence of the water content on the undrained shear strength and adhesion of the samples is examined with the obtained experimental data. Figure 7.3 shows the variation of both the undrained shear strength and adhesion with the water content. In Figure 7.3, the measured adhesion is depicted as dots (open dots for soil 1, filled dots for soil 2) and the cohesion (undrained shear strength) is depicted as diamonds (open diamonds for soil 1, filled diamonds for soil 2). Furthermore the Plastic Limit and Liquid Limit are depicted as the Plasticity Index for both of the tested soils; so the left borders are the Plastic Limits and the right borders the Liquid Limits. The black lines represent the best polynomial fit according to the least squares method.

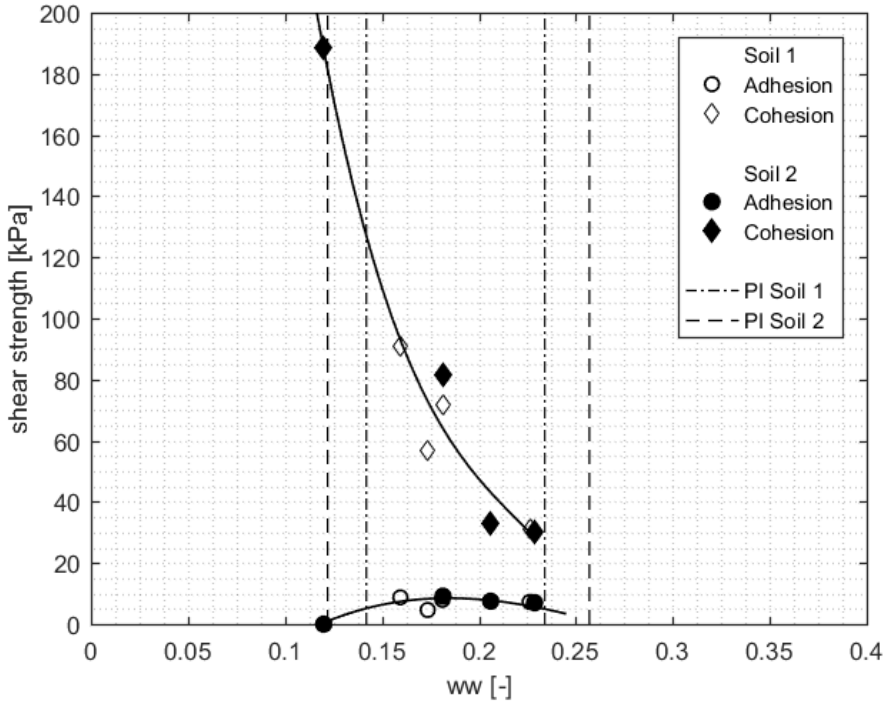

FIGURE 7.3: Variation of the cohesion and adhesion with the water content. Note: the test on the soil sample with the undrained shear strength c_u = 295 kPa is not depicted in this plot to be able to show the variation of the adhesion clearly

In Figure 7.3, the cohesion drops exponentially for increasing water content. Furthermore, just as in the research of Kooistra et al., adhesion varies with water content, with the peak adhesion closer to the Plastic Limit; this is more clearly depicted in Figure 7.5. Another interesting conclusion arising from Figure 7.3 is the fact that soil 1 and 2, despite of the slightly different mineralogy and composition, show the same behaviour over water contents.

Over the tested range of water contents, the measured adhesion is always smaller than the cohesion, which indicates that no sticking should occur. This matches the observations during and after the experiments, where very little to no clay was found on the metal blade after shearing.

In Figure 7.4, the variation of the internal friction angle ϕ and external friction angle δ with the undrained shear strength are depicted. Again, the open dots represent tests performed on samples of soil 1 and the filled dots on samples of soil 2. The dashed lines represent the best polynomial fit according to the least squares method.

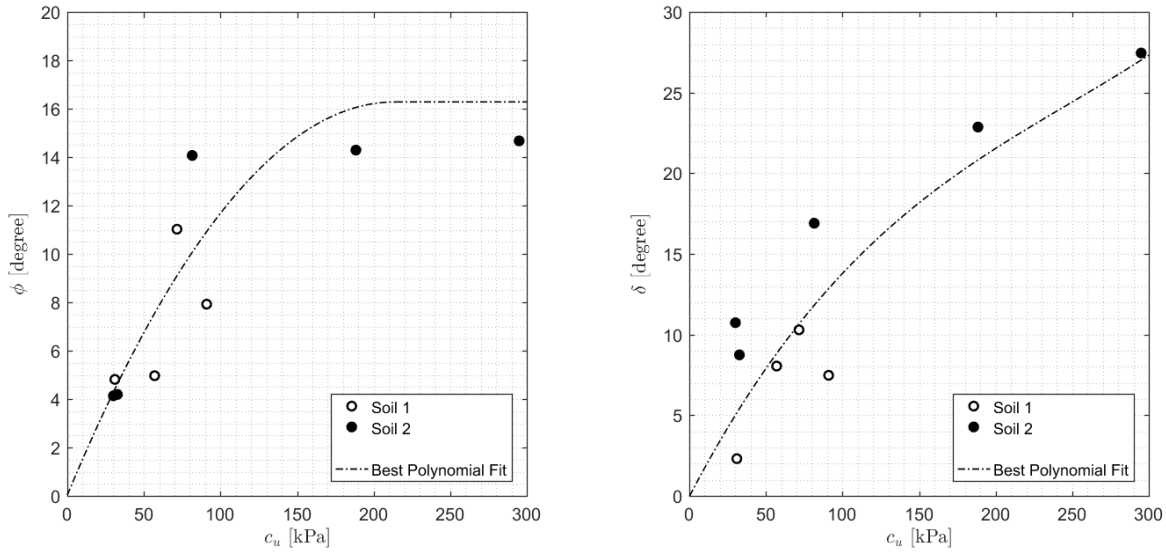

(a) Undrained shear strength versus the internal friction angle ϕ. The open dots represent test data obtained with tests on soil 1; the filled dots represent test data obtained with tests on soil 2. The dashed line represents the best polynomial fit.

(b) Undrained shear strength versus the external friction angle δ. The open dots represent test data obtained with tests on soil 1; the filled dots represent test data obtained with tests on soil 2. The dashed line represents the best polynomial fit.

FIGURE 7.4: Undrained shear strength versus the internal friction angle ϕ (a) and external friction angle δ (b)

In Figure 7.4(a), the internal friction angle ϕ shows a logarithmic growing trend: the internal friction angles increases less and less until a reaches a more or less constant value at high shear strengths. Figure 7.4(b) depicts the variation of the external friction angle δ with the undrained shear strength c_u. In the conducted tests, the external friction angle also shows a logarithmic growth, however in the tested range of undrained shear strengths, the external friction angle is still increasing.

In Figure 7.5, the variation of the adhesion with the water content is depicted in blue for all 9 soil samples. Furthermore, the variation of the external friction angle δ with the water content is depicted in orange. The dotted lines represent the best polynomial fit according to the least squares method. All data depicted in Figure 7.5 in measured in the range between the Plastic Limit and Liquid Limit for both soils; thus all samples where fully saturated. So, for both of the tested soils, the degree of consolidation (higher consolidation, lower pore volume and weight percent water) determines the adhesion of the soils, which was to be expected.

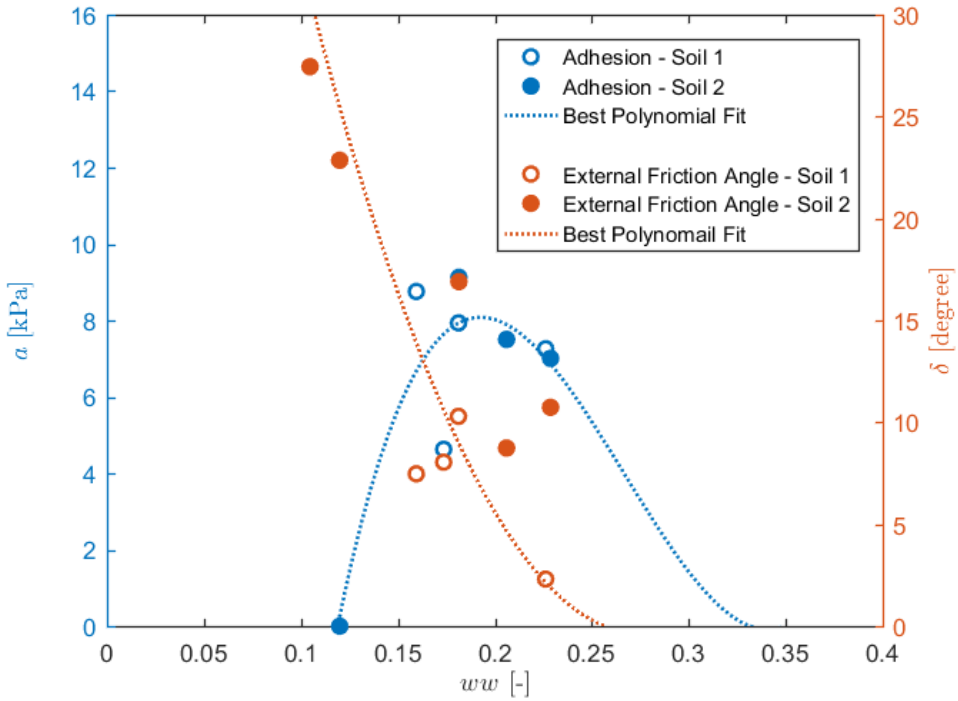

FIGURE 7.5: The variation of the adhesion (blue) and external friction angle (orange) with the water content in weight percent water

From Figure 7.5, it can be concluded that the adhesion of a cohesive soil has a maximum value at a certain water content. However, this does not mean that the overall tangential resistance on the dredging tools at a certain normal stress is at a maximum at this value; the tangential resistance keeps increasing for cohesive soils with a lower and lower water content. But it does indicate that a certain window exists where the effect on clay sticking to tools is at a maximum, possibly lowering production in these dredging operations.

7.2 Adhesion Factor

Again, tests were performed on a total of 10 consolidated soil samples (resulting in data for 9 samples). For each sample, five blade pull-out tests at a pull-out speed of 1 mm/s and four direct shear tests at 0.8 mm/s were performed. As mentioned in Paragraph 7.1, linear regression was used to obtain the undrained shear strength and adhesion of the tested samples. The results for the adhesion factor (again, defined as $\frac{a}{c}$) versus the undrained shear strength for both soils are depicted besides in Figure 7.6(a) and 7.6(b). Furthermore, the three constructed literature models are depicted besides the obtained experimental data.

In Figure 7.6(a) and 7.6(b), soil 1 is represented by the open black dots and soil 2 by the filled black dots. From Figure 7.6(a), it is clear that the adhesion factor for both soils follows the same exponential decaying trend towards zero. Furthermore, both the linear-exponential and constant-exponential model seem to provide a good representation of the experimental results. However, the adhesion factor between 20 and 30 [kPa] seems to be slightly overestimated by all models. Further research at low undrained shear strengths should show which model is the most accurate in the 1 - 20 kPa range.

7.3 Discussion on the Mechanism of Adhesion

Adhesion and cohesion have been interpreted in both the mechanical and non-mechanical ways. As stated previously, the mechanical perspective tends to treat adhesion and cohesion as a result of the pore water pressure change, e.g. as discussed by Mitchell and Soga, 2005, while the non-mechanical perspective tends to emphasize the impact of the micro-electrochemical reactions, especially when the clay contains organic compositions. It is clear from the results of the experiments that while both soils are comprised out of different minerals, they show the same trend as found from analyzing the literature data: the adhesion factor drops with a logarithmic trend towards zero for an increasing undrained shear strength. This indicates that in these tests, adhesion and cohesion can best be interpreted in a mechanical way.

In the undrained shear blade pull-out tests of the fully saturated soil, the external load is transmitted to pore water. This means that the pore pressure will increase and that the effective stress on the soil skeleton does not change. As a result the frictional forces stay equal: this applies for both internal and external friction. If the cohesive and adhesive shear strengths can be seen as constant for a certain soil type with a certain water content, then increasing the axial load can hardly affect the apparent shear stress. However, Figure 7.2 tells that the apparent shear stress increases proportionally to the normal stress. The reason could be the existence of two local effects:

- When the blade is being pulled out, a local dilatancy in the solid skeleton in the boundary layer of the soil sample and the blade will occur due to shearing. Due to the dilatancy the local pore volumes will change. Considering the fact that the soil samples hold very low porosities and permeabilities, the surrounding water can hardly flow into the expanded pores, as well as the pore water can hardly flow out of the shrunken pores. Overall, a water under-pressure will form up in the boundary layer. For the solid particles in this layer it means an extra pressure gradient force will be acting on them, thus locally the effective stress in vertical direction will increase.
- Due to the rough interface, the interface between the soil sample and the blade is not completely sealed. Thus, during the pull-out test a small amount of drainage can occur near the moving blade, so that the local effective stress will increase.

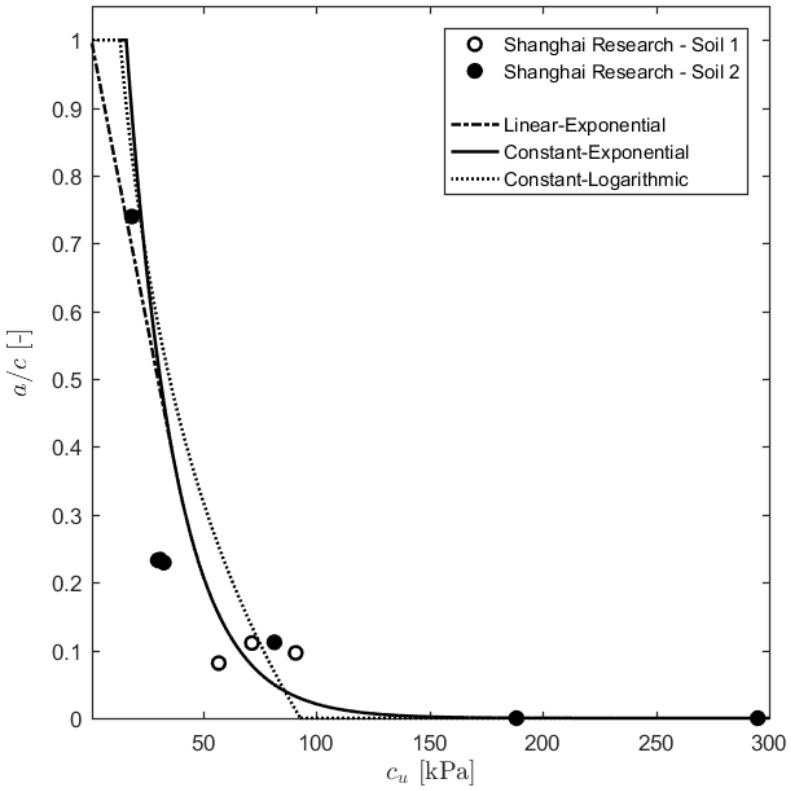

(a) Plot showing α-c_u data obtained in the Shanghai tests

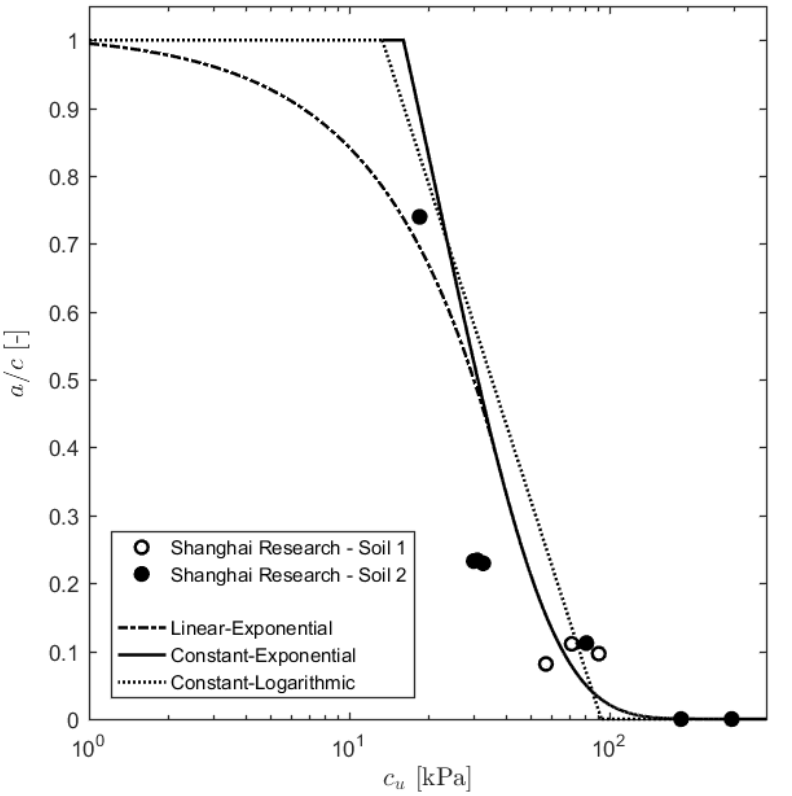

(b) Semi-logarithmic plot showing α-c_u data obtained in the Shanghai tests

FIGURE 7.6: Linear and semi-logarithmic plot of the adhesion factor versus the undrained shear strength as obtained in the Shanghai tests

Part IV

Implementation of the Cohesion-Adhesion Model: Numerical Modelling for Clay Cutting

Chapter 8

Numerical Modeling for Clay Cutting

With the help of numerical techniques, clay cutting process can be simulated in both atmospheric and saturated conditions. This chapter focuses on the numerical simulation of saturated clay cutting under atmospheric conditions. First, the physical concepts and assumptions used in creating a numerical model for clay cutting are discussed. Subsequently, two models used to validate the soil mechanical properties of the created numerical clay samples are presented. Examples of this validation are presented, which are subsequently used for validating the cutting model.

8.1 Discrete Element Modeling

The Discrete Element Package used in this research is the open source LIGGGHTS package (LAMMPS improved for general granular and granular heat transfer simulations). Macroscopic simulations are performed where all forces acting on a particle are summed for each particle. (*The Discrete Element Method* 2018) A more detailed description of particle force calculations is presented below.

Particle Forces

To compute the inter-particle friction/contact force, a Hertzian contact model is used. The Hertzian model is only valid for perfectly elastic solids as it represents the collision between to particles as a non-linear spring. In the Hertzian model, the contact force is proportional to the area of overlap of the two particles. When the distance r between two particles i and j is smaller than the inter-particle contact distance $R_i + R_j$, Equation 8.1 is valid for the inter-particle contact force. (*LIGGGHTS Documentation Version 3.X* 2018)

$$F_{hz} = \underbrace{\left(k_n \delta \mathbf{n}_{ij} - \gamma_n \mathbf{vn}_{ij}\right)}_{\text{Normal Force}} - \underbrace{\left(k_t \delta \mathbf{t}_{ij} - \gamma_t \mathbf{vt}_{ij}\right)}_{\text{Tangential Force}} \tag{8.1}$$

Where k_n is the elastic constant for normal contact ($\mathrm{N\,m^{-2}}$), $\delta \mathbf{n}_{ij}$ the normal overlap distance of two particles, γ_n the viscoelastic damping coefficient for normal contact, $\mathbf{vn}_{ij}$ the normal component of the relative velocity of the two particles, k_t the elastic constant for tangential contact ($\mathrm{N\,m^{-2}}$), $\delta \mathbf{t}_{ij}$ the tangential overlap distance of two particles, γ_t the viscoelastic damping coefficient for tangential contact and v_n and v_t the normal and $\mathbf{vt}_{ij}$ the tangential component of the relative velocity of the two particles. (*LIGGGHTS Documentation Version 3.X* 2018) The fact that the Hertzian contact model is based on the relation between the contact surface and geometric and material properties of the particles instead of the overlap distance used in the linear Hookean model makes the Hertzian model the preferred model in the DEM modeling of clay particles. (*LIGGGHTS Documentation Version 3.X* 2018) (Flores and Lankarani, 2016)

To model the internal shear strength or cohesion of the clay, the Simplified Johnson-Kendall-Roberts (SJKR) cohesion model is used. The SJKR cohesion model adds an additional normal force to particles in contact which resists separation. The force on a particle by cohesion is proportional to the overlap area and can be simply modeled as stated in Equation 8.2. (*LIGGGHTS Documentation Version 3.X* 2018)

$$F_c = K * O \tag{8.2}$$

Where K is the cohesion energy density and O the inter-particle overlap area [m^2].

When all forces on the particles are computed, NVE-integration (integration where the sum of kinetic and potential energy is conserved) is performed to compute the change in particle position, velocity and angular velocity during the specified time step, governed by Newton's laws of motion. Subsequently, the updated positions and velocities are used to compute the forces during the next time step. This process continues until the end time of the simulation is reached.

Micro-Macro Coupling

As stated in Equation 8.2, the cohesive force between two particles is the product of the cohesion energy density K and the overlap area A. At the microscopic scale, which is the scale of the input parameters, the cohesive force computed by the SJKR-model qualitatively and quantitatively agrees with the physical phenomena taking place between two grains. However, at the macroscopic level, the SJKR-model is only able to generate weak cohesive forces. This is because, especially for stiff particles, the overlap area between spherical particles is small. Therefore, at the macroscopic scale, the behavior is dominated by the larger gravitational and frictional forces. (Del Cid, 2015) One way to overcome this problem is by increasing the cohesion energy density K and increasing the coefficient of friction mu between to particles to increase the overall normal and tangential force between to particles. The second way to overcome this problem and generate a soil sample with the proper cohesive properties is to scale to experiment, because the normal and tangential forces between to particles are sensitive to the particle size. In this research it is preferred to scale the experiment, as increasing the cohesion energy density K and coefficient of friction μ can easily lead to numerically unstable situations.

8.2 Implementing Cohesive and Adhesive Shear Strength

As mentioned previously, the input parameters, which are implemented on a microscopic scale, do no lead directly to the desired macroscopic behaviour of the numeric clay sample. Therefore, the particles are scaled in such a way that they represent the desired cohesive macroscopic behaviour.

To test the cohesive shear properties of the numerical samples, ring shear tests are performed according to the ASTM D-6773 standard. (*ASTM International* 2018) The geometry used in the tests are modelled according to the Schulze Ring Shear Test Device. The walls are modelled as steel (E = 180 GPa) with a static friction coefficient of $\mu_s = 0.35$. The corrugated surfaces of the Schulze Ring Shear device, which are needed to prevent the soil from sliding on the surface of the top and bottom ring, are simplified in the performed tests. They are modelled as a total of 16 fins, 8 on the top ring and 8 on the bottom ring. A depiction of the ring shear geometry used in the tests is presented in Figure 8.1.

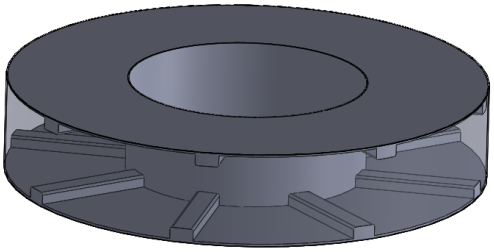

FIGURE 8.1: The Schulze ring shear test geometry used to validate the cohesive properties of the numerical clay sample.

Before testing, the ring shear geometry is filled with cohesive particles which are allowed to settle. A preset normal force is applied to the top ring before the shearing starts. This normal stress is held into place using by a proportional controller during the shearing. Subsequently, shearing is commenced by rotating the bottom ring at a constant speed of $\omega = 0.5\ rad/s$ until a constant torque T is reached. The shear stress can be calculated according to Equation 8.3.

$$\tau = \frac{T}{r_{mean} A} \tag{8.3}$$

Where τ is the shear stress $[kPa]$, T the torque $[Nm]$, r_{mean} the average radius $[m]$ and A the contact surface between the rings and the soil $[m^2]$. A depiction of a shear test is presented in Figure 8.2; Table 8.1 presents the input parameters. The results for a numerical shear test at various normal stresses are depicted in Figure 8.3.

TABLE 8.1: The Input Parameters for The Numerical Ring Shear Test

Particle Radius [m]		**Ring Shear Tester Radius [m]**		ω **[rad/s]**
minimum	maximum	inner radius	outer radius	
0.0015	0.022	0.5	1	0.5

In Figure 8.3, after applying the normal pressure, the shear force goes to a steady state value when shearing is commenced. Because it takes longer to build up the higher normal stresses, reaching the steady state takes longer for increasing applied normal stress. With the steady state results of the last second of shearing, the Mohr-Coulomb failure criterion is used to obtain the numerical internal shear strength at 0 normal stress; this is depicted in Figure 8.4.

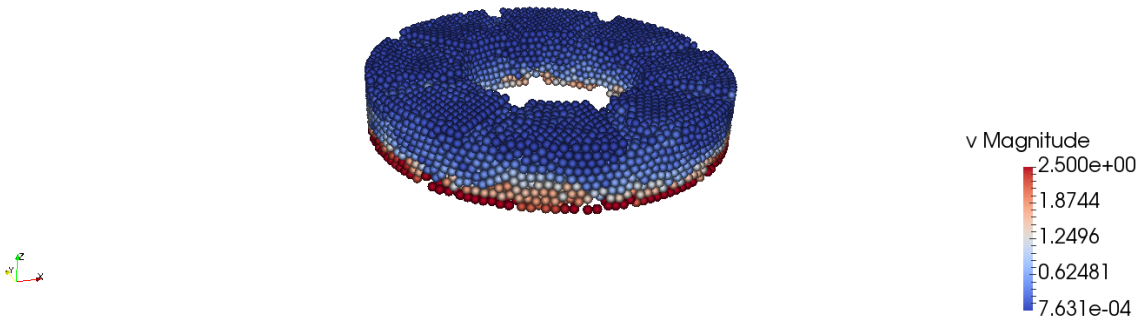

FIGURE 8.2: Numerical Shear Test, where the colors of the particles represent the particle velocity. Blue represents the low velocities, whereas red represent the highest velocities

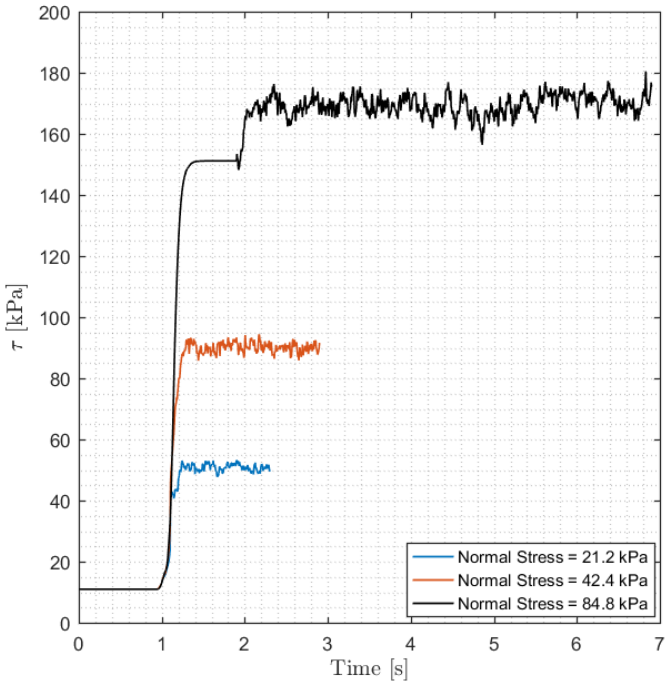

FIGURE 8.3: Results from the Numerical Shearing Test for Three Normal Stresses.

In Figure 8.4 the steady-state shear results from Figure 8.3 are plotted versus the applied normal stress. Furthermore, the Mohr-Coulomb failure criterion is plotted. From Figure 8.4 it can be concluded that these input parameters give an macroscopic cohesion of approximately 23 kPa, which is needed in the validation of the cutting model in Paragraph 8.3

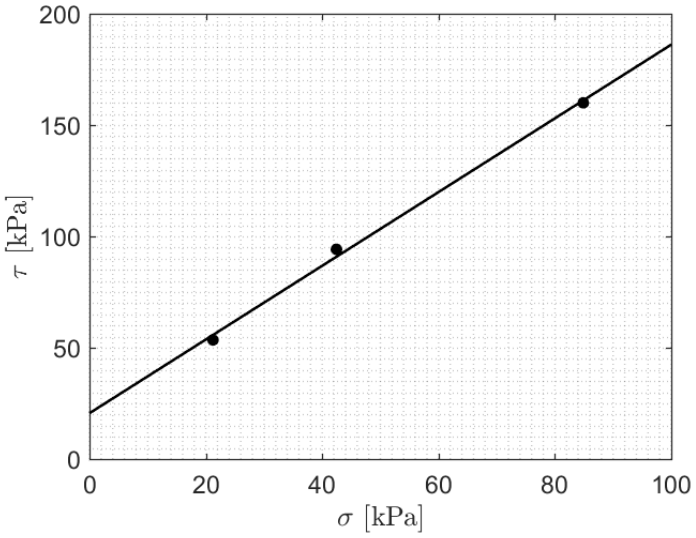

FIGURE 8.4: Results from the Numerical Shearing Test With the Mohr-Coulomb Failure Criterion.

Besides the internal shear strength, the external shear strength or the adhesion of the numerical sample needs to be validated as well. Using the developed model validated by the real life experiments depicted in Figure 7.6(b), the adhesion energy density is set at $0.75 \cdot K$. The horizontal blade pull-out tests which are performed experimentally in real life, are replicated numerically. A depiction of a numerical blade pull-out test is depicted in Figure 8.5; Table 8.2 presents the input parameters. The full code for the numerical blade pull-out test is given in Appendix B.1.

TABLE 8.2: The Input Parameters for the Numerical Blade Pull-Out Test

Particle Radius [m]		**Blade Dimensions [m]**		$V_{pullout}$ **[m/s]**
minimum	maximum	width	length	
0.0015	0.022	0.5	5	5

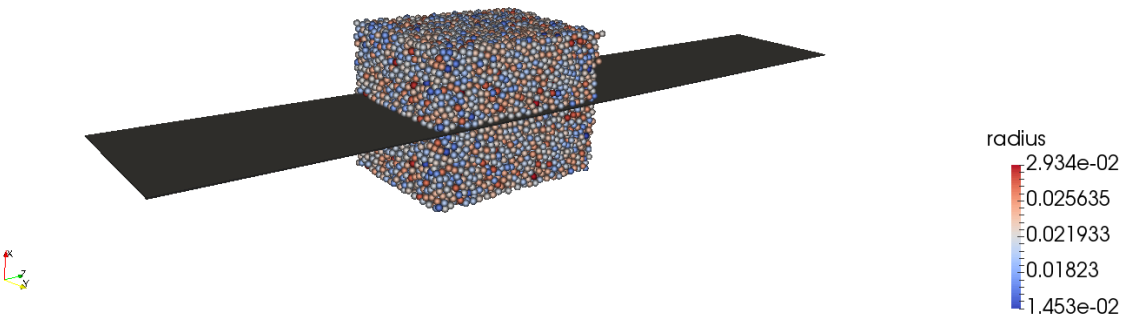

FIGURE 8.5: Numerical Blade Pull-out Test, where the colors represent the radii of the particles. Blue represents the lower particle radii, whereas red represent the highest radii.

The blade material is modelled as steel with equal properties to the materials of the Schulze Ring Shear Test Device. In this simulation, a negligible normal pressure is applied to both sides and maintained with a proportional controller. Blade pull-out tests are commenced at a constant velocity of 5 m/s, until the blade is pulled through the sample. Results for this numerical tests are presented in Figure 8.6. The full code is given in Appendix B.2.

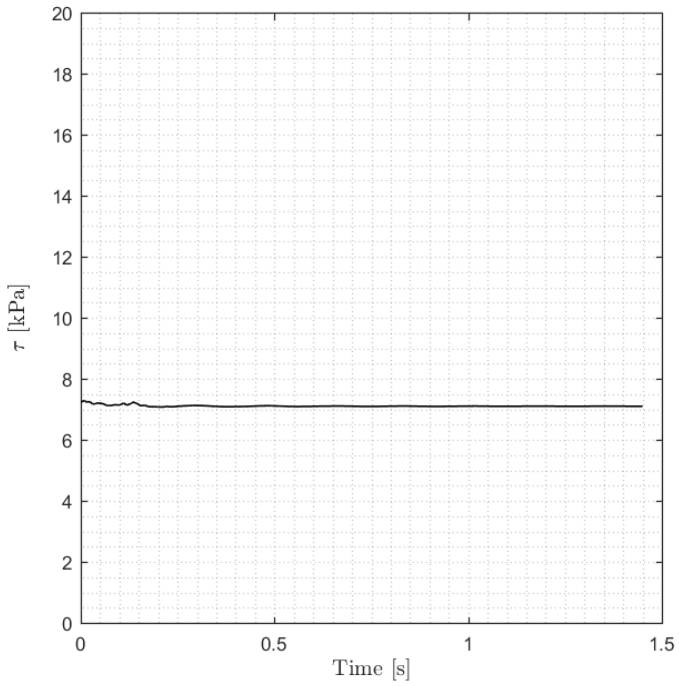

FIGURE 8.6: Results from the Numerical Blade Pull-out Test.

In Figure 8.6, it can be seen that during the pull-out of the blade, the tangential resistance, so the adhesion or external shear strength of the numerical clay sample, is approximately 7.1 [kPa]. This external shear strength is smaller than the desired 75 % of the numerical internal shear strength. This is caused by the fact that the overlap distance between the spherical particles and the flat metal surface is smaller than the overlap distance between two spherical particles on which this value is based, because the metal blade has a much higher stiffness than the clay particles. This results in a smaller overlap area used to compute the numerical adhesive strength.

8.3 Validation of the Cutting Model

Hatamura and Chijiiwa conducted cutting tests in plastic loam with various blade angles, blade depths and blade speeds to investigate the effect of the cutting angle, the depth of cut and the cutting speed. To validate the numerical DEM-model, the cutting experiments with blade angles of 30°, 45° and 60° at depth of cut of $0.1m$ and blade speed of $0.05m/s$ are replicated.

In the cutting of plastic loam a clear shear plane such as in sand cutting does not exist, because the shearing zone in loam is much thicker. Therefore, the plane obtained by connecting the points where the deformations are the most remarkable is called the shear plane (Hatamura and Chijiiwa, 1976b). Figures 8.7, 8.8 and 8.9 depict the cutting patterns observed in the DEM-simulation. The highlighted particles represented the particles that are being deformed; the orange lines represent the shear plane observed by Hatamura and Chijiiwa.

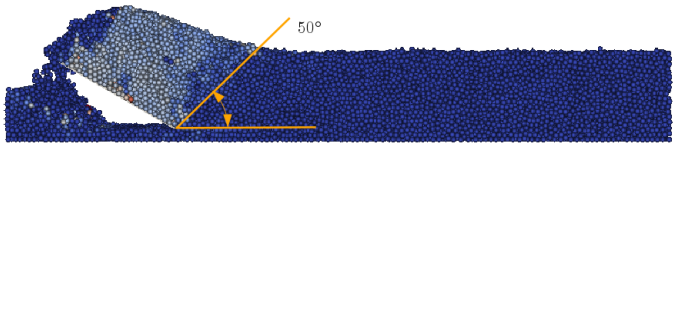

FIGURE 8.7: Cutting pattern observed in the DEM-simulation for a blade angle of 30°, a blade speed of $0.05m/s$ and a cutting depth of $0.06m$. The orange line depicts the direction of the shear plane observed by Hatamura and Chijiiwa (Hatamura and Chijiiwa, 1976a)

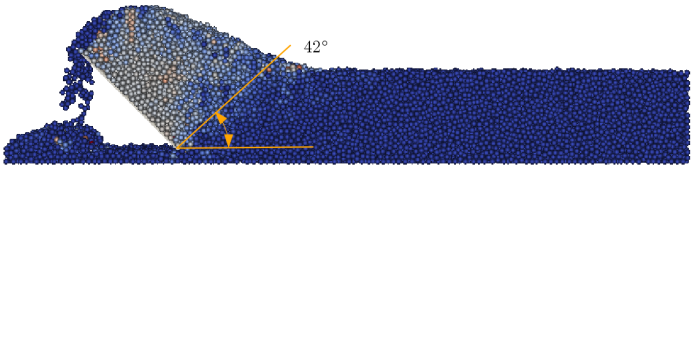

FIGURE 8.8: Cutting pattern observed in the DEM-simulation for a blade angle of 45°, a blade speed of $0.05m/s$ and a cutting depth of $0.06m$. The orange line depicts the direction of the shear plane observed by Hatamura and Chijiiwa (Hatamura and Chijiiwa, 1976a)

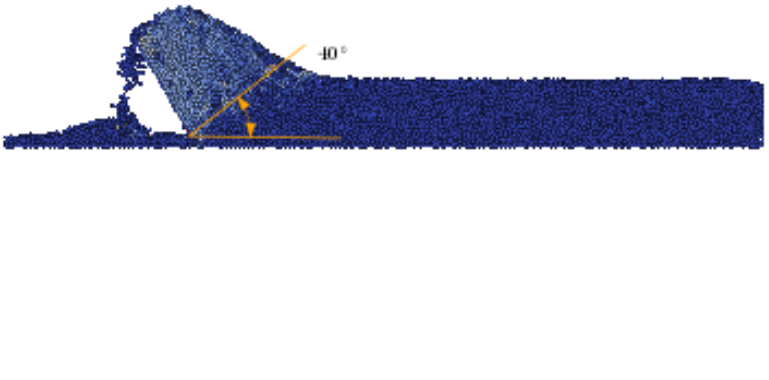

FIGURE 8.9: Cutting pattern observed in the DEM-simulation for a blade angle of 60°, a blade speed of $0.05m/s$ and a cutting depth of $0.06m$. The orange line depicts the direction of the shear plane observed by Hatamura and Chijiiwa (Hatamura and Chijiiwa, 1976a)

Just like the shear planes observed by Hatamura and Chijiiwa, the shear planes in the DEM-simulation stay in a constant position relative to the cutting blade irrespective of its proceedings.

From Figures 8.7, 8.8 and 8.9, it can be concluded that the shear plane found in the 60° DEM-simulations matches the experimental results of Hatamura and Chijiiwa. For 30° and 45° the simulated shear plane is approximated by the experimental value, but much more spread is observed. Hatamura and Chijiiwa found that in the case of cutting clay with 30° and 45° cutting blades, the clay is cut according to the tear type mechanism, therefore the shear plane at these angles was not clearly observable. While the 60° blade cuts the clay according to the flow type and a clear shear plane could be observed.

To be able to compare Hatamura and Chijiiwa's results with the numerically obtained results, a scaling relation based on Miedema's equations for the horizontal and vertical cutting force in the two-dimensional cutting of clay, given in Equation 4.5 and 4.6, is established. It should be noted that this scaling relation is an approximation: in this scaling relation, it is assumed that the cutting coefficients λ in Equation 4.5 and 4.6 stay constant.(Miedema, 2015) The scaling relation is given in Equation 8.4.

$$\frac{\sigma_{HC}}{\sigma_{DEM}} = \frac{h_{i,HC} \cdot h_{b,DEM}}{h_{i,DEM} \cdot h_{b,HC}} \tag{8.4}$$

Where σ_{HC} is the normal blade stress according to Hatamura and Chijiiwa's experiments and σ_{DEM} the numerically obtained normal blade stress. An overview of Hatamura and Chijiiwa's results for the total cutting force on the blade is given in Table 8.3. The results for the total cutting force on the blade obtained from the DEM-simulations are depicted in Figure 8.10.

TABLE 8.3: An overview of the results for the total blade force for blade angles of 30°, 45° and 60° at a cutting depth of $0.1m$ and blade speed of $0.05m/s$ as obtained by Hatamura and Chijiiwa (Hatamura and Chijiiwa, 1976b) and the results for the blade stress obtained as obtained by DEM-simulations.

	Hatamura and Chijiiwa			**Clay cutting simulation**			
	30	**45**	**60**	**30**	**45**	**60**	
total blade force	105	120	190				$[kg]$
	1030.1	1177.2	1863.9				$[N]$
direction of blade force	11	8	3				$[deg]$
angle with normal	49	37	27				$[deg]$
normal blade force	675.8	940.2	1660.7				$[N]$
normal blade stress	10.2	15.4	25.2				$[kPa]$
normal blade stress scaled	12.4	18.7	30.5	14.1	19.4	27.3	$[kPa]$

In Figure 8.10, the blue line depicts the blade stress for a blade angle of 30°, the orange line the blade stress for a blade angle of 45° and the black line the blade stress for a blade angle of 60°. The steady state blade stress is taken as the blade stress during the last second of cutting. The results for the steady state blade stress from the DEM-simulations is given in Table 8.3. The full code is given in Appendix B.3.

As discussed in the previous section, Hatamura and Chijiiwa found that in the case of cutting clay with 30° and 45° cutting blades, the clay is cut according to the tear type mechanism. For a blade angle of 60°, this cutting mechanism changes to the flow type. This change in cutting mechanisms explains why the steady state cutting force is reached faster for the 30° and 45° blades than for the blade with an angle of 60°. For the 30° and 45° blades the clay is teared in chunks

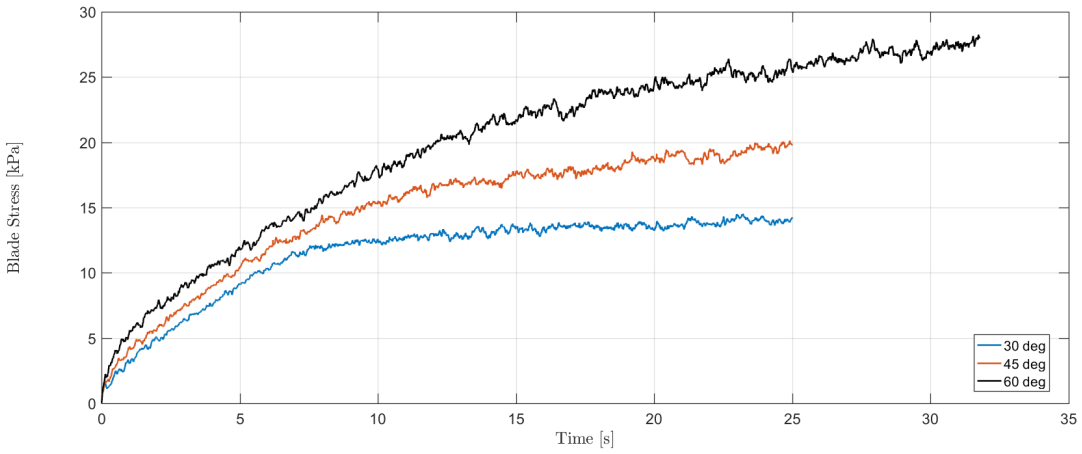

FIGURE 8.10: The measured blade stress versus cutting time as obtained by DEM-simulations. The blue line depicts the blade stress for a blade angle of 30°, the orange line for a blade angle of 45° and the black line for a blade angle of 60°.

before the particles flow over the blade. In the case of the 60° blade, the clay is first pushed and compressed until a certain layer thickness is reached. This layer thickness stays at a constant value as the particles flow over the blade. This pushing takes place over a longer distance, hence the time difference.

Because the experimental setup used by Hatamura and Chijiiwa is scaled in the DEM-simulation to achieve the proper macroscopic behavior of the clay sample, the total steady state cutting forces on the blade cannot be compared directly. To compare the DEM results with the experimental value the normal blade stress in the steady state is used and scaled according to Equation 8.4. The results for the scaled normal blade stress for the experiments by Hatamura and Chijiiwa and the obtained normal blade stress from the DEM-simulations are given in Table 8.3.

From Table 8.3 it can be concluded that the values for the blade stress found by Hatamura and Chijiiwa are slightly lower than the values obtained by the DEM-simulations, except for the blade angle of 60° where the numerical results is slightly smaller than the experimental value. However, it could be argued that the black line for an angle of 60° is still climbing and will end up slightly higher than the value found by Hatamura and Chijiiwa.

The error margin between the real life experiments and the DEM simulations are small at a maximum value of $\pm$ 10%; the numerical results for the normal blade stress are still in the same order of magnitude as found in the experiments by Hatamura and Chijiiwa. Overall it can be concluded that the developed DEM-model gives a good approximation of the total normal blade stress in plastic loam cutting. It is important to note that further simulations should be performed the validate the tangential blade stress, before the model can be used to simulate the cutting stress on dredging tools with more complex geometries.

Chapter 9

Conclusions and Recommendations

The main goal of this research is to characterize the relation between cohesion and adhesion in cohesive soils through experimental research. This new relation will be implemented in Miedema's "Delft Sand, Clay and Rock Cutting Model" to be able to analytically calculate and estimate cutting forces in cohesive soils. From the review of subsea ploughing and clamshell dredging, two common operations in dredging operations, **it becomes apparent that the adhesion factor, defined as the ratio between the adhesion and cohesion of a cohesive soil, plays an important roll in determining the overall cutting force in these dredging operations.**

A soil can be called 'cohesive' if the clay mineral fraction of the soil is above a certain threshold, therefore the this research uses clay as the main soil type. Clay possesses cohesive properties between the small, platy particles due to electrostatic bonds and possible cementing agents and adhesive properties with respect to other materials. This adhesion or external shear strength of the clay is partly due to solid-solid attraction, but predominantly due to adhesive action of the water in the soil.

From reviewing literature on the adhesion factor, it can be concluded that the adhesion factor models from literature can be split into two groups: the adhesion factor models based on total shear resistance used mainly in foundation engineering and the adhesion factor based on the true adhesion of the soil at zero normal stress. The foundation engineering adhesion models are mostly empirical; it is a coefficient which provides an indication for the total shear resistance of the foundation, so consisting of both adhesion and friction. The adhesion factor based on true adhesion consists solely out of the adhesive part and, therefore, it is generally lower, especially at higher undrained shear strengths. **In this project, the focus in on the true adhesion factor defined as a/c.**

With experimental data from various authors, three different models are constructed to describe the adhesion factor over an increasing undrained shear strength: a constant-logarithmic model, a linear-exponential model and a constant-exponential model.

To validate the constructed models a dedicated test setup was designed. Blade pull-out tests and direct shear tests were performed to evaluate the adhesion of two soils at a range of undrained shear strengths. **From the experimental results, it can be concluded that the exponential models provide the best description of the adhesion factor - undrained shear strength relation.** However, it should be noted that more tests at low undrained shear strengths (1 - 20 [kPa]) are required to give a conclusive assessment on the best model.

With the new adhesion factor models, numerical DEM-models for clay cutting where developed. The cohesive strength of the numerical clay sample was validated using the Schulze Ring Shear Test. Furthermore, the adhesive strength was validated using the same blade pull-out concept as in the real life experiments.

Finally, the developed cutting model was validated using the experiments carried out by Hatamura and Chijiiwa. **It can be concluded that the developed model gives a good description of the normal cutting stresses in cohesive soils, but further validation should be performed before the model can be used on more complex geometries.**

Summary of Conclusions

To summarize, this thesis reached the following conclusions:

- The adhesion factor, defined as the ratio between the adhesion and cohesion of a cohesive soil, plays an important roll in determining the overall cutting force in dredging operations in cohesive soils.
- The existing adhesion factor models can be split into two groups: the adhesion factor models based on total shear resistance and the adhesion factor based on the true adhesion of the soil at zero normal stress.
- From the experimental results, it can be concluded that the constructed exponential models provide the best description of the adhesion factor - undrained shear strength relation.
- The developed numerical model gives a good description of the cutting force in cohesive soils and can be used to calculate cutting forces on more complex geometries.

9.1 Recommendations

In the experiments allot of data was gathered regarding the adhesion at higher undrained shear strengths ($> 30\ kPa$) to be able to make the distinction between adhesion and friction. The constructed models for the adhesion factor are verified with this data, but verification at lower undrained shear strengths still needs to be performed. It is recommended that the constructed dedicated Adhesion Test Setup is used to conduct blade pull-out tests in this lower range of undrained shear strengths to be able to verify the adhesion factor models in that range.

Furthermore, tests were conducted at a fixed speed of $1\ mm/s$. Because it is likely that the blade pull-out speed will influence the results, it is recommended to conduct the blade-pull out tests at higher speeds.

Finally, a numerical model capable of providing a a good estimate of normal stresses on cutting tools in cohesive soils was created. In future research, this model can be used to quantify stresses on dredging tools for more complex geometries when the tangential blade stresses are validated.

Bibliography

ASTM International (2018). Standard ASTM. D4318-17e1: Standard Test Methods for Liquid Limit, Plastic Limit, and Plasticity Index of Soils.

ASTM International (2018). Standard ASTM. D6528: Standard Test Method for Consolidated Undrained Direct Simple Shear Testing of Cohesive Soils.

ASTM International (2018). Standard ASTM. D6773-02: Standard shear test method for bulk solids using the Schulze ring shear tester.

Barnes, G.E. (1995). *Soil Mechanics: Principles and Practice*. MacMillan Press Ltd, London.

BERR (2008). *Review of Cabling Techniques and Environmental Effects Applicable to the Offshore Wind Farm Industry - Techical Report*. Tech. rep. Department for Business Enterprise & Regulatory Reform.

Cappelletto, A. et al. (1998). "Field Full Scale Tests on Longitudinal Pipeline-Soil Interaction". In: *International Pipeline Conference - ASME 1998* 2, pp. 771–778.

Chen, X., J.W. van den Broecke, et al. (2019). "Analysis of the Cohesion-Adhesion Relation of Cohesive Soil". WODCON XXII.

Chen, X., S.A. Miedema, and C. van Rhee (2015). "Numerical Modeling of Excavation Process in Dredging Engineering". In: *Procedia Engineering* 102, pp. 804–814.

Chen, Y. et al. (2011). "Evaluation of Side Resistance Capacity for Drilled Shafts". In: *Journal of Marine Science and Technology*.

Del Cid, L.I. (2015). "A Discrete Element Methodology for the Analysis of Cohesive Granular Bulk Solid Materials". PhD thesis. Colorado School of Mines.

Contact Force Models for Multibody Dynamics (2016). Springer International Publishing.

Fountaine, E.R. (1953). *Investigations Into The Mechanism of Soil Adhesion*. Tech. rep. National Institute of Agricultural Engineering.

Hatamura, Y and K Chijiiwa (1975). "Analysis of the Mechanism of Soil Cutting: 1st report. Cutting Patterns of Soils". In: *Bulletin of the JSME* 18, pp. 619–626.

— (1976a). "Analysis of the Mechanism of Soil Cutting: 2nd report. Deformation and Internal Stress of Soil in Cutting". In: *Bulletin of the JSME* 19, pp. 555–563.

— (1976b). "Analysis of the Mechanism of Soil Cutting: 3rd report. Distribution of Stresses on Cutting Blade and Cutting Force". In: *Bulletin of the JSME* 19, pp. 1376–1384.

— (1977a). "Analysis of the Mechanism of Soil Cutting: 4th report. Properties of Soils Related to Cutting". In: *Bulletin of the JSME* 20, pp. 130–137.

Hatamura, Y and K Chijiiwa (1977b). "Analysis of the Mechanism of Soil Cutting: 5th report. Cutting Theories of Soils". In: *Bulletin of the JSME* 20, pp. 388–395.

IHC (2009). *Leaflet Pipeline Ploughs*.

Khan, M. Azam, R. Qaisrani, and L. Jian-Qiao (2010). "The Techniques of Reducing Adhesion and Scouring Soil by Bionic". In: *Advances in Natural Science* 3.2, p. 10.

Kooistra, A. et al. (1998). *Appraisal of Stickiness of Natural Clay from Laboratory Tets*. Tech. rep. Delft University of Technology.

LIGGGHTS Documentation Version 3.X (2018). Retrieved from: `https://www.cfdem.com/media/DEM/docu/Manual.html`.

Littleton, I. (1976). "An Experimental Study of The Adhesion Between Clay and Steel". In: *Journal of Terramechanics* 13.3, pp. 141–152.

Miedema, S.A. (1992). "New Developments of Cutting Theories with respect to Dredging, the Cutting of Clay". In: *Proc. WODCON XIII*.

— (2015). *The Delft Sand, Clay & Rock Cutting Model*. 3rd Edition. IOS Press.

Miedema, S.A. and W.J. Vlasblom (2006). "The Closing Process of Clamshell Dredges in Water-Saturated Sand". In: *CEDA African Section: Dredging Days 2006 - Protection of the coastline, dredging sustainable development*.

Mitchell, J.K. and K. Soga (2005). *Fundamentals of Soil Behavior*. John Wiley & Sons, Hoboken, New Jersey.

Stafford, J.V. and D.W. Tanner (1976). *The Frictional Characteristics of Steel Sliding On Soil*. Tech. rep. National Institute of Agricultural Engineering.

The Discrete Element Method (2018). Retrieved from: `https://en.wikipedia.org/wiki/Discrete_element_method`.

Tong, J. et al. (1994). "Characteristics of Adhesion Between Soil and Solid Surfaces". In: *Journal of Terramechanics* 31.2, pp. 93–105.

USDA (2018). Particle Soil classification by USDA. Retrieved from: `https://www.nrcs.usda.gov/wps/portal/nrcs/detail/soils/survey/office/ssr10/tr/?cid=nrcs144p2_074845`.

Van Der Wielen, V. (2014). "Physical Modeling of Soft Clay Cutting for Plain Strain Conditions". MA thesis. Delft University of Technology.

Van Gurp, A.P. (2014). "Development of a Plough Pulling Force Model for Submarine Narrow Shaped Ploughs". MA thesis. Delft University of Technology.

Zhang, J.G. (1985). "Studies on the adhesion and friction of soil to solid materials". PhD thesis. Jiangsu Technical College.

Zimnik, A. R. et al. (2014). *The Adherence of Clay to Steel Surfaces*.

List of Symbols

$\boldsymbol{\alpha}$	adhesion factor	-
α	arbitrary angle	$^\circ$
α_a	cutting angle	$^\circ$
β	angle of the shear plane and the cutting velocity	$^\circ$
γ_n	viscoelastic damping coefficient for normal contact	$\mathrm{N\,m^{-2}\,s^{-2}}$
γ_s	unit weight of a soil	$\mathrm{kg\,m^{-3}}$
γ_t	viscoelastic damping coefficient for tangential contact	$\mathrm{N\,m^{-2}\,s^{-2}}$
δ	external friction angle	$^\circ$
$\delta\mathbf{n}_{ij}$	normal overlap distance of two particles	$\mathrm{m^2}$
$\delta\mathbf{t}_{ij}$	tangential overlap distance of two particles	$\mathrm{m^2}$
λ	strengthening factor	-
μ_s	static friction coefficient	-
ϕ	internal friction angle	$^\circ$
σ	normal stress	Pa
σ_h	horizontal stress	Pa
σ_e	normal stress on the bucket edge	Pa
σ_v	vertical stress	Pa
τ	shear stress	Pa
τ_a	adhesive shear strength, same as a	Pa
τ_c	cohesive shear strength, same as c	Pa
τ_e	shear stress on the bucket edge	Pa
A	shear force on blade	N
A_e	bucket edge area	$\mathrm{m^3}$
a	adhesion	Pa
B	foundation width	m
b	plough width	m
C	shear force on shear surface	N
c	cohesion	Pa
c_u	undrained shear strength	Pa
d	ploughing depth	m
F	force	N
F_c	numerical cohesion force	N
F_e	pressure force on bucket edges	N
F_h	horizontal cutting force	N
F_{hz}	Herztian inter-particle contact force	N
F_{pull}	subsea plough pulling force	N
F_v	vertical cutting force	N
h_b	blade height	m
h_i	cutting depth	m
K	cohesion energy density	$\mathrm{J\,m^{-3}}$
k_n	elastic constant for normal contact	$\mathrm{N\,m^{-2}}$

k_t	elastic constant for tangential contact	$\mathrm{N\,m^{-2}}$
L	foundation length	m
l_a	adhesion length, dependent on plough geometry	m
m_s	mass of solids in a soil	kg
m_w	mass of water in a soil	kg
N_1	normal force on shear surface	N
N_2	normal force on blade	N
N_γ	Terzaghi's bearing capacity factor depending on unit soil weight	-
N_c	Terzaghi's bearing capacity factor depending on the internal friction angle	-
N_q	Terzaghi's bearing capacity factor depending on the cutting depth	-
N_{cp}	dimensionless coefficient depending on plough geometry	-
O	inter-particle overlap area	$\mathrm{m^2}$
Q_s	side resistance capacity of a pile foundation	Pa
S	degree of saturation	-
S_c	effective soil-body contact area	$\mathrm{m^2}$
s_u	undrained shear strength	Pa
T	torque	Nm
t	thickness	m
$t_{1...10}$	consolidation time	s
$R_{i,j}$	particle radius	m
r	distance between to particles	m
V_a	volume of air in a soil	$\mathrm{m^3}$
V_p	soil pore volume	$\mathrm{m^3}$
V_w	volume of water in a soil	$\mathrm{m^3}$
$\mathbf{vn}_{ij}$	normal component of the relative velocity of two particles	$\mathrm{m^2\,s^{-2}}$
$\mathbf{vt}_{ij}$	tangential component of the relative velocity of two particles	$\mathrm{m^2\,s^{-2}}$
w	blade width	m
ww	moisture content or weight percent water	-

List of Figures

2.1 The PL3 V-shaped Pipe Burial Plough Designed by Royal IHC. Retrieved from IHC, 2009 . . . 6
2.2 Schematic Representation of a Self-propelled Clamshell Dredger. Retrieved from Miedema and Vlasblom, 2006 . . . 7
2.3 Schematic Representation of a Cable Clamshell Bucket Hoisting System . Retrieved from Miedema and Vlasblom, 2006 . . . 8

3.1 Soil naming according to the United States Department of Agriculture. Retrieved from `https://www.nrcs.usda.gov`. . . . 12
3.2 The Atterberg Limits. Retrieved from Barnes, 1995 . . . 13
3.3 Particle size ranges for engineering classifications. Retrieved from Mitchell and Soga (2005). . . . 14
3.4 Overview of a single silicon tetrahedron and a silica sheet. Retrieved from Mitchell and Soga (2005). . . . 15
3.5 Overview of a single octahedral unit and an octahedral sheet structure. Retrieved from Mitchell and Soga (2005). . . . 15
3.6 An overview of the most common types of clay minerals. Retrieved from (Barnes, 1995) . . . 16
3.7 The stresses acting on an infinitesimal piece of soil. Retrieved from Miedema, 2015. . 17
3.8 The Mohr circle with the Mohr-Coulomb failure criterion . . . 18
3.9 Direct shear test (soil-soil) with the Mohr-Coulomb failure criterion . . . 18
3.10 Adhesion of a relatively dry and coarse soil (left) and a relatively wet ideal fine soil (right). Retrieved from: (Fountaine, 1953) . . . 19
3.11 The adhesive tensile strength (normal pull) and the adhesive shear strength (tangential pull). Retrieved from (Zimnik et al., 2014) . . . 20
3.12 Direct shear test (soil-foreign body) with the Mohr-Coulomb failure criterion . . . 21

4.1 The different types of cutting mechanisms encountered in excavation processes. Retrieved from Miedema, 2015. . . . 24
4.2 Forces on the layer cut and forces on the blade in clay cutting. Retrieved from Miedema, 2015. . . . 25

5.1 An overview of the most frequently used α-c_u relations (1 ton/m^2 is approximately 10 kPa). Retrieved from `http://www.thaicontractors.com` . . . 30
5.2 Linear and semi-logarithmic plot of the adhesion factor versus the undrained shear strength as obtained from literature. . . . 33
5.3 Linear and semi-logarithmic plot of the adhesion factor versus the undrained shear strength as obtained from literature. . . . 34

6.1 The Horizontal Adhesion Test Setup Concept. . . . 38
6.2 The Vertical Adhesion Test Setup Concept. . . . 39
6.3 The Vertical Adhesion Test Setup Concept. . . . 40
6.4 The final concept for the design of the Adhesion Test Setup. . . . 41

6.5 A schematic overview of the final experimental setup used for measuring soil-metal friction. . . . 42
6.6 A schematic overview of the direct shear boxes used. Retrieved from `http://www.soilmanagementindia.com/soil/shear-strength` . . . 43

7.1 Results obtained in the direct shear tests and blade pull-out tests . . . 47
7.2 Example of normal stress versus shear stress with a linear fit according to the Mohr-Coulomb failure criterion for both soil 1 and soil 2 . . . 48
7.3 Variation of the cohesion and adhesion with the water content. Note: the test on the soil sample with the undrained shear strength $c_u = 295\ kPa$ is not depicted in this plot to be able to show the variation of the adhesion clearly . . . 49
7.4 Undrained shear strength versus the internal friction angle ϕ (a) and external friction angle δ (b) . . . 50
7.5 The variation of the adhesion (blue) and external friction angle (orange) with the water content in weight percent water . . . 51
7.6 Linear and semi-logarithmic plot of the adhesion factor versus the undrained shear strength as obtained in the Shanghai tests . . . 53

8.1 The Schulze ring shear test geometry used to validate the cohesive properties of the numerical clay sample. . . . 59
8.2 Numerical Shear Test, where the colors of the particles represent the particle velocity. Blue represents the low velocities, whereas red represent the highest velocities . 60
8.3 Results from the Numerical Shearing Test for Three Normal Stresses. . . . 60
8.4 Results from the Numerical Shearing Test With the Mohr-Coulomb Failure Criterion. 61
8.5 Numerical Blade Pull-out Test, where the colors represent the radii of the particles. Blue represents the lower particle radii, whereas red represent the highest radii. . . . 61
8.6 Results from the Numerical Blade Pull-out Test. . . . 62
8.7 Cutting pattern observed in the DEM-simulation for a blade angle of 30°, a blade speed of $0.05m/s$ and a cutting depth of $0.06m$. The orange line depicts the direction of the shear plane observed by Hatamura and Chijiiwa (Hatamura and Chijiiwa, 1976a) . . . 63
8.8 Cutting pattern observed in the DEM-simulation for a blade angle of 45°, a blade speed of $0.05m/s$ and a cutting depth of $0.06m$. The orange line depicts the direction of the shear plane observed by Hatamura and Chijiiwa (Hatamura and Chijiiwa, 1976a) . . . 63
8.9 Cutting pattern observed in the DEM-simulation for a blade angle of 60°, a blade speed of $0.05m/s$ and a cutting depth of $0.06m$. The orange line depicts the direction of the shear plane observed by Hatamura and Chijiiwa (Hatamura and Chijiiwa, 1976a) . . . 63
8.10 The measured blade stress versus cutting time as obtained by DEM-simulations. The blue line depicts the blade stress for a blade angle of 30°, the orange line for a blade angle of 45° and the black line for a blade angle of 60°. . . . 65

A.1 Render of the Vertical Adhesion Test Setup . . . 77
A.2 Pictures of the Adhesion Test Setup: (a) before the pressure is applied and (B) during the pull-out test . . . 84
A.3 The direct shear apparatus used to measure the undrained shear strength . . . 85
A.4 Results from the cone drop tests to obtain the plastic limit and liquid limit . . . 86
A.5 Results from the cone drop tests to obtain the plastic limit and liquid limit . . . 87
A.6 X-ray diffraction result for soil 1 . . . 88
A.7 X-ray diffraction result for soil 2 . . . 89

List of Tables

2.1 General Properties of the PL3 Pipe Burial Plough by Royal IHC. (IHC, 2009) 6

3.1 Soil classification according to Soil particle size according to Miedema, 2015 11

5.1 An overview of the soils and there properties obtained in the literature review. . . . 31

6.1 Experimental Matrix 43
6.2 The main soil properties of the used soils 44

7.1 Overview of the results obtained in the experimental study. Note: test data on sample 1-5 was lost due to data exchange issues after the tests. 48

8.1 The Input Parameters for The Numerical Ring Shear Test 59
8.2 The Input Parameters for the Numerical Blade Pull-Out Test 61
8.3 An overview of the results for the total blade force for blade angles of 30°, 45° and 60° at a cutting depth of 0.1m and blade speed of 0.05m/s as obtained by Hatamura and Chijiiwa (Hatamura and Chijiiwa, 1976b) and the results for the blade stress obtained as obtained by DEM-simulations. 64

Appendix A

Appendix to Chapter 6: Experimental Study

A.1 Vertical Adhesion Test Setup Drawings

FIGURE A.1: Render of the Vertical Adhesion Test Setup

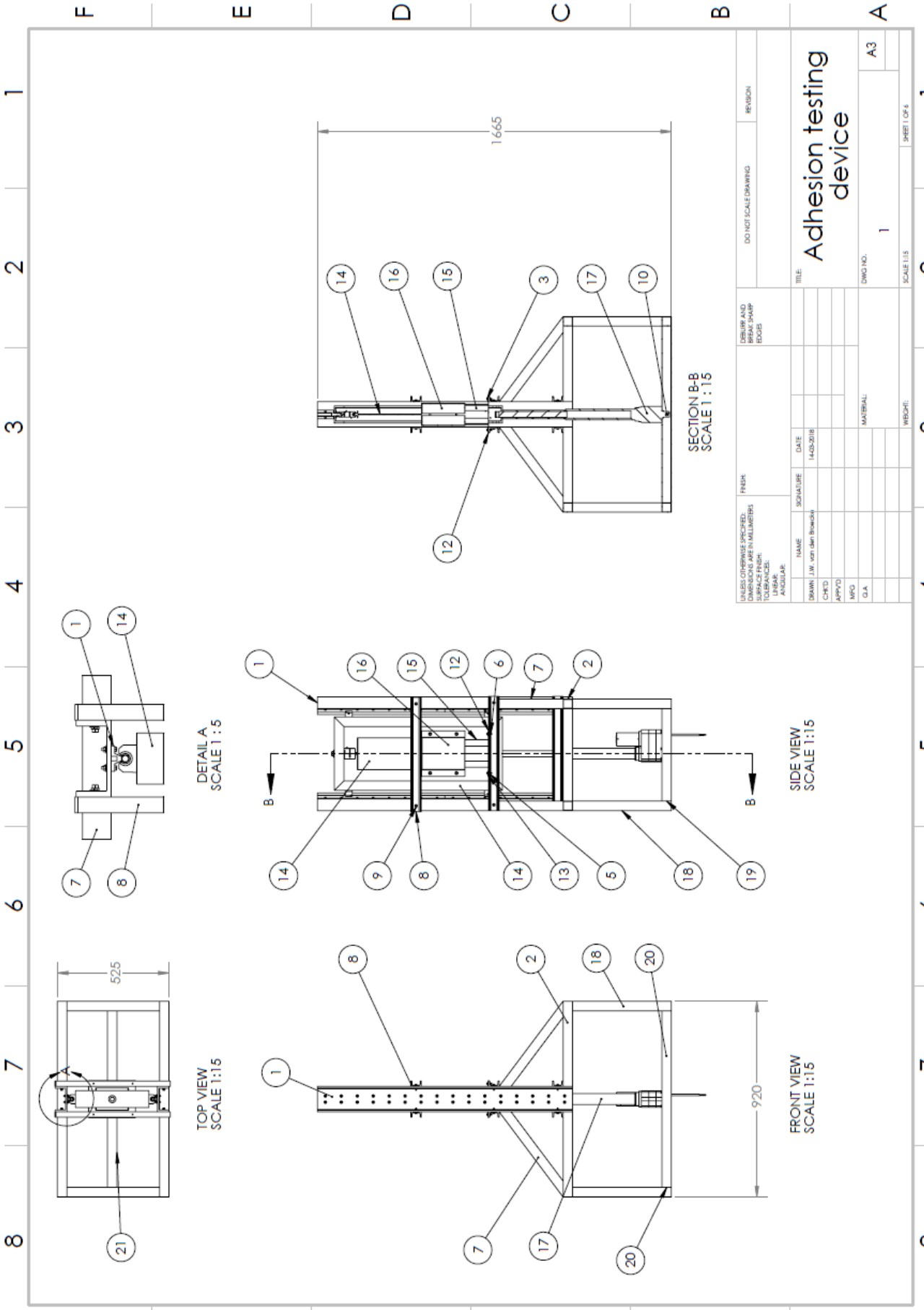
Adhesion testing device
A3
SECTION B-B
SCALE 1 : 15
DETAIL A
SCALE 1 : 5
SIDE VIEW
SCALE 1:15
TOP VIEW
SCALE 1:15
FRONT VIEW
SCALE 1:15
1665
525
920

ITEM NO.	PART NUMBER	DESCRIPTION	QTY.
1	Linear guide assembly		2
2	Support box profile base		4
3	B18.6.7M - M4 x 0.7 x 20 Plain HHMS --20C		4
4	B18.22M - Plain washer, 12 mm, regular		2
5	B18.22M - Plain washer, 4 mm, regular		28
6	B18.2.4.1M - Hex nut, Style 1, M4 x 0.7 --D-N		16
7	Support box profile angle		4
8	Connecting channel profile		6
9	B18.6.7M - M4 x 0.7 x 25 Plain HHMS --25C		12
10	B18.6.7M - M12 x 1.75 x 80 Plain HHMS --38C		1
11	B18.2.4.1M - Hex nut, Style 1, M12 x 1.75 --D-N		1
12	Sample holder support plate		1
13	B18.22M - Plain washer, 4 mm, wide		4
14	Frame assembly		1
15	Sample holder support L profile		4
16	Sample holder assembly		1
17	CAHB20-A3-E-300495-B-AD0ET-000-E linear electrical actuator		1
18	Base frame vertical leg box profile		4
19	Base frame short horizontal leg box profile		4
20	Base frame long horizontal leg box profile		2
21	Base frame long horizontal box profile with hole		1

UNLESS OTHERWISE SPECIFIED:
DIMENSIONS ARE IN MILLIMETERS
SURFACE FINISH:
TOLERANCES:
LINEAR:
ANGULAR:

FINISH:

DEBURR AND BREAK SHARP EDGES

DO NOT SCALE DRAWING | REVISION

	NAME	SIGNATURE	DATE
DRAWN	J.W. van den Broecke		14-05-2018
CHK'D			
APPV'D			
MFG			
Q.A			

MATERIAL:

WEIGHT:

TITLE:

Adhesion testing device

DWG NO. 2

A3

SCALE:1:20

SHEET 2 OF 6

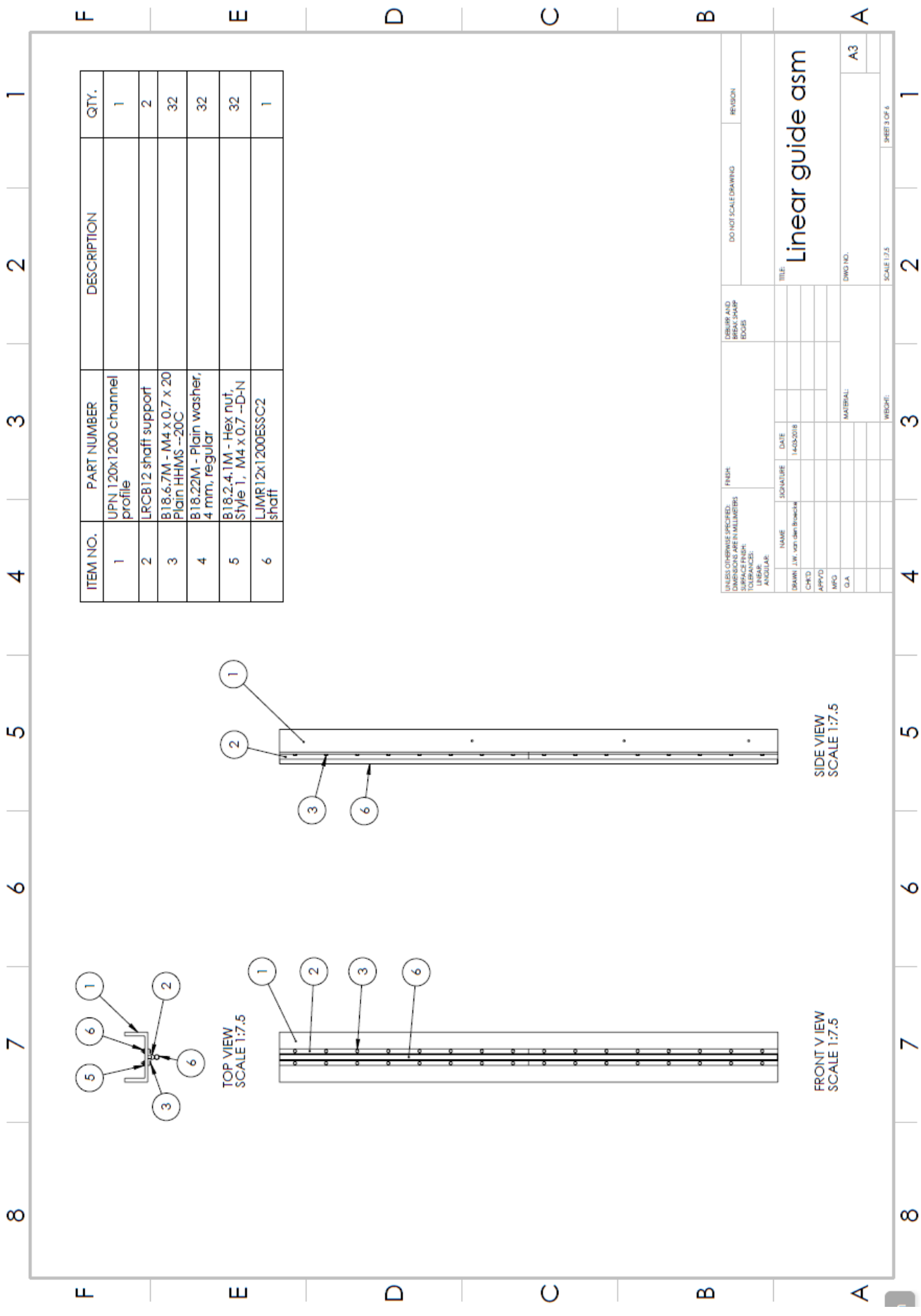
Linear guide asm
A3
SCALE 1:7.5
SHEET 3 OF 6
DO NOT SCALE DRAWING
REVISION
DEBURR AND BREAK SHARP EDGES
FINISH
DATE
SIGNATURE
NAME
DRAWN J.W. van den Broeke 14-03-2018
CHK'D
APP'D
MFG
Q.A
MATERIAL:
WEIGHT:
DWG NO.
TITLE:
UNLESS OTHERWISE SPECIFIED:
DIMENSIONS ARE IN MILLIMETERS
SURFACE FINISH:
TOLERANCES:
LINEAR:
ANGULAR:
ITEM NO. PART NUMBER DESCRIPTION QTY.
1 UPN 120x1200 channel profile 1
2 LRCB12 shaft support 2
3 B18.6.7M - M4 x 0.7 x 20 Plain HHMS --20C 32
4 B18.22M - Plain washer, 4 mm, regular 32
5 B18.2.4.1M - Hex nut, Style 1, M4 x 0.7 --D-N 32
6 LJMR12x1200ESSC2 shaft 1
TOP VIEW
SCALE 1:7.5
SIDE VIEW
SCALE 1:7.5
FRONT V IEW
SCALE 1:7.5

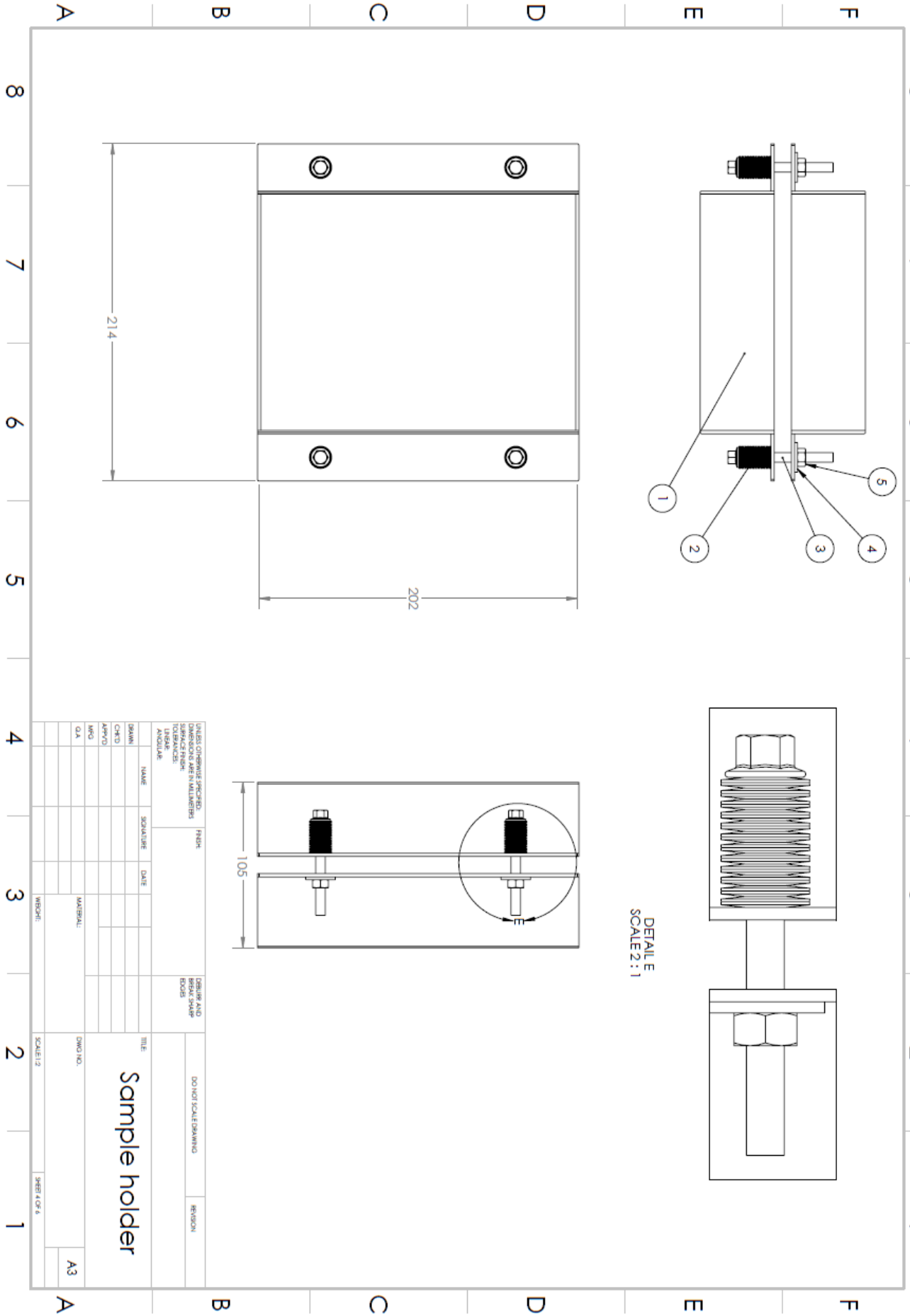
214
202
105
DETAIL E
SCALE 2 : 1
Sample holder
A3

ITEM NO.	PART NUMBER	DESCRIPTION	QTY.
1	2_sample_half_sample_container		2
2	2_sample_bellville_thin_parallel_washer_asm		4
3	B18.6.7M - M6 x 1.0 x 60 Plain HFMS --60C		4
4	B18.22M - Plain washer, 6 mm, regular		4
5	B18.2.4.1M - Hex nut, Style 1, M6 x 1 --D-N		4

UNLESS OTHERWISE SPECIFIED:
DIMENSIONS ARE IN MILLIMETERS
SURFACE FINISH:
TOLERANCES:
LINEAR:
ANGULAR:

FINISH:

DEBURR AND BREAK SHARP EDGES

DO NOT SCALE DRAWING

REVISION

	NAME	SIGNATURE	DATE
DRAWN			
CHK'D			
APPV'D			
MFG			
Q.A			

TITLE:
Adhesion testing device

MATERIAL:

DWG NO.
adhesion_testing_device_asm

A3

WEIGHT:

SCALE:1:10

SHEET 5 OF 6

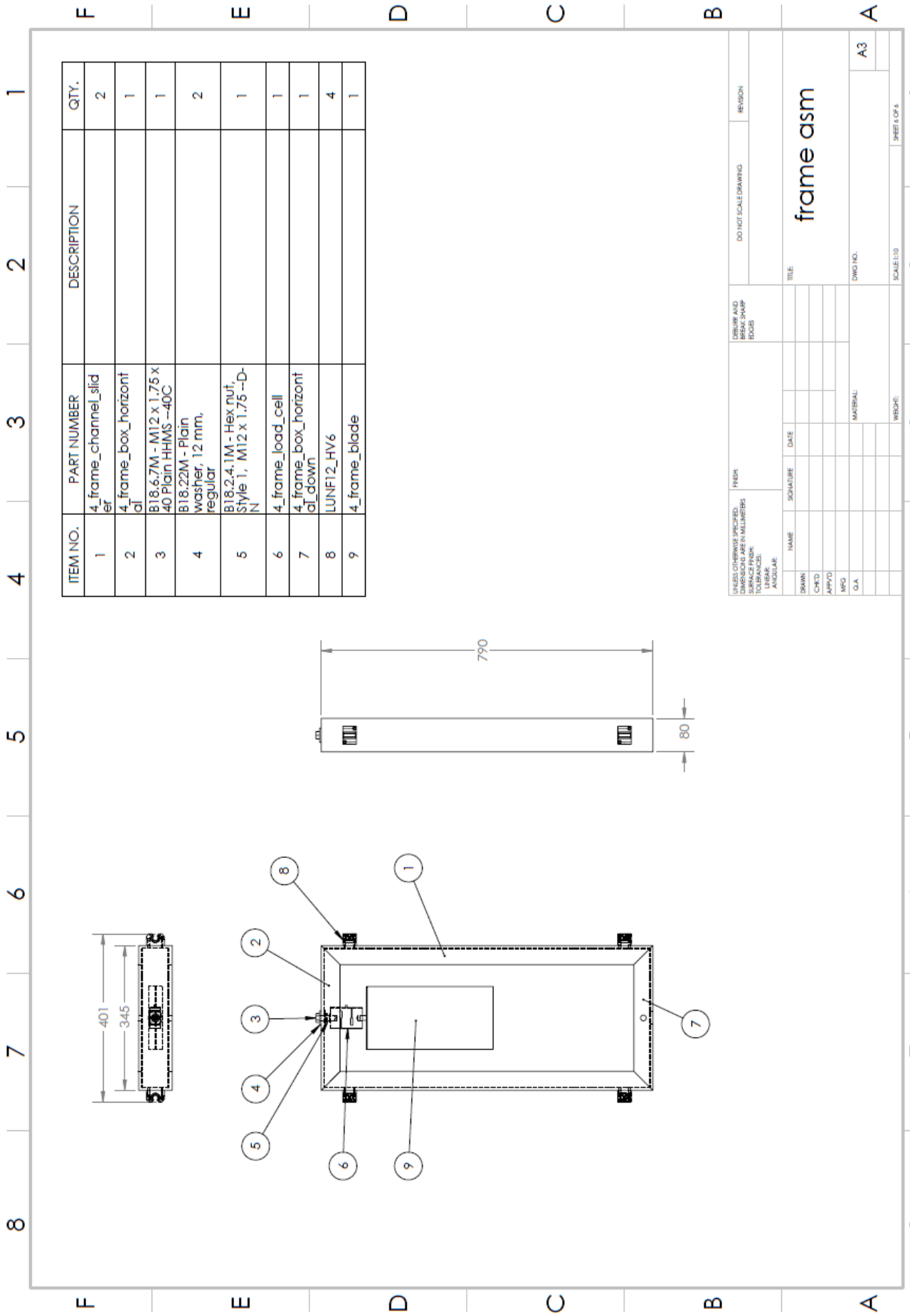

ITEM NO.	PART NUMBER	DESCRIPTION	QTY.
1	4_frame_channel_slider		2
2	4_frame_box_horizontal		1
3	B18.6.7M - M12 x 1.75 x 40 Plain HHMS --40C		1
4	B18.22M - Plain washer, 12 mm, regular		2
5	B18.2.4.1M - Hex nut, Style 1, M12 x 1.75 --D-N		1
6	4_frame_load_cell		1
7	4_frame_box_horizontal_down		1
8	LUNF12_HV6		4
9	4_frame_blade		1

A.2 Pictures of the Adhesion Test Setup

(a)

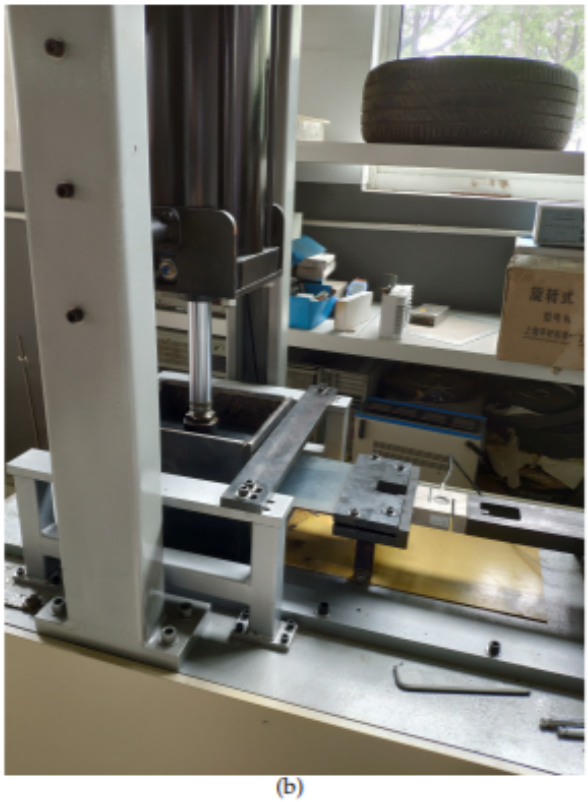

(b)

FIGURE A.2: Pictures of the Adhesion Test Setup: (a) before the pressure is applied and (B) during the pull-out test

A.3 Direct Shear Apparatus

FIGURE A.3: The direct shear apparatus used to measure the undrained shear strength

A.4 Atterberg Limit Tests

In this section the results from the cone drop tests to obtain the plastic limit and liquid limit are presented. Test were carried out according to the Chinese JTG E-40 standards. To obtain the PL and LL, a linear regression is performed on the averages of the depth at 3 different water contents. A linear relation is plotted between the top and middle water content and between the middle and bottom water content. Between these lines, a third line average line is plotted. The water contents where d = 2 and d = 17 *mm* are defined as the plastic limit and the liquid limit. The results are depicted in Figure A.4 and A.5.

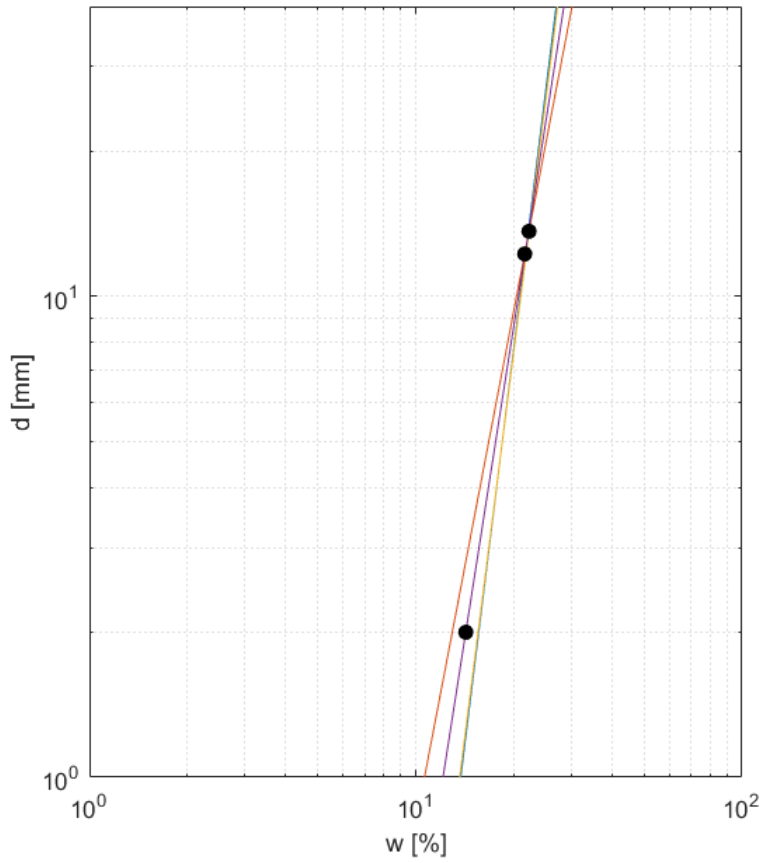

FIGURE A.4: Results from the cone drop tests to obtain the plastic limit and liquid limit

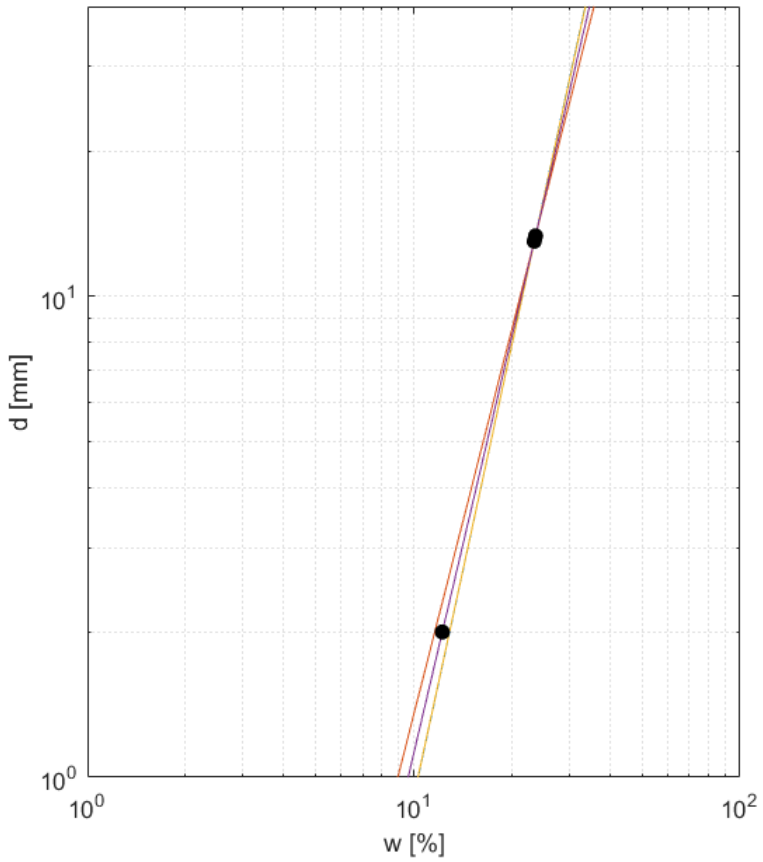

FIGURE A.5: Results from the cone drop tests to obtain the plastic limit and liquid limit

A.5 X-ray Diffraction Results

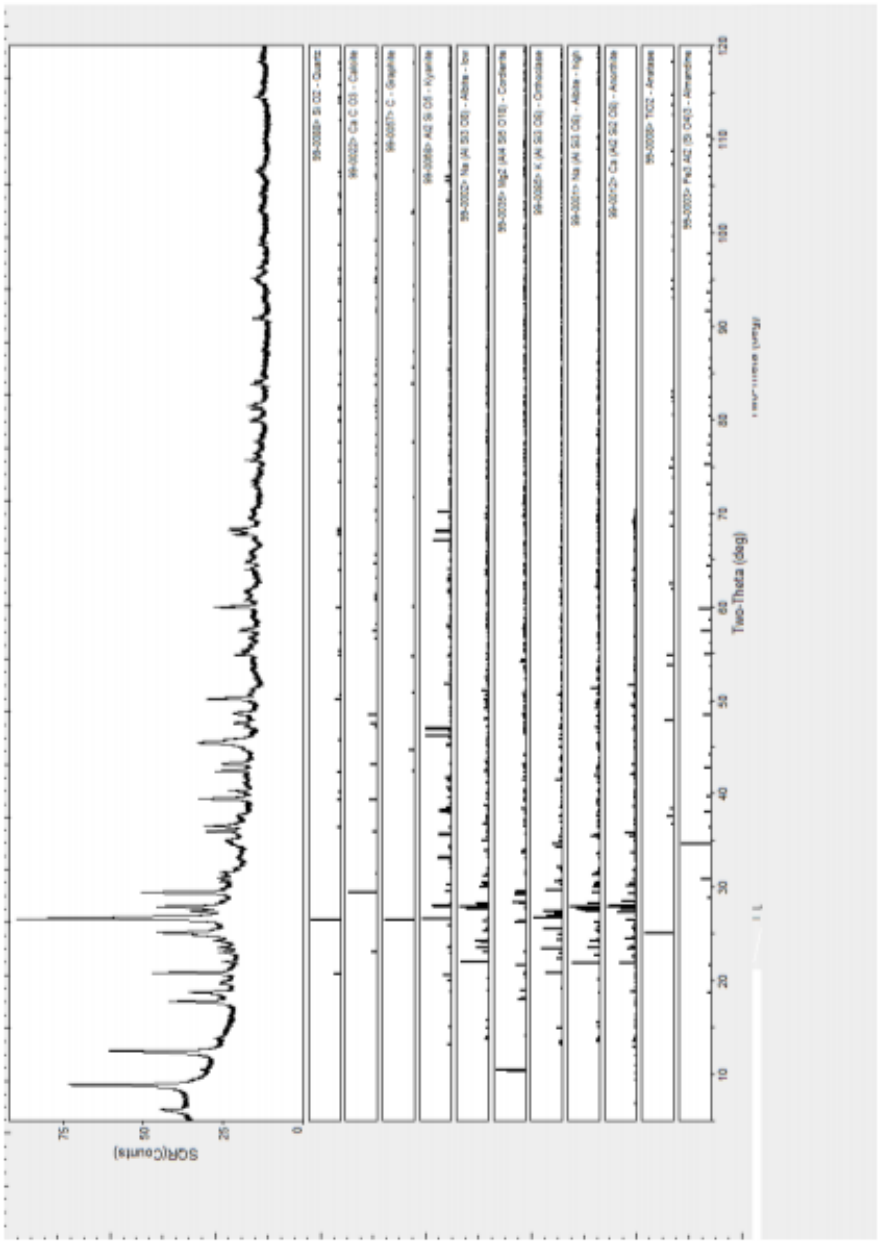

FIGURE A.6: X-ray diffraction result for soil 1

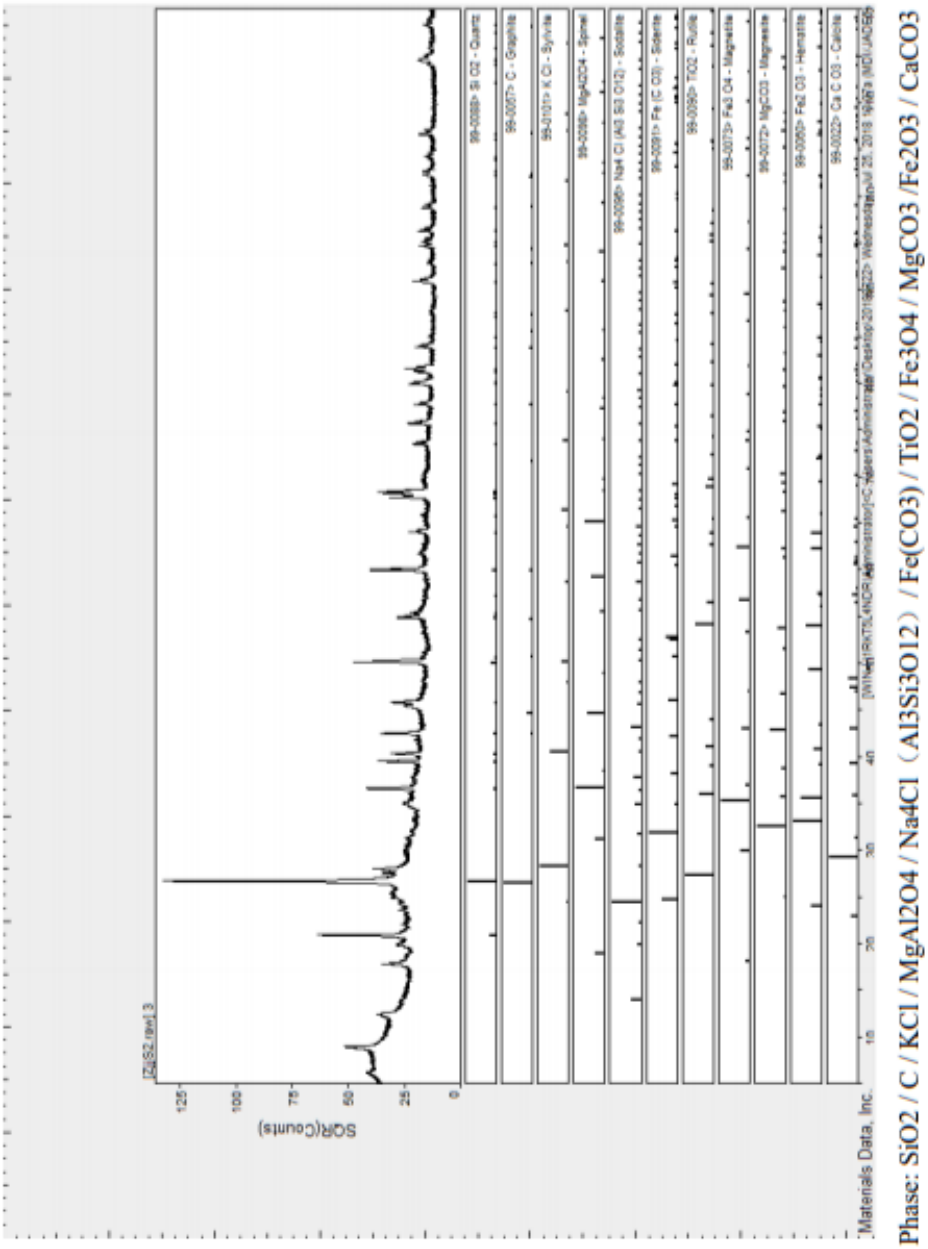

FIGURE A.7: X-ray diffraction result for soil 2

Appendix B

Appendix to Chapter 8: Numerical Modeling for Clay Cutting

B.1 DEM Code for Schulze Ring Shear Test

```
# Settings
        atom_style              granular
        atom_modify             map array
        newton                  off
        units                   si

        boundary                f f f

        processors              2 2 1

        timestep                1e-5

        communicate             single vel yes

        region                  domain block            -10 10 -10 10
        -10 10 units box

        variable                type equal              2 #clay, steel
        create_box              ${type} domain


        variable                thermostep equal        1000
        variable                particlestep equal      1000
        variable                seed equal              15485863
        variable                porosity equal          0.6
        variable                volfraction equal       1-${porosity}

# Particles
        variable                rho equal               2710
        variable                radius equal            0.022
        variable                skin equal              ${radius}*0.25

# Neighbor list settings
        neighbor                ${skin} bin
        neigh_modify            delay 0
```

```
# Contact properties
        fix             m1 all property/global youngsModulus peratomtype
        fix             m2 all property/global poissonsRatio peratomtype
        fix             m3 all property/global coefficientRestitution
        peratomtypepair         2 0.1 0.1 0.1 0.1
        fix             m4 all property/global coefficientFriction
        peratomtypepair         2 0.15 0.1 0.1 0.1
        fix             m5 all property/global characteristicVelocity scalar
        fix             m6 all property/global cohesionEnergyDensity
        peratomtypepair         2 3e5 2e5 2e5 4e4 # 1-1 is clay-clay
        / 1-2 & 2-1 clay-steel / 2-2 steel-steel

        pair_style      gran model hertz tangential history cohesion sjkr
        pair_coeff      * *

        fix             gravi all gravity 9.81 vector 0.0 0.0 -1.0

# Mesh importation
        #fix            ro              all wall/gran model hertz tangential
        history cohesion sjkr type 2 zcylinder 0.2 0.05 0.05

        fix             ins_mesh        all mesh/surface/planar file
        /home/jan/ASTM/ASTM_shearcell/inj_reg.stl type 1 scale 0.1 move
0 0 0.03 curvature_tolerant yes
        fix             ri              all mesh/surface/stress file
        /home/jan/ASTM/ASTM_shearcell/ri_astm.stl type 2 scale 0.1 move
0.5 0.5 0 curvature_tolerant yes
        fix             ro              all mesh/surface/stress file
        /home/jan/ASTM/ASTM_shearcell/ro_astm.stl type 2 scale 0.1 move
0 0 0 curvature_tolerant yes
        fix             bottom          all mesh/surface/stress file
        /home/jan/ASTM/ASTM_shearcell/bottom_astm.stl type 2
        element_exclusion_list read ASTM_shearcell/bottom.exclude scale 0.1
        move  0 0 0 curvature_tolerant yes
        fix             geometry        all wall/gran model hertz tangential
        history cohesion sjkr mesh n_meshes 3 meshes ri ro bottom

# Particle factory
        group                   nve_group               region domain

        fix                     pts1 all particletemplate/sphere 15485863
        atom_type 1 density constant ${rho} radius constant ${radius}
        fix                     pdd1 all particledistribution/discrete
        15485867 1 pts1 1.0

        fix                     pts2 all particletemplate/sphere 49979693
        atom_type 2 density constant ${rho} radius constant 0.0015
        fix                     pdd2 all particledistribution/discrete
        15485863 1 pts2 1.0
```

```
fix                     ins1 all insert/stream seed 67867967
distributiontemplate pdd1 nparticles 15000 particlerate 200000
overlapcheck yes vel constant 0. 0. -5. all_in yes insertion_face
ins_mesh extrude_length 0.7

fix                     integrator all nve/sphere
thermo_style            custom step atoms ke cpu
thermo                  1000
thermo_modify           lost ignore norm no

run                     1 upto

#fix                    ins2 nve_group insert/pack seed 32452843
distributiontemplate pdd2 &
                #maxattempt 100 insert_every 500 overlapcheck yes
                all_in yes &
                #region cylin volumefraction_region 0.33
                ntry_mc 10000

#fix                    integrator all nve/sphere
#thermo_style           custom step atoms ke cpu
#thermo                         1000
#thermo_modify          lost ignore norm no

unfix                   ins1
run                     110000 upto

# Apply normal pressure
unfix                   geometry
fix                     lid all mesh/surface/stress/servo file
/home/jan/ASTM/ASTM_shearcell/lid_astm.stl type 2
element_exclusion_list read ASTM_shearcell/lid.exclude scale 0.1
move 0 0 0.9 curvature_tolerant yes stress on com 0 0 0
axis 0. 0. 1.   ctrlPV force target_val -200000.0 vel_max 50
fix                     geometry2       all wall/gran model hertz
tangential history cohesion sjkr mesh n_meshes 4 meshes ri ro
bottom lid store_force yes

# Dump and print
unfix                   ins_mesh

dump                    dumpstress all mesh/gran/VTK ${particlestep}
/home/jan/ASTM/post/dump*.vtk stress
dump                    dmp all custom ${particlestep}
/home/jan/ASTM/post/dump*.clay id type type x y z ix iy iz vx vy
vz fx fy fz omegax omegay omegaz radius

variable                forcex equal f_bottom[1]
variable                forcey equal f_bottom[2]
variable                forcez equal f_lid[3]
```

```
        variable                torquex equal f_bottom[4]
        variable                torquey equal f_bottom[5]
        variable                torquez equal f_bottom[6]

        fix                     printforce all print 500 "${forcex} ${forcey}
        ${forcez} ${torquex} ${torquey} ${torquez}" screen no file
        data_F_T_r2_2.txt
        thermo_style            custom step atoms ke cpu f_bottom[1]
        f_bottom[2] f_lid[3] f_bottom[4] f_bottom[5] f_bottom[6]

        run                     300000 upto
# Describe shearing action
        variable        w equal 0.5
        variable        T equal 1/${w}
        fix             movecad all move/mesh mesh bottom rotate origin
        1 1 0. axis 0. 0. 1. period ${T}

        run                     500000
```

B.2 DEM Code for The Blade pull-out Test

```
# Environmental Settings

atom_style              granular
atom_modify             map array
newton                  off
units                   si

boundary                p p f

processors              2 2 1

timestep                5e-6

communicate             single vel yes

region                  domain block            -10 10 -10 10 -10 10 units box

region                  domain1 block           -10 10 -10 10 -10 10 units box

variable                type equal              2 #clay, steel
create_box              ${type} domain


variable                thermostep equal        1000
variable                particlestep equal      1000
variable                seed equal              15485863
variable                porosity equal          0.6
variable                volfraction equal       1-${porosity}

variable                porosity1 equal                 0.6
```

```
variable                volfraction1 equal      1-${porosity}

# Particles


variable                rho equal               2710
variable                radius equal            0.022
variable                skin equal              ${radius}*0.25

variable                rho1 equal              2710
variable                radius1 equal           0.022
variable                skin1 equal             ${radius}*0.25

# Neighbor list settings

neighbor                ${skin} bin
neigh_modify            delay 0

# Contact properties

fix             m1 all property/global youngsModulus
peratomtype              30e6 1e9
fix             m2 all property/global poissonsRatio
peratomtype              0.45 0.33
fix             m3 all property/global coefficientRestitution
peratomtypepair          2 0.1 0.1 0.1 0.1
fix             m4 all property/global coefficientFriction
peratomtypepair          2 0.35 0.1 0.1 0.1
fix             m5 all property/global characteristicVelocity scalar
2.
fix             m6 all property/global cohesionEnergyDensity
peratomtypepair          2 3e5 2.25e5 2.25e5 4e4 # 1-1 is clay-clay
/ 1-2 & 2-1 clay-steel / 2-2 steel-steel

pair_style      gran model hertz tangential history cohesion sjkr2
pair_coeff      * *

fix             gravi all gravity 9.81 vector 0.0 0.0 -1.0

# Walls

fix leftX       all wall/gran model hertz tangential history primitive
type 1 xplane 0
fix rightX      all wall/gran model hertz tangential history primitive
type 1 xplane 0.5
fix frontY      all wall/gran model hertz tangential history primitive
type 1 yplane 0
fix backY       all wall/gran model hertz tangential history primitive
type 1 yplane 1
fix bottomZ     all wall/gran model hertz tangential history primitive
type 1 zplane 0.0
```

```
fix leftX1      all wall/gran model hertz tangential history primitive
type 1 xplane 0.51
fix rightX1     all wall/gran model hertz tangential history primitive
type 1 xplane 1.01

# Blade

fix blade       all mesh/surface/stress file /home/jan/CFDEM/jan-PUBLIC-3.0.x/
run/ATS/blade_improved_mesh.stl type 2 scale 0.1 move 0.5 0 -3 stress on
fix bladewall   all wall/gran model hertz tangential history cohesion sjkr
mesh n_meshes 1 meshes blade store_force yes

# Particle factory

region                  birth block             0 0.5 -0 1 0.0 2.6 units box
group                   nve_group                region domain

region                  birth1 block            0.51 1.01 -0 1 0.0 2.6 units box
group                   nve_group1               region domain1


        fix                     pts1 all particletemplate/sphere 15485863
        atom_type 1 density constant ${rho} radius constant ${radius}
        fix                     pdd1 all particledistribution/discrete
        15485867 1 pts1 1.0

        fix                     pts2 all particletemplate/sphere 49979693
        atom_type 2 density constant ${rho} radius constant 0.0015
        fix                     pdd2 all particledistribution/discrete
        15485863 1 pts2 1.0

fix                     ins nve_group insert/pack seed 32452843
distributiontemplate pdd1 &
                        maxattempt 100 insert_every 3000 overlapcheck yes
                        all_in yes &
                        region birth volumefraction_region 0.4 ntry_mc 10000

fix                     ins1 nve_group1 insert/pack seed 32452843
distributiontemplate pdd2 &
                        maxattempt 100 insert_every 3000 overlapcheck yes
                        all_in yes &
                        region birth1 volumefraction_region 0.4 ntry_mc 10000

# Output

fix                     integr nve_group nve/sphere

compute                 rke all erotate/sphere

fix                     integr1 nve_group1 nve/sphere
```

```
compute                 rke1 all erotate/sphere

compute                 bladeforce all wall/gran/local pos vel id
force force_normal

thermo_style            custom step atoms ke c_rke vol f_blade[1] f_blade[2]
f_blade[3]
thermo                  ${thermostep}
thermo_modify           lost ignore norm no

variable                forcex equal f_blade[1]
variable                forcey equal f_blade[2]
variable                forcez equal f_blade[3]

# System start and settling

run                     1

dump                    dmp all custom ${particlestep}
/home/jan/CFDEM/jan-PUBLIC-3.0.x/run/ATS/post/dump*.clay id type type x y z
ix iy iz vx vy vz fx fy fz omegax omegay omegaz radius
dump                    dumpstress all mesh/gran/VTK ${particlestep}
/home/jan/CFDEM/jan-PUBLIC-3.0.x/run/ATS/post/dump*.vtk stress
#dump                   dumpforce all local 500 /home/jan/CFDEM/
jan-PUBLIC-3.0.x/run/hatamura_simulation/post/dump*.csv
c_bladeforce[13] c_bladeforce[14]
c_bladeforce[15] c_bladeforce[16] c_bladeforce[17] c_bladeforce[18]
c_bladeforce[19]
fix                     printforce all print 500 "${forcex} ${forcey}
${forcez}" screen no file force.txt

unfix                   ins
unfix                   ins1
run                     145000 upto

# Cutting

unfix                   rightX

unfix                   leftX1

fix                     sigma_normal nve_group addforce 0.002 0 0

fix                     sigma_normal1 nve_group1 addforce -0.002 0 0

fix topZ                all wall/gran model hertz tangential history
primitive type 1 zplane 1.5

fix                     move all move/mesh mesh blade linear 0 0 5 blade 2
run                     150000
```

```
unfix                   move
```

B.3 DEM Code for the Cutting Model

```
# Environmental Settings

atom_style              granular
atom_modify             map array
newton                  off
units                   si

boundary                p p f

processors              2 2 1

timestep                5e-6

communicate             single vel yes

region                  domain block            -10 10 -10 10 0 10 units box

variable                type equal              2 #clay, steel
create_box              ${type} domain


variable                thermostep equal        1000
variable                particlestep equal      1000
variable                seed equal              15485863
variable                porosity equal          0.6
variable                volfraction equal       1-${porosity}

# Particles


variable                rho equal               2710
variable                radius equal            0.04
variable                skin equal              ${radius}*0.25

# Neighbor list settings

neighbor                ${skin} bin
neigh_modify            delay 0

# Contact properties

fix             m1 all property/global youngsModulus
peratomtype             30e6 1e9
fix             m2 all property/global poissonsRatio
peratomtype             0.45 0.33
fix             m3 all property/global coefficientRestitution
peratomtypepair         2 0.1 0.1 0.1 0.1
```

```
fix             m4 all property/global coefficientFriction
peratomtypepair          2 0.35 0.1 0.1 0.1
fix             m5 all property/global characteristicVelocity scalar
2.
fix             m6 all property/global cohesionEnergyDensity
peratomtypepair          2 300000 112000 112000 400000

pair_style      gran model hertz tangential history cohesion sjkr2
pair_coeff      * *

fix             gravi all gravity 9.81 vector 0.0 0.0 -1.0

# Walls

fix leftX       all wall/gran model hertz tangential history primitive
type 1 xplane -5.5
fix rightX      all wall/gran model hertz tangential history primitive
type 1 xplane -0.5
fix frontY      all wall/gran model hertz tangential history primitive
type 1 yplane -0.5
fix backY       all wall/gran model hertz tangential history primitive
type 1 yplane 0.5
fix bottomZ     all wall/gran model hertz tangential history primitive
type 1 zplane 0.0

# Blade

fix blade       all mesh/surface/stress file
/home/jan/CFDEM/jan-PUBLIC-3.0.x/run/Proper_cohesion_dry/blade55.stl
type 2 scale 0.2 move -5.5 0 0.6 stress on
fix bladewall   all wall/gran model hertz tangential history
cohesion sjkr mesh n_meshes 1 meshes blade store_force yes

# Particle factory
region                  birth block             -5.5 -0.5 -0.5 0.5 0.0 1.2
units box
group                   nve_group                region domain


fix                     pts1 all particletemplate/sphere 15485863 atom_type
1 density constant ${rho} radius gaussian number ${radius} 0.0025
fix                     pdd1 all particledistribution/discrete 15485867
1 pts1 1.0

fix                     ins nve_group insert/pack seed 32452843
distributiontemplate pdd1 &
                        maxattempt 100 insert_every 3000 overlapcheck yes
                        all_in yes &
                        region birth volumefraction_region 0.4 ntry_mc 10000

# Output
```

```
fix                     integr nve_group nve/sphere

compute                 rke all erotate/sphere
compute                 bladeforce all wall/gran/local pos vel id force
force_normal

thermo_style            custom step atoms ke c_rke vol f_blade[1] f_blade[2]
f_blade[3]
thermo                  ${thermostep}
thermo_modify           lost ignore norm no

variable                forcex equal f_blade[1]
variable                forcey equal f_blade[2]
variable                forcez equal f_blade[3]

# System start and settling

run                     1

dump                    dmp all custom ${particlestep} /home/jan/CFDEM/
jan-PUBLIC-3.0.x/run/Proper_cohesion_dry/post/dump*.clay id type type x y z
ix iy iz vx vy vz fx fy fz omegax omegay omegaz radius

dump                    dumpstress all mesh/gran/VTK ${particlestep} /home/
jan/CFDEM/jan-PUBLIC-3.0.x/run/Proper_cohesion_dry/post/dump*.vtk stress
#dump                   dumpforce all local 500 /
home/jan/CFDEM/
jan-PUBLIC-3.0.x/run/hatamura_simulation/post/dump*.csv c_bladeforce[13]
c_bladeforce[14] c_bladeforce[15] c_bladeforce[16] c_bladeforce[17]
c_bladeforce[18] c_bladeforce[19]
fix                     printforce all print 500 "${forcex} ${forcey}
${forcez}" screen no file force.txt

unfix                   ins
run                     145000 upto

## Cutting

fix                     move all move/mesh mesh blade linear 5 0 0 blade 2
run                     100000
unfix                   move
```

TU Delft